DYNAMICS
OF TOPOLOGICAL
MAGNETIC SOLITONS

Thesis submitted for the degree of
doctor of philosophy

Stavros Komineas

UNIVERSITY OF CRETE
DEPARTMENT OF PHYSICS

OCTOBER 1998

ΔΥΝΑΜΙΚΗ ΤΟΠΟΛΟΓΙΚΩΝ ΜΑΓΝΗΤΙΚΩΝ ΣΟΛΙΤΟΝΙΩΝ

Διδακτορική διατριβή του

Σταύρου Κομηνέα

ΠΑΝΕΠΙΣΤΗΜΙΟ ΚΡΗΤΗΣ
ΤΜΗΜΑ ΦΥΣΙΚΗΣ

ΟΚΤΩΒΡΙΟΣ 1998

αφιερώνεται

στην

οικογένειά μου

Ευχαριστίες

Είναι ανάγκη εδώ να εκφράσω τις ευχαριστίες μου προς κάθε έναν που βοήθησε ή παρείχε τα μέσα για την ολοκλήρωση αυτής της προσπάθειας.

Τον επιβλέποντα καθηγητή Ν. Παπανικολάου για τη ανεκτίμητη συμβολή του σε κάθε μέρος της προσπάθειάς μου. Επίσης τους Γιώργο Καλόσακα και Νίκο Κοπιδάκη για το πνεύμα συνεργασίας που είχαμε όλα τα χρόνια κατά τα οποία σπουδάσαμε μες το ίδιο γραφείο.

Το Φυσικό τμήμα του Πανεπιστημίου Κρήτης με συμπεριέλαβε στα μέλη του όλα αυτά τα χρόνια παρέχοντας μου κάθε δικαίωμα και το Ιδρυμα Τεχνολογίας και Ερευνας συνέβαλε στην επιστημονική και οικονομική μου υποστήριξη. Για τούτο και ευχαριστώ ιδιαίτερα όσους κόπιασαν γι' αυτό.

Τέλος, ευχαριστώ τους πολλούς καλούς φίλους με τους οποίους συζήσαμε στο Ηράκλειο και αδιαλείπτως μου παραστάθηκαν.

Την επιτροπή που έκρινε αυτή τη διατριβή αποτέλεσαν οι: Ν. Παπανικολάου, Θ. Τομαράς, Ε. Ν. Οικονόμου, Α. Μπούντης, Γ. Τσιρώνης, Π. Τζανετάκης, Μ. Φλωράτος, Δ. Χαραλαμπίδης.

Σταύρος Κομηνέας

Table of contents

General Introduction

Stable solitary wave solutions appear in nonlinear field theories which describe a variety of physical systems in one, two or three spatial dimensions plus the time. Our main concern will be in systems which can be described within two spatial dimensions and we shall use the term soliton to refer to the stable solitary wave solutions found for such systems.

The existence of solitons as physical entities has so far being established in a remarkably diverse collection of physical systems. Condensed matter physics and fluid dynamics is only some of the areas where the notion of a soliton has found wide application. Thus physicists coming from a variety of research areas have studied the subject from different perspectives while these different insights have provided a wealth of observations about the statics and dynamics of solitons and keep the interest for the subject at a high level. In close connection to the above we usually have the remarkable coincidence that some models which admit soliton solutions are relevant to a variety of physical systems rather than only a single one.

Fields employed in these theories may sometimes be attributed a topological index according to which the static or dynamical solutions are classified into mutually exclusive classes and the relevant solitons will therefore be called topological solitons. Other consequences of topology are also possible and in fact it is expected to have an overall impact on soliton dynamics.

The notion of a soliton has appeared first in connection to one-dimensional systems in order to describe stable traveling wave solutions of nonlinear equations with a very simple dynamical behavior. Namely a single soliton travels undistorted with a constant velocity while two such solitons collide only to emerge with essentially unchanged their profile and velocity after sufficiently long time. The looser term solitary wave has been introduced to describe a more general traveling wave solution of a one-dimensional nonlinear evolution equation.

The surprisingly simple behavior of solitons in one-dimensional systems is attributed to the fact that the relevant equations are integrable in the sense that they possess an infinite set of conserved quantities. Along these lines the Landau-Lifshitz equation which governs at the microscopic level the dynamics of magnetic moments in a magnetic solid, has been found to possess soliton solutions which represent magnetic domain walls. We parenthetically remark here that the picture for nonlinear dynamics that we have described so far can only be contrasted to chaotic systems. These are also described by nonlinear evolution equations and present a highly complex dynamical behavior which leads to deterministic chaos through the routes of period-doubling, intermittency and the formation of strange attractors.

In higher-than-one dimensional systems, one of the best known examples of topological solitons are the magnetic bubbles observed in abundance in ferromagnetic films [1, 2]. Such films are single (magnetic) domain ferromagnets in which the creation of bubbles can be controlled mainly by switching an external magnetic field. Arrays of bubbles as well as isolated ones can be obtained. Isolated bubbles have been observed experimentally as early as 1960 and have been used in device applications since 1967. By now a wealth of experimental results can be found in the literature concerning these bubbles.

Their most notable and unusual dynamical feature is the experimentally observed skew deflection under the influence of an external magnetic field gradient. Extensive experimental studies involving isolated bubbles have been performed and concluded to some simple rules for bubble dynamics. Theoretical studies for magnetic solitons have started with a work by Thiele [3] while the first attempt to study the dynamics was done in [4] drawing attention to the bubble internal structure. It is interesting to note here that the overall picture of bubble dynamics resembles that of vortices in classical fluids or superfluids [14, 34]. These observations suggest that we have a dynamical behavior of solitons generic to a variety of physical systems. Nevertheless different dynamics has been observed in other models such as for monopoles or for skyrmions in σ-models.

A fresh look into magnetic bubble dynamics as well as into the underlying Landau-Lifshitz equation was given in [5]. A simple theoretical description of the dynamics for the model was given emphasizing the role of the topological invariant called the winding number. The approach has been successful in understanding the patterns observed for isolated or pairs of solitons. Thus a ferromagnetic bubble is shown to be pinned in the ferromagnet while the above mentioned skew deflection is understood. Moreover two like solitons are found to move on a more or less circular orbit while a pair of solitons with opposite topological charge undergo Kelvin motion along roughly parallel lines. We also note that a dynamical behavior analogous to that of magnetic bubbles was also found for Abrikosov vortices in a superconductor [6, 7].

Concentrating on the main subject of this thesis we shall try to give an account of the different classes of magnets that are encountered in practice. The most well known class is ferromagnets while as a second class from the theoretical point of view come the antiferromagnets. It is clear that materials of high experimental interest belong to this last class, the parent compounds of high T_c superconductors being a good example. Other classes of magnetic materials are also encountered in practice such as the weak ferromagnets. These are basically antiferromagnets in which an extra so-called Dzyaloshinskii-Moriya interaction gives rise to a weak net magnetic moment [9].

We shall confine ourselves to the important cases of ferromagnets and antiferromagnets. As a first step we have to understand the interactions therein. The strength of the most important among them exchange interaction may vary a lot along the three space directions thus giving rise to layered magnets. The magnetization is expected to vary in principle along only two spatial dimensions allowing for a study within a 2D model. In addition to the exchange an anisotropy energy may be present which comes in a lot of varieties. Some important cases are the uniaxial and an anisotropy of the easy-plane type. Other interactions such as the dipole-dipole interaction among ferromagnetically ordered moments gives rise to a magnetostatic field which plays an important role in certain cases.

An externally supplied magnetic field has often been found to be important. Thus a uniform magnetic field is needed to stabilize bubbles in ferromagnetic films while dynamics is best studied in an external magnetic field gradient. Also in other cases an external field is found to affect profoundly the statics and dynamics in magnets such as is the case for antiferromagnets studied in Chapter III of this thesis. Thus the use of external fields can be a source of intuition as well as a tool for studying the magnetic soliton dynamics.

The above remarks apply to ferromagnets as well as to antiferromagnets. We only note here that, contrary to the wealth of experiments done for ferromagnets, no magnetic solitons have been observed in antiferromagnets mainly because, in contrast to ferromagnetic bubbles, they carry almost no magnetic dipole moment. Nevertheless theoretical arguments suggest that they should exist for essentially the same reasons as in ferromagnets. Moreover an indirect proof for their existence is provided from related work in weak ferromagnets.

We now proceed to a description of the general outline of this thesis. In Chapter I we present a theory for the description of the dynamics of bubbles in ferromagnetic films. This is based on the theory presented in [5]. The quasi two-dimensional geometry of the film calls for a generalization to three dimensions and a suitable extension of the arguments of [5] to properly take into account boundary effects. The chapter is completed with a detailed numerical calculation of the axially symmetric (so-called fundamental) bubble taking into full account the long range non-local magnetostatic field. This field is known to be present due to the dipole-dipole interaction among magnetic ions and plays a crucial role in the statics of the bubble. We believe to give here a clear picture of the dynamics of an isolated bubble in a realistic ferromagnetic film.

Some of the finer issues of the motion of the bubble remain difficult to study either numerically or analytically in the 3D film geometry. Thus the long term dynamics may be quite complicated and can only be studied within a 3D numerical algorithm. But, despite that the bubbles are three-dimensional objects, their topological characteristics are essentially two-dimensional. Thus we decided to analyze some of the important details of the bubble motion within the two-dimensional isotropic Heisenberg model and perform some straightforward numerical calculations. In Chapter II we study this model within the present theoretical framework and present the results of an analysis obtained mainly through numerical simulations of the bubble motion which further complete and clarify the arguments presented in Chapter I.

In Chapter III we study vortices in two-dimensional or layered antiferromagnets. Their dynamics is expected to be essentially different from that of ferromagnetic solitons and be described by the relativistic nonlinear σ-model [9]. We first give a detailed derivation of the σ-model treating properly some parity breaking contributions that are implicit in the model due to the antiferromagnetic discontinuity. We then proceed to study numerically the dynamics of vortices. Two vortices are shown to scatter at right angles but we find that the presence of a uniform external magnetic field affects the dynamics rather profoundly. Then an isolated vortex is found to be pinned in the antiferromagnet while relevant motion is only possible in the presence of other vortices. This is a situation similar to that in the ferromagnet. A topological charge relevant to the dynamics is given and finally the dynamical behavior of vortices in the presence of the external field is explained by arguments analogous to those employed in the theory of Chapter I.

CHAPTER I

FERROMAGNETIC FILMS

1. Introduction

Magnetic bubbles have been known to exhibit some distinct dynamical features due to their nontrivial topological structure. The inherent link between topology and dynamics was already apparent in the early work of Thiele [4] as well as in many investigations that followed [1, 2]. The essence of the early work is best summarized by the experimentally observed skew deflection of magnetic bubbles under the influence of an applied magnetic-field gradient. The so-called golden rule of bubble dynamics relates the deflection angle δ to the winding number Q by

$$\frac{gr^2}{2V}\sin\delta = Q, \tag{1.1}$$

where g is the strength of the applied field gradient, r is the bubble radius and V its speed. Relation (1.1) is remarkable in two respects. First, it suggests that only topologically trivial ($Q = 0$) bubbles move in the direction of the gradient ($\delta = 0$), even though such a behavior would naively be expected for all magnetic bubbles; in fact, bubbles with a nonvanishing winding number ($Q = \pm 1, \pm 2, \ldots$) tend to be deflected in a direction nearly perpendicular ($\delta \sim 90^\circ$) to the applied gradient. Second, Eq. (1.1) implies some sort of a topological quantization in that it relates the integer-valued winding number to experimentally measured quantities that can, in principle, assume any values.

Although golden rule (1.1) has been employed with considerable success in the analysis of actual experiments, especially for hard ($|Q| \gg 1$) bubbles, it is still a semi-empirical relation whose precise meaning and domain of validity must be specified.

For instance, the meaning of the various quantities entering Eq. (1.1) needs to be explained because magnetic bubbles are extended structures rather than point-like particles. Furthermore the usual derivations of (1.1) are based on the assumption that the bubble reaches a steady state, in the presence of dissipation, in which the deflection angle δ, the radius r and the speed V approach constant values. But such an assumption was never justified and is actually incorrect. In practice, experiments are analyzed by applying Eq. (1.1) with average values for the deflection angle and the speed and by assuming that the radius does not change significantly during the application of the gradient.

In some recent work on this subject [5] the link between topology and dynamics was made explicit through the construction of unambiguous conservation laws as moments of a suitable topological vorticity. The important qualitative features of bubble dynamics became then apparent. Thus, in the absence of external magnetic-field gradients or other perturbations, bubbles with a nonvanishing winding number cannot move freely but are always spontaneously pinned. On the other hand, in the absence of dissipation, a bubble would be deflected at a right angle ($\delta = 90^\circ$) with respect to an applied magnetic-field gradient, with a drift velocity that can be calculated analytically in some important special cases [5] and is generally consistent with Eq. (1.1). The emerging picture is thus analogous to the Hall motion of an electron as well as to the Magnus effect of fluid dynamics. These analogies further suggest that the deflection angle should deviate from 90° in the presence of dissipation. However an exact calculation of the deflection angle, i.e., a derivation of the golden rule, is no longer possible on the basis of conservation laws alone.

Therefore the semi-quantitative picture derived from the conservation laws must be supplemented by some results from a numerical solution of the underlying Landau-Lifshitz equation. Such a solution is not straightforward under completely realistic conditions; calculation of the long-range magnetostatic field is always a problem and the finite thickness of actual magnetic films forces one to work with a three-dimensional (3D) grid, even though the essential topological structure of magnetic bubbles is two-dimensional (2D). Hence the numerical efforts have thus far been restricted to strictly 2D models of increasing complexity [10, 11].

Our purpose in the present chapter is to provide a precise formulation within the quasi-2D geometry of realistic ferromagnetic films, taking into account the effects from the film boundaries and the magnetostatic field based on the work presented in [12]. In Section 2 we review some basic facts about the Landau-Lifshitz equation and introduce convenient (rationalized) physical units. In Section 3 we discuss the two ingredients that are important to establish a direct link between the topological complexity of magnetic structures and their dynamics, the gyrovector and the stress tensor. The derivation of unambiguous conservation laws is then carried out in Section 4 in the presence of film boundaries. A byproduct of our study of conservation laws is a set of virial theorems that generalize the well-known scaling relation of Derrick [13], an issue taken up in Section 5. In Section 6 we desribe in detail a numerical relaxation algorithm for the calculation of static bubble solutions. We finally present a detailed numerical calculation of the fundamental ($Q = 1$) bubble which is consistent with the virial theorems. The issue of skew deflection in an applied magnetic-field gradient is studied in Section 7 where we find that the semi-empirical golden rule is verified in its gross features but not in its details. Our conclusions are summarized in Section 8 together with some suggestions for further work.

2. The Landau-Lifshitz equation

A ferromagnetic medium is described in terms of the density of magnetic moment or magnetization $\mathbf{M}$ which is due primarily to the electron spins but may include contributions also from the orbital motion. In general, the vector $\mathbf{M} = (M_1, M_2, M_3)$ is a function of position and time except that its magnitude is nearly constant for a wide temperature range sufficiently below the Curie point. Thus we write

$$\mathbf{M} = \mathbf{M}(\mathbf{x}, t), \qquad \mathbf{M}^2 \equiv M_1^2 + M_2^2 + M_3^2 = M_0^2, \tag{2.1}$$

where $\mathbf{x} = (x_1, x_2, x_3)$ is the position vector, t is the time variable, and the constant M_0 is the saturation magnetization.

Static as well as dynamical properties of the magnetization are governed by the Landau-Lifshitz equation

$$\frac{\partial \mathbf{M}}{\partial t} + \gamma(\mathbf{M} \times \mathbf{F}) = \frac{\lambda}{M_0}\left(\mathbf{M} \times \frac{\partial \mathbf{M}}{\partial t}\right), \tag{2.2}$$

which describes precession around an effective field $\mathbf{F}$ with the constant γ given by

$$\gamma = \frac{g_e |e|}{2 m_e c}, \tag{2.3}$$

where $g_e \sim 2$ is the gyromagnetic ratio, e the electron charge, m_e the electron mass, and c the velocity of light. Equation (2.2) also includes a phenomenological (Landau-Gilbert) dissipative term where the dissipation constant λ is dimensionless. This choice of dissipation preserves the magnitude of magnetization.

The effective field $\mathbf{F}$ may be written as

$$\mathbf{F} = \mathbf{F}_e + \mathbf{F}_a + \mathbf{H}_b + \mathbf{H}. \tag{2.4}$$

Here $\mathbf{F}_e$ is the exchange field

$$\mathbf{F}_e = \frac{2A}{M_0^2}\Delta\mathbf{M}, \tag{2.5}$$

where A is the exchange stiffness constant and Δ the Laplace operator. $\mathbf{F}_a$ is the anisotropy field

$$\mathbf{F}_a = -\frac{2K}{M_0^2}(M_1, M_2, 0), \tag{2.6}$$

where K is a positive constant leading to an easy axis in the third direction. In ferromagnetic films made out of bubble materials the easy axis is perpendicular to the film surface [1]. $\mathbf{H}_b$ is a uniform bias field,

$$\mathbf{H}_b = (0, 0, H_b), \qquad H_b = \text{const}, \tag{2.7}$$

applied along the easy axis. Finally $\mathbf{H}$ is the magnetic field produced by the magnetization itself and thus satisfies the magnetostatic equations

$$\boldsymbol{\nabla} \times \mathbf{H} = 0, \qquad \boldsymbol{\nabla} \cdot \mathbf{B} = 0; \qquad \mathbf{B} = \mathbf{H} + 4\pi\mathbf{M}, \tag{2.8}$$

where $\mathbf{B}$ is the corresponding magnetic induction. The use of the magnetostatic instead of the complete Maxwell equations is justified by the fact that time variations of magnetic structures of practical interest are slow.

Numerical values of the various constants introduced above may be found in Ref. [1] for a number of ferromagnetic materials. However using all these constants within a theoretical development clouds the underlying simplicity of the Landau-Lifshitz equation. Hence we introduce rationalized physical units as follows. First, we work with the normalized magnetization

$$\mathbf{m} = \mathbf{M}/M_0, \qquad \mathbf{m}^2 = 1. \tag{2.9}$$

Second, we measure distance, time and magnetic field (induction) in units of

$$\sqrt{\frac{A}{2\pi M_0^2}}, \qquad \frac{1}{4\pi\gamma M_0} \quad \text{and} \quad 4\pi M_0, \tag{2.10}$$

respectively. We further define the dimensionless anisotropy constant

$$\kappa = \frac{K}{2\pi M_0^2}, \tag{2.11}$$

which is usually referred to as the quality factor. Finally, we introduce new symbols for dimensionless magnetic fields, such as $\mathbf{h} = \mathbf{H}/4\pi M_0$, but maintain the same symbols $\mathbf{x}$ and t for the rationalized space and time variables.

The Landau-Lifshitz equation is then written as

$$\dot{\mathbf{m}} + (\mathbf{m} \times \mathbf{f}) = \lambda(\mathbf{m} \times \dot{\mathbf{m}}), \qquad \mathbf{m}^2 = 1, \tag{2.12}$$

where the dot denotes differentiation with respect to time, a convention that will be adopted from now on. The effective field $\mathbf{f}$ is given by

$$\mathbf{f} = \Delta\mathbf{m} - \kappa(m_1, m_2, 0) + \mathbf{h}_b + \mathbf{h}, \tag{2.13}$$

where $\mathbf{h}_b = (0, 0, h_b)$ is the bias field and $\mathbf{h}$ satisfies the magnetostatic equations

$$\boldsymbol{\nabla} \times \mathbf{h} = 0, \qquad \boldsymbol{\nabla} \cdot \mathbf{b} = 0; \qquad \mathbf{b} = \mathbf{h} + \mathbf{m}. \tag{2.14}$$

The only free parameters are now the quality factor κ, the dissipation constant λ, and the bias field h_b.

The remainder of this section is devoted to a discussion of the hamiltonian structure associated with the Landau-Lifshitz equation at vanishing dissipation ($\lambda = 0$). Then we write

$$\dot{\mathbf{m}} + (\mathbf{m} \times \mathbf{f}) = 0, \qquad \mathbf{m}^2 = 1, \tag{2.15}$$

where the effective field $\mathbf{f}$ is still given by Eq. (2.13) and may be expressed entirely in terms of the magnetization once the magnetostatic field $\mathbf{h}$ is determined by solving the linear system (2.14). Now a conserved energy functional $W = W(\mathbf{m})$ exists such that the effective field is obtained through the general relation

$$\mathbf{f} = -\frac{\delta W}{\delta \mathbf{m}}, \tag{2.16}$$

where the symbol δ denotes the usual functional derivative. Equation (2.16) together with Eq. (2.15) imply that the functional W is indeed conserved, and that (2.15) is the Hamilton equation associated with the hamiltonian W endowed with the Poisson-bracket relations

$$\{m_i(\mathbf{x}), m_j(\mathbf{x}')\} = \varepsilon_{ijk} m_k(\mathbf{x}) \delta(\mathbf{x} - \mathbf{x}'), \tag{2.17}$$

which are reminiscent of the spin commutation relations. Here ε_{ijk} is the 3D antisymmetric tensor and the usual summation convention for repeated indices is invoked.

In order to display the explicit form of the energy functional we write

$$W = W_e + W_a + W_b + W_m, \tag{2.18}$$

where the four terms correspond to the exchange, anisotropy, bias, and mangetostatic field. The more or less obvious choice of the exchange energy,

$$W_e = \int w_e dV, \qquad w_e = \frac{1}{2}(\partial_i \mathbf{m} \cdot \partial_i \mathbf{m}), \tag{2.19}$$

where w_e is the corresponding energy density, requires some qualification in the presence of boundaries. Thus we consider the functional variation

$$\delta W_e = \int (\partial_i \delta\mathbf{m} \cdot \partial_i \mathbf{m}) dV = \oint (\delta\mathbf{m} \cdot \partial_i \mathbf{m}) dS_i - \int (\delta\mathbf{m} \cdot \Delta\mathbf{m}) dV, \tag{2.20}$$

where the surface-element vector $d\mathbf{S} = (dS_1, dS_2, dS_3)$ is perpendicular to the boundaries of the ferromagnetic medium. Equation (2.20) would yield the desired relation

$$\mathbf{F}_e = -\frac{\delta W_e}{\delta \mathbf{m}} = \Delta\mathbf{m}, \tag{2.21}$$

if the surface integral were absent; that is, if the gradient of the magnetization along the normal to the surface vanished. We write symbolically

$$\frac{\partial \mathbf{m}}{\partial n} = 0, \tag{2.22}$$

which will be viewed as a boundary condition to be imposed at the free boundaries of the medium, in addition to the familiar boundary conditions of magnetostatics. This "unpinned" boundary condition was previously employed in the study of ferromagnetic films [1] and will play an important role in the following.

On the other hand, the usual bulk expressions for the anisotropy and bias (Zeeman) energies,

$$\begin{aligned} W_a &= \int w_a dV, \qquad w_a = \frac{\kappa}{2}(m_1^2 + m_2^2) \\ W_b &= \int w_b dV, \qquad w_b = h_b(1 - m_3), \end{aligned} \tag{2.23}$$

are free of boundary ambiguities and obviously yield the corresponding contributions to the effective field through the general relation (2.16). Note that in the Zeeman energy we have subtracted the (trivial) contribution from the state

$$\mathbf{m}_0 = (0, 0, 1), \tag{2.24}$$

which describes a fully saturated ferromagnet and will thus be referred to as the ground state. Configuration (2.24) is the simplest example of a static solution of the Landau-Lifshitz equation.

Boundary effects are also important in the definition of the magnetostatic energy and will be described here in some detail. We begin with the reasonable ansatz

$$W_m = \frac{1}{2}\int \mathbf{h}^2 dV, \tag{2.25}$$

where it is understood that the integral extends over all volume, inside and outside the material, and that the field $\mathbf{h}$ is expressed in terms of the magnetization through Eqs. (2.14). However, in order to justify that (2.25) is an appropriate choice of the mangetostatic energy within the context of the Landau-Lifshitz equation, one must show that

$$\mathbf{h} = -\frac{\delta W_m}{\delta \mathbf{m}}. \tag{2.26}$$

Such a demonstration is not completely straightforward because of the implicit dependence of $\mathbf{h}$ on the magnetization.

To make this dependence explicit we introduce a scalar potential ψ from

$$\mathbf{h} = -\boldsymbol{\nabla}\psi, \qquad \Delta\psi = (\boldsymbol{\nabla}\cdot\mathbf{m}), \tag{2.27}$$

and solve the Poisson equation to obtain

$$\psi(\mathbf{x}) = \frac{1}{4\pi}\left[\oint \frac{\mathbf{m}(\mathbf{x}')\cdot d\mathbf{S}'}{|\mathbf{x}-\mathbf{x}'|} - \int \frac{(\boldsymbol{\nabla}\cdot\mathbf{m})(\mathbf{x}')}{|\mathbf{x}-\mathbf{x}'|} dV'\right], \tag{2.28}$$

where the surface integral extends over the boundaries of the ferromagnetic medium, if any, and the volume integral over the bulk of the medium. Applying a careful partial integration yields the equivalent relation

$$\psi(\mathbf{x}) = \frac{1}{4\pi}\int \frac{(\mathbf{x}-\mathbf{x}')\cdot\mathbf{m}(\mathbf{x}')}{|\mathbf{x}-\mathbf{x}'|^3} dV', \tag{2.29}$$

whose advantage is that it contains no derivatives of the magnetization and is valid irrespectively of the presence of boundaries.

As an elementary illustration we consider a ferromagnetic film of thickness d (see Fig. 1) and assume that the magnetization is equal to its ground-state value (2.24) inside the film (region I) and vanishes outside (regions II and III). An explicit calculation of the integral in Eq. (2.29) then yields

$$\psi = \begin{cases} d/2, & x_3 > d/2 \\ x_3, & -d/2 < x_3 < d/2 \\ -d/2, & x_3 < -d/2. \end{cases} \tag{2.30}$$

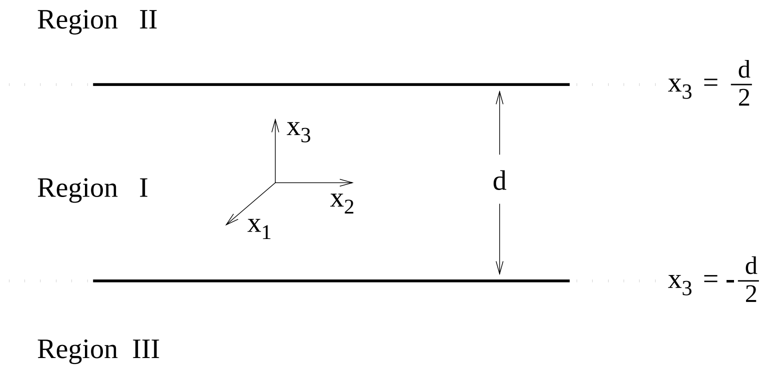

Fig. 1: Conventions concerning a ferromagnetic film of thickness d. The film extends to infinity in the x_1 and x_2 directions.

Therefore the magnetic field is given by $\mathbf{h} = -\boldsymbol{\nabla}\psi = -\mathbf{m}_0$ inside the film and vanishes outside. The magnetic induction $\mathbf{b} = \mathbf{h} + \mathbf{m}_0$ vanishes everywhere.

We now return to the magnetostatic energy (2.25) and replace $\mathbf{h}^2$ by $-\mathbf{h}\cdot(\boldsymbol{\nabla}\psi)$. An application of the divergence theorem and Eqs. (2.14) then gives

$$W_m = \frac{1}{2}\left[\oint \psi(\mathbf{m}\cdot d\mathbf{S}) - \int \psi(\boldsymbol{\nabla}\cdot\mathbf{m})dV\right], \tag{2.31}$$

where we have also used the fact that ψ is continuous across the boundary and that the difference between the normal components of the magnetic field on the two sides of the boundary is equal to the normal component of the magnetization. A further partial integration transforms (2.31) into

$$W_m = -\frac{1}{2}\int(\mathbf{h}\cdot\mathbf{m})dV, \tag{2.32}$$

which shares with Eq. (2.29) the property that it is valid whether or not boundaries are present. Hence, using this form of the magnetostatic energy and a magnetic field calculated from Eq. (2.29), the basic relation (2.26) is established by straightforward manipulations.

We complete the discussion of the canonical structure noting that the Landau-Lifshitz equation is actually a constrained hamiltonian system. Nevertheless one may resolve the constraint $\mathbf{m}^2 = 1$ explicitly using, for example, the spherical parametrization

$$m_1 = \sin\Theta\cos\Phi, \qquad m_2 = \sin\Theta\sin\Phi, \qquad m_3 = \cos\Theta. \tag{2.33}$$

The energy functional is then parametrized in terms of the two independent fields Θ and Φ and the general form of the Landau-Lifshitz equation reads

$$\sin\Theta\ \dot{\Theta} = -\frac{\delta W}{\delta\Phi}, \qquad \sin\Theta\ \dot{\Phi} = \frac{\delta W}{\delta\Theta}, \tag{2.34}$$

which suggests that the pair of fields

$$\Pi = \cos\Theta \quad \text{and} \quad \Phi \tag{2.35}$$

is a canonical pair:

$$\dot{\Pi} = \frac{\delta W}{\delta \Phi}, \qquad \dot{\Phi} = -\frac{\delta W}{\delta \Pi}. \tag{2.36}$$

However most of the special dynamical features of the ferromagnetic continuum emerge exactly when the definition of the canonical variables (2.35) encounters ambiguities due to a possibly nontrivial topological structure of the magnetization.

Finally we return briefly to the issue of dissipation and rewrite Eq. (2.12) in the equivalent form

$$\begin{aligned} &\dot{\mathbf{m}} + (\mathbf{m}\times\mathbf{G}) = 0, \qquad \mathbf{m}^2 = 1, \\ &\mathbf{G} = \lambda_1 \mathbf{f} + \lambda_2(\mathbf{m}\times\mathbf{f}), \qquad \lambda_1 = \frac{1}{1+\lambda^2}, \qquad \lambda_2 = \frac{\lambda}{1+\lambda^2}. \end{aligned} \tag{2.37}$$

We then examine the rate at which the energy changes in the presence of dissipation:

$$\dot{W} = \int \left(\frac{\delta W}{\delta \mathbf{m}} \cdot \dot{\mathbf{m}}\right) dV = -\lambda \int \dot{\mathbf{m}}^2 \, dV, \tag{2.38}$$

whish is negative when the dissipation constant λ is positive.

3. Gyrovector and the stress tensor

The key quantity for the description of both topological and dynamical properties of the magnetization is the gyrovector or vorticity $\boldsymbol{\gamma} = (\gamma_1, \gamma_2, \gamma_3)$ whose cartesian components are given by

$$\gamma_i = -\frac{1}{2}\varepsilon_{ijk}(\partial_j \mathbf{m} \times \partial_k \mathbf{m}) \cdot \mathbf{m}. \tag{3.1}$$

The former terminology was introduced in the early work [4] but the latter seems more appropriate in view of the significant formal analogy of the vector $\boldsymbol{\gamma}$ with ordinary vorticity in fluid dynamics. Nevertheless one should stress that $\boldsymbol{\gamma}$ is not related to actual rotational motion in the ferromagnetic continuum but rather to the topological complexity of the magnetization. For the moment, we are concerned with instantaneous properties of the unit vector field $\mathbf{m} = \mathbf{m}(\mathbf{x})$ at some instant t that is not displayed explicitly. Questions of dynamics will be addressed later in this section.

An immediate consequence of the definition (3.1) and the constraint $\mathbf{m}^2 = 1$ is that the vorticity field is solenoidal,

$$\boldsymbol{\nabla} \cdot \boldsymbol{\gamma} = 0, \tag{3.2}$$

and hence the corresponding vortex lines cannot terminate but at the boundaries of the ferromagnetic medium. The precise nature of vortex lines is revealed by expressing the vorticity in terms of the canonical variables (2.35),

$$\boldsymbol{\gamma} = \boldsymbol{\nabla}\Pi \times \boldsymbol{\nabla}\Phi, \tag{3.3}$$

a relation that suggests an analogy of Π and Φ with the Clebsch potentials of fluid dynamics [14]. It also establishes that vortex lines are defined as the intersections of the two surfaces $\Pi(\mathbf{x}) = c_1$ and $\Phi(\mathbf{x}) = c_2$ where c_1 and c_2 are arbitrary constants. In other words, vortex lines are the curves along which the magnetization vector $\mathbf{m}$ remains constant.

Such a simple definition of vortex lines allows a transparent topological classification of the possible distributions of magnetization. We shall consider the physically interesting class of configurations $\mathbf{m} = \mathbf{m}(\mathbf{x})$ that are differentiable functions of position and approach the ground state of the ferromagnet at spatial infinity:

$$\mathbf{m}(\mathbf{x}) \underset{|\mathbf{x}| \to \infty}{\longrightarrow} \mathbf{m}_0 = (0, 0, 1). \tag{3.4}$$

In the absence of boundaries the medium extends to infinity in all directions and vortex lines are closed curves. One may then define a degree of knottedness, or helicity, of tangled vortex lines by analogy with related work in fluid dynamics [15] and magnetohydrodynamics [16]. The current status of the topological aspects of the above subjects may be traced from Ref. [17]. In the present context, such a degree is more appropriately referred to as the Hopf index [18]. In view of the boundary condition (3.4) the 3D space is isomorphic to the sphere S^3 and a specific configuration $\mathbf{m} = \mathbf{m}(\mathbf{x})$ establishes a map from S^3 to S^2, where S^2 is the 2D sphere defined from the constraint $\mathbf{m}^2 = 1$. Such a map is characterized by the integer-valued Hopf index defined as follows. Let $\mathbf{m}(\mathbf{x}) = \mathbf{m}_1$ and $\mathbf{m}(\mathbf{x}) = \mathbf{m}_2$ be any two vortex lines where $\mathbf{m}_1$ and $\mathbf{m}_2$ are constant unit vectors. The linking number of these two curves is independent of the specific choice of the pair of vortex lines and is called the Hopf index of configuration $\mathbf{m}(\mathbf{x})$.

In order to make a first contact with the dynamics we also quote an analytical definition of the Hopf index. The solenoidal vorticity is derived from a vector potential $\mathbf{a}$,

$$\boldsymbol{\gamma} = \boldsymbol{\nabla} \times \mathbf{a}, \tag{3.5}$$

and the Hopf index is given by

$$N = \frac{1}{4\pi} \int (\mathbf{a} \cdot \boldsymbol{\gamma}) dV. \tag{3.6}$$

Although the vector potential is unique only to within a gauge transformation, N is gauge invariant and may be expressed entirely in terms of $\boldsymbol{\gamma}$ by

$$N = \frac{1}{(4\pi)^2} \int \varepsilon_{ijk} \gamma_i(\mathbf{x}) \frac{(\mathbf{x} - \mathbf{x}')_j}{|\mathbf{x} - \mathbf{x}'|^3} \gamma_k(\mathbf{x}') dV dV'. \tag{3.7}$$

The remarkable fact is that the above integral is always equal to an integer, and its explicit values coincide with those obtained through the linking-number definition given in the preceding paragraph [19, 20].

It would appear that a simpler (local) expression for the vector potential may be derived from Eq. (3.3) which suggests that

$$\mathbf{a} = \Pi \boldsymbol{\nabla} \Phi, \tag{3.8}$$

provided that Π and Φ are differentiable functions of position. However inserting (3.3) and (3.8) in (3.6) would then lead to a vanishing Hopf index. Putting it differently, the canonical variables Π and Φ cannot be both differentiable for field configurations with $N \neq 0$, even though the magnetization is always assumed to be differentiable. Indeed explicit examples worked out in the literature [5, 21] demonstrate that the magnetization reaches the north as well as the south pole of the sphere $\mathbf{m}^2 = 1$ along certain (vortex) lines where the angular variable Φ becomes multivalued when $N \neq 0$. While these difficulties are largely irrelevant, because of the gauge-invariant definition (3.7), they already provide an important hint concerning dynamics. Note that the vector potential (3.8) coincides with the familiar expression for the momentum density associated with the Hamilton equations (2.36). We thus conclude that the difficulties discussed in connection with Eq. (3.8) render ambiguous also the usual linear momentum.

We defer for the moment further discussion of dynamics and return to the question of topological classification in the presence of boundaries. Specifically we consider the film geometry of Fig. 1 where vortex lines need not be closed but may terminate at the boundaries of the film. Hence a definition of a Hopf index is no longer meaningful. Instead we consider the flux of vorticity

$$Q = \frac{1}{4\pi} \int_S \boldsymbol{\gamma} \cdot d\mathbf{S} \tag{3.9}$$

through any open surface S that is contained within the film but extends to infinity on all sides. The flux is independent of the specific choice of a surface with the above properties, thanks to $\boldsymbol{\nabla} \cdot \boldsymbol{\gamma} = 0$ and an elementary application of the divergence theorem. In particular, S may be a plane perpendicular to the third axis,

$$Q = \frac{1}{4\pi} \int \gamma_3 dx_1 dx_2, \qquad -\frac{d}{2} < x_3 < \frac{d}{2}, \tag{3.10}$$

where the double integral is independent of x_3. In fact, this integral coincides with the Pontryagin index or winding number [19] of the magnetization and is also integer-valued ($Q = 0, \pm1, \pm2, \ldots$). Again, when $Q \neq 0$, the canonical variables Π and Φ cannot be defined everywhere and the corresponding linear momentum is ambiguous.

To be sure, the topological classification described above does not assume that the configuration $\mathbf{m} = \mathbf{m}(\mathbf{x})$ solves the Landau-Lifshitz equation but merely that it obeys some general physical restrictions such as differentiability and Eq. (3.4). Of course, this classification would become especially relevant if stationary solutions were found with a nontrivial topology. In this respect, we note that arguments of varying completeness have been presented in the literature for the existence of magnetic vortex rings with a nonvanishing Hopf index [5, 21] but a definite theoretical treatment and actual observation are still lacking. Nonetheless magnetic bubbles with a wide range of winding numbers have been observed in ferromagnetic films [1, 2]. Finally, if the magnetization itself is allowed to be nondifferentiable at isolated singular points, one is naturally led to a class of topological *defects* that are also characterized by a winding number of the form (3.9) except that the surface S is now closed around a singular point. Such defects have been observed in the bulk of the ferromagnetic continuum and are called Bloch points [1, 2].

We now organize the various hints concerning the connection between topology and dynamics by considering the time evolution of the vorticity (3.1). An elementary calculation based on the Landau-Lifshitz equation at vanishing dissipation, Eq. (2.15), leads to

$$\dot{\gamma}_i = -\varepsilon_{ijk}\partial_j(\mathbf{f} \cdot \partial_k \mathbf{m}) = \varepsilon_{ijk}\partial_j \tau_k, \tag{3.11}$$

where

$$\tau_k \equiv -(\mathbf{f} \cdot \partial_k \mathbf{m}) = \left(\frac{\delta W}{\delta \mathbf{m}} \cdot \partial_k \mathbf{m}\right) \tag{3.12}$$

is the "generalized force density" that appeared first in the work of Thiele [4]. We take this calculation one step farther and write τ_k as a total divergence,

$$\tau_k = \partial_\ell \sigma_{k\ell}, \tag{3.13}$$

where $\sigma_{k\ell}$ will be called the stress tensor and it is given by the general formula [5]

$$\sigma_{k\ell} = w\delta_{k\ell} - \frac{\partial w}{\partial(\partial_\ell m_i)}\,\partial_k m_i, \tag{3.14}$$

where w is the energy functional. Equation (3.11) then reads

$$\dot{\gamma}_i = \varepsilon_{ijk}\partial_j\partial_\ell\sigma_{k\ell} \tag{3.15}$$

and proves to be fundamental for our purposes [5].

To complete this line of reasoning we must also supply an explicit expression for the stress tensor. As a first step we insert in Eq. (3.12) the effective field $\mathbf{f}$ of Eq. (2.13):

$$\begin{aligned} &\tau_k = \tau_k^e + \tau_k^a + \tau_k^b + \tau_k^m, \\ &\tau_k^e = -(\Delta\mathbf{m}\cdot\partial_k\mathbf{m}), \qquad \tau_k^a = \kappa(m_1\partial_k m_1 + m_2\partial_k m_2), \\ &\tau_k^b = -h_b\partial_k m_3, \qquad \tau_k^m = -(\mathbf{h}\cdot\partial_k\mathbf{m}). \end{aligned} \tag{3.16}$$

We then search for a tensor

$$\sigma_{k\ell} = \sigma_{k\ell}^e + \sigma_{k\ell}^a + \sigma_{k\ell}^b + \sigma_{k\ell}^m \tag{3.17}$$

that must lead to Eq. (3.16) by applying the general relation (3.13). The first three terms are simply

$$\sigma_{k\ell}^e = w_e\delta_{k\ell} - (\partial_k\mathbf{m}\cdot\partial_\ell\mathbf{m}), \qquad \sigma_{k\ell}^a = w_a\delta_{k\ell}, \qquad \sigma_{k\ell}^b = w_b\delta_{k\ell}, \tag{3.18}$$

where w_e, w_a and w_b are the energy densities defined in Eqs. (2.19) and (2.23). The construction of the magnetostatic contribution is slightly more involved but trial and error leads to

$$\sigma_{k\ell}^m = h_k b_\ell - \frac{1}{2}\mathbf{b}^2\delta_{k\ell}, \tag{3.19}$$

where the magnetic induction $\mathbf{b} = \mathbf{h} + \mathbf{m}$ is used mostly as a notational abbreviation. As usual, it is understood that the magnetic field in Eq. (3.19) is expressed in terms of the magnetization through the magnetostatic equations (2.14). A repeated application of these equations establishes the desired relation

$$\partial_\ell\sigma_{k\ell}^m = -(\mathbf{h}\cdot\partial_k\mathbf{m}) = \tau_k^m. \tag{3.20}$$

A notable feature of the derived stress tensor $\sigma_{k\ell}$ is that all but the magnetostatic contributions are symmetric under exchange of the indices k and ℓ. The asymmetry of the last term anticipates the physical fact that the orbital angular momentum and the total magnetization are not separately conserved in the presence of the magnetostatic interaction, as we shall see shortly. A further interesting property is that the preceding construction applies whether or not boundaries are present, taking into account that the magnetic induction $\mathbf{b}$ is equal to the magnetic field $\mathbf{h}$ outside the ferromagnetic material where the stress tensor reduces to

$$\sigma_{k\ell} = \sigma^m_{k\ell} = h_k h_\ell - \frac{1}{2}\mathbf{h}^2 \delta_{k\ell}, \tag{3.21}$$

which is symmetric and satisfies the continuity equation

$$\partial_\ell \sigma_{k\ell} = 0 \tag{3.22}$$

by virtue of $\boldsymbol{\nabla} \times \mathbf{h} = 0 = \boldsymbol{\nabla} \cdot \mathbf{h}$. Equation (3.22) is consistent with a vanishing Thiele force density outside the material.

4. Conservation laws

The occurrence of ambiguities in the canonical definition of conservation laws has already received considerable attention. Slonczweski [22] was apparently the first to recognize that the usual definition of linear momentum fails for magnetic bubbles with a nonvanishing winding number. Haldane [23] and Volovik [24] also addressed the question from different perspectives. But we believe that a simple as well as complete resolution of this issue was given only in some recent work [5] where the linear and angular momentum were expressed as moments of the topological vorticity (3.1). Since the available studies address strictly 2D and 3D models, our aim here is to establish unambiguous conservation laws in the context of the quasi-2D geometry appropriate for the description of ferromagnetic films.

We consider the geometry of Fig. 1 where a film of constant thickness d extends to infinity in the (x_1, x_2) plane and the easy axis is perpendicular to the film. Therefore the relevant symmetries are (i) translations in the (x_1, x_2) plane, and (ii) azimuthal rotations around the third axis. We shall show that the corresponding conservation laws are the moments

$$I_\mu = \int x_\mu \gamma_3 dV, \qquad \mu = 1 \quad \text{or} \quad 2, \tag{4.1}$$

which are related to the linear momentum, and the third component of the total angular momentum

$$J = \ell + \mu; \qquad \ell = \frac{1}{2}\int \rho^2 \gamma_3 dV, \qquad \mu = \int (m_3 - 1) dV, \tag{4.2}$$

where $\rho^2 = x_1^2 + x_2^2$ and hence the "orbital" angular momentum ℓ is also expressed as a moment of the vorticity; μ is the total magnetic moment along the easy axis, except that we have subtracted the trivial contribution from the ground state so that μ is finite and negative. It should be noted that all volume integrals in Eqs. (4.1) and (4.2) extend over region I of Fig. 1.

Although the conservation laws quoted above have a similar appearance with those derived for strictly 2D models [5], a proof of their validity is not obvious because of potential boundary effects. We consider first the time evolution of the moments (4.1),

$$\dot{I}_\mu = \int x_\mu \dot{\gamma}_3 dV = \varepsilon_{3jk} \int x_\mu \partial_j \partial_\ell \sigma_{k\ell} dV, \tag{4.3}$$

where we have used the fundamental relation (3.15) applied for $i = 3$. Notation is organized by asserting that Greek indices $\mu, \nu, \ldots$ assume only the two distinct values 1 and 2, corresponding to the two spatial coordinates x_1 and x_2, while Latin indices $i, j, \ldots$ assume all three values, as usual. We further introduce the 2D antisymmetric tensor $\varepsilon_{\mu\nu}$, whose elements are $\varepsilon_{11} = 0 = \varepsilon_{22}$ and $\varepsilon_{12} = 1 = -\varepsilon_{21}$, and invoke the summation convention for repeated indices without exception. Then

$$\dot{I}_\mu = \varepsilon_{\nu\lambda} \int x_\mu \partial_\nu \partial_\ell \sigma_{\lambda\ell} dV = \varepsilon_{\nu\lambda} \int [\partial_\nu (x_\mu \partial_\ell \sigma_{\lambda\ell}) - \delta_{\mu\nu} \partial_\ell \sigma_{\lambda\ell}] dV, \tag{4.4}$$

where both terms in the integrand are in the form of a total divergence. Since the film extends to infinity in the x_1 and x_2 directions, the first integral vanishes for either $\nu = 1$ or 2 provided that the magnetization exhibits a reasonable behavior at large x_1 or x_2. By reasonable we mean that the magnetization approaches its ground-state value sufficiently fast so that the energy of the configuration is finite. Then we may write

$$\dot{I}_\mu = -\varepsilon_{\mu\lambda} \int \partial_\ell \sigma_{\lambda\ell} dV, \tag{4.5}$$

where the integrand is also a total divergence but the integral need not vanish because the Latin index ℓ is summed over all three values, $\ell = 1, 2$ and 3, and may lead to a nonvanishing contribution from the film boundaries, namely

$$\dot{I}_\mu = -\varepsilon_{\mu\lambda} \left[\int\limits_{x_3 = d/2} \sigma_{\lambda 3} dx_1 dx_2 - \int\limits_{x_3 = -d/2} \sigma_{\lambda 3} dx_1 dx_2 \right], \tag{4.6}$$

where the tensor elements $\sigma_{\lambda 3}$ are evaluated right inside the boundaries and are certainly not equal to zero.

However we may now return to the explicit form of the stress tensor given in Section 3 and apply it for $\sigma_{\lambda 3}$ with $\lambda \neq 3$ to obtain

$$\sigma_{\lambda 3} = -(\partial_\lambda \mathbf{m} \cdot \partial_3 \mathbf{m}) + h_\lambda b_3, \tag{4.7}$$

which must be evaluated at the boundaries of the film where $\partial_3 \mathbf{m} = 0$ on account of the unpinned boundary condition (2.22). Hence

$$\sigma_{\lambda 3}(x_1, x_2, x_3 = \pm d/2) = h_\lambda b_3, \tag{4.8}$$

where we further note that the combination of fields $h_\lambda b_3$, with $\lambda = 1$ or 2, is continuous across the boundaries thanks to the familiar boundary conditions of magnetostatics. The double integrals in Eq. (4.6) may thus be evaluated right outside the boundaries where the stress tensor satisfies the continuity equation (3.22). An application of the divergence theorem in region II yields

$$0 = \int\limits_{\mathrm{II}} \partial_\ell \sigma_{\lambda\ell} dV = -\int\limits_{x_3=d/2} \sigma_{\lambda 3} dx_1 dx_2, \tag{4.9}$$

and a similar relation for region III. The net conclusion is that both integrals in Eq. (4.6) vanish and

$$\dot{I}_\mu = 0, \tag{4.10}$$

which is the desired result. We shall defer discussion of the interesting physical consequences of Eq. (4.10) until a corresponding result is obtained for the angular momentum.

The time evolution of the orbital angular momentum is governed again by the fundamental relation (3.15). The analog of Eq. (4.4) now reads

$$\dot{\ell} = \frac{1}{2}\varepsilon_{\nu\lambda} \int \rho^2 \partial_\nu \partial_\ell \sigma_{\lambda\ell} dV = \frac{1}{2}\varepsilon_{\nu\lambda} \int [\partial_\nu(\rho^2 \partial_\ell \sigma_{\lambda\ell}) - 2x_\nu \partial_\ell \sigma_{\lambda\ell}] dV, \tag{4.11}$$

where the first integral in the last step of Eq. (4.11) vanishes for both $\nu = 1$ and 2:

$$\dot{\ell} = -\varepsilon_{\nu\lambda} \int x_\nu \partial_\ell \sigma_{\lambda\ell} dV = \varepsilon_{\nu\lambda} \int [\sigma_{\lambda\nu} - \partial_\ell(x_\nu \sigma_{\lambda\ell})] dV. \tag{4.12}$$

Recalling that the volume integration extends over region I we write

$$\int\limits_{\mathrm{I}} \partial_\ell(x_\nu \sigma_{\lambda\ell}) dV = \int\limits_{x_3=d/2} x_\nu \sigma_{\lambda 3} dx_1 dx_2 - \int\limits_{x_3=-d/2} x_\nu \sigma_{\lambda 3} dx_1 dx_2, \tag{4.13}$$

where the double integrals may be calculated either above or below the film surfaces because the tensor elements $\sigma_{\lambda 3}$ given by Eq. (4.8) are continuous across the boundaries. An argument similar to that used in Eq. (4.9) then leads to

$$\int\limits_{x_3=d/2} x_\nu \sigma_{\lambda 3} dx_1 dx_2 = -\int\limits_{\mathrm{II}} \sigma_{\lambda\nu} dV, \tag{4.14}$$

and

$$\int\limits_{x_3=-d/2} x_\nu \sigma_{\lambda 3} dx_1 dx_2 = \int\limits_{\mathrm{III}} \sigma_{\lambda\nu} dV. \tag{4.15}$$

Therefore Eq. (4.13) may be rewritten as

$$\int\limits_{\mathrm{I}} \partial_\ell (x_\nu \sigma_{\lambda\ell}) dV = -\int\limits_{\mathrm{II}} \sigma_{\lambda\nu} dV - \int\limits_{\mathrm{III}} \sigma_{\lambda\nu} dV, \tag{4.16}$$

where the right-hand side is symmetric under exchange of the indices ν and λ because the stress tensor is symmetric outside the film. Hence inserting Eq. (4.16) in Eq. (4.12) yields a vanishing contribution, because of the contraction with the antisymmetric tensor $\varepsilon_{\nu\lambda}$, and

$$\dot{\ell} = \int\limits_{\mathrm{I}} \varepsilon_{\nu\lambda} \sigma_{\lambda\nu} dV. \tag{4.17}$$

To summarize, if the magnetostatic interaction were absent, the stress tensor would be symmetric in all regions and Eq. (4.17) would lead to a conserved orbital angular momentum ($\dot{\ell} = 0$). In general, using the complete stress tensor given in Eqs. (3.18) and (3.19),

$$\varepsilon_{\nu\lambda} \sigma_{\lambda\nu} = \varepsilon_{\nu\lambda} h_\lambda b_\nu = \varepsilon_{\nu\lambda} h_\lambda m_\nu, \tag{4.18}$$

and

$$\dot{\ell} = \int (m_1 h_2 - m_2 h_1) dV, \tag{4.19}$$

so that the orbital angular momentum is not by itself conserved.

Nevertheless a conservation law is obtained by including the total magnetic moment μ of Eq. (4.2) whose time derivative is computed by applying directly the Landau-Lifshitz equation (2.15) to write

$$\dot{\mu} = \int \dot{m}_3 dV = -\int (\mathbf{m} \times \mathbf{f})_3 dV. \tag{4.20}$$

Now taking into account the explicit expression for the effective field $\mathbf{f}$ of Eq. (2.13) we find that the contributions from the anisotropy and bias fields drop out from Eq. (4.20) and

$$\dot{\mu} = -\int (\mathbf{m} \times \Delta \mathbf{m} + \mathbf{m} \times \mathbf{h})_3 dV. \tag{4.21}$$

To compute the exchange contribution we note that

$$\int (\mathbf{m} \times \Delta \mathbf{m}) dV = \int \partial_i (\mathbf{m} \times \partial_i \mathbf{m}) dV = \oint (\mathbf{m} \times \partial_i \mathbf{m}) dS_i, \tag{4.22}$$

where the surface integral vanishes because of the unpinned boundary condition (2.22). Therefore

$$\dot{\mu} = -\int (\mathbf{m} \times \mathbf{h})_3 dV = -\int (m_1 h_2 - m_2 h_1) dV. \tag{4.23}$$

Comparing this result with Eq. (4.19) establishes that

$$\dot{J} = 0, \tag{4.24}$$

or that the total angular momentum $J = \ell + \mu$ is conserved.

Having thus demonstrated the validity of the conservation laws (4.1) and (4.2) we now turn to the discussion of their physical content. We first note that these conservation laws are free of all ambiguities even for configurations with a nontrivial topological structure. Suffice it to say that the potential nondifferentiability of the canonical variables Π and Φ does not affect Eqs. (4.1) and (4.2) because they are both expressed in terms of the vorticity which can be calculated directly from the magnetization through Eq. (3.1). A detailed discussion of this issue may be found in [5] within a strictly 2D context and applies here with minor modifications. Hence we will simply list the important points adapted to the present quasi-2D situation.

The conserved moments (4.1) are related to the linear momentum $\mathbf{p} = (p_1, p_2)$ by

$$p_\mu = \varepsilon_{\mu\nu} I_\nu, \qquad \{p_\mu, \mathbf{m}\} = -\partial_\mu \mathbf{m}, \tag{4.25}$$

where the Poisson-bracket relation establishes that $\mathbf{p}$ is indeed the generator of translations in the (x_1, x_2) plane. However $\mathbf{p}$ cannot be interpreted as ordinary momentum for two related reasons. First, the Poisson bracket of its two components,

$$\{p_1, p_2\} = -4\pi d Q, \tag{4.26}$$

does not vanish except for a vanishing winding number. Second, under translations in the plane, $x_1 \to x_1 + c_1$ and $x_2 \to x_2 + c_2$, the moments transform according to

$$I_\mu \to I_\mu + 4\pi d Q c_\mu, \tag{4.27}$$

which is a consequence of definition (4.1) and Eq. (3.10). The nontrivial transformation of the linear momentum (4.25) implied by Eq. (4.27) is surely an unusual property because one would expect the momentum to remain unchanged under a rigid translation. Nevertheless the above properties suggest a formal analogy with the familiar electron motion in a uniform magnetic field, the role of the latter being played here by the winding number.

Therefore, when $Q \neq 0$, a more useful interpretation of the conserved moments is obtained through the guiding center coordinates

$$R_\mu = \frac{\displaystyle\int x_\mu \gamma_3 dV}{\displaystyle\int \gamma_3 dV} = \frac{I_\mu}{4\pi d Q}, \qquad \mu = 1 \quad \text{or} \quad 2, \tag{4.28}$$

which are conserved and transform as $(R_1, R_2) \to (R_1 + c_1, R_2 + c_2)$ under a rigid translation in the plane $(x_1, x_2) \to (x_1 + c_1, x_2 + c_2)$. The latter property suggests that the 2D vector $\mathbf{R} = (R_1, R_2)$ may be interpreted as the mean position of a magnetic bubble with $Q \neq 0$ in a ferromagnetic film, and its conservation implies that such a bubble cannot be found in a free translational motion. In other words, $Q \neq 0$ bubbles are always spontaneously pinned or frozen within the ferromagnetic medium provided that external perturbations are absent; in analogy with electrons undergoing a 2D cyclotron motion in a uniform magnetic film, in the absence of electric fields.

The physical meaning of the orbital angular momentum ℓ defined in Eq. (4.2) is also unusual, for it actually provides a measure of the size of a configuration with $Q \neq 0$. More precisely, one may define a mean squared radius from

$$r^2 = \frac{\displaystyle\int [(x_1 - R_1)^2 + (x_2 - R_2)^2] \gamma_3 dV}{\displaystyle\int \gamma_3 dV} = \frac{\ell}{2\pi d Q} - \mathbf{R}^2, \tag{4.29}$$

which is directly proportional to ℓ when the latter is defined with respect to the guiding center ($\mathbf{R} = 0$). Note that we use the abbreviated 2D notation $\mathbf{R} = (R_1, R_2)$ and $\mathbf{R}^2 = R_1^2 + R_2^2$. The radius r of Eq. (4.29) plays an important role in our theoretical development but does not, in general, coincide with the naive radius at which the third component of the magnetization vanishes ($m_3 = 0$). One should also note that r would be a conserved quantity in the absence of the magnetostatic interaction because the orbital angular momentum would then be by itself conserved.

In order to pursue further a meaningful discussion of dynamics, one must first ascertain the existence of interesting static solutions of the Landau-Lifshitz equation such as magnetic bubbles with a nonvanishing winding number; an issue addressed in the following two sections. We shall return to a more detailed study of the implications of the derived conservation laws for dynamics in Section 7.

5. Virial theorems

A simple scaling argument due to Derrick [13] leads to a virial relation that must be satisfied by any finite-energy static solution of a nonlinear field theory. Since Derrick's relation is mainly used in the literature to establish the nonexistence of nontrivial static solutions, it is of some interest to demonstrate how the present theory evades its potential consequences and leads to the observed wealth of magnetic bubbles with practically any winding number [1]. However a generalization of the original scaling argument to the present case is not completely straightforward, because of the film boundaries, and is given below.

Static solutions are stationary points of the energy functional $W = W(\mathbf{m})$ provided that the constraint $\mathbf{m}^2 = 1$ is taken into account. For instance, one may use the spherical variables (2.35) to write

$$\frac{\delta W}{\delta \Pi} = 0 = \frac{\delta W}{\delta \Phi}, \tag{5.1}$$

which are the static versions of the Hamilton equations (2.36). In this section, we shall neither write out nor solve the above equations explicitly but merely use them to derive some general relations.

For the moment, let us ignore the film boundaries and assume that the medium extends to infinity in all directions. We may then apply Derrick's scaling argument in a straightforward fashion. Suppose that $\Pi = \Pi(\mathbf{x})$ and $\Phi = \Phi(\mathbf{x})$ is a solution of Eqs. (5.1) with (finite) energy $W = W_e + W_a + W_b + W_m$. The energy of the configuration $\Pi(\zeta\mathbf{x})$ and $\Phi(\zeta\mathbf{x})$, where ζ is some constant, is then given by

$$W(\zeta) = \frac{1}{\zeta} W_e + \frac{1}{\zeta^3}(W_a + W_b + W_m). \tag{5.2}$$

By our hypothesis $\zeta = 1$ is a stationary point of $W(\zeta)$ and thus $W'(\zeta = 1) = 0$ or

$$W_e + 3(W_a + W_b + W_m) = 0, \tag{5.3}$$

which is a virial relation that must be satisfied by any static solution with finite energy. Since all pieces of the energy are positive definite, one must conclude from Eq. (5.3) that nontrivial static solutions with finite energy do not exist in a 3D ferromagnetic continuum without boundaries.

The preceding derivation of virial relation (5.2) is clearly inapplicable in the presence of boundaries. We thus seek to obtain the analog of this relation for the film geometry of Fig. 1 by a method that was already employed in the simpler context of Ref. [5] and leads to a series of virial theorems, Derrick's relation being the simplest example. An alternative form of the Thiele force density is given by

$$\tau_k = \frac{\delta W}{\delta \Pi}\partial_k \Pi + \frac{\delta W}{\delta \Phi}\partial_k \Phi = \partial_\ell \sigma_{k\ell} \tag{5.4}$$

and vanishes for static solutions satisfying Eqs. (5.1). Therefore the stress tensor satisfies the continuity equation

$$\partial_\ell \sigma_{k\ell} = 0 \tag{5.5}$$

within the ferromagnetic medium. Recalling that the stress tensor satisfies the continuity equation outside the film even for time-dependent solutions, see Eq. (3.22), we conclude that static solutions satisfy Eq. (5.5) everywhere.

A series of virial relations may now be derived by taking suitable moments of Eq. (5.5) and by a systematic application of the divergence theorem. The simplest possibility is

$$\int_V x_j \partial_\ell \sigma_{k\ell} dV = 0, \tag{5.6}$$

where the integration extends over some volume V that is left unspecified for the moment. The divergence theorem then yields

$$\int_V \sigma_{ij} dV = \oint_S x_j \sigma_{i\ell} dS_\ell, \tag{5.7}$$

where we have effected a trivial rearrangement of indices and S is the surface surrounding the volume V. It is understood that the region of integration is such that the surface S does not cross the film boundaries because of potential discontinuities that may render the divergence theorem invalid.

Thus we proceed with an application of Eq. (5.7) in several steps. First we consider the subset of relations obtained by restricting the indices i and j to the values 1 or 2. Using our standard convention we write

$$\int_V \sigma_{\mu\nu} dV = \oint_S x_\nu \sigma_{\mu\ell} dS_\ell, \tag{5.8}$$

where $\mu, \nu = 1$ or 2, and subsequently apply this relation to each region I, II or III separately:

$$\begin{aligned} \int_{\mathrm{I}} \sigma_{\mu\nu} dV &= S^{+}_{\mu\nu} - S^{-}_{\mu\nu}, \\ \int_{\mathrm{II}} \sigma_{\mu\nu} dV &= -S^{+}_{\mu\nu}, \\ \int_{\mathrm{III}} \sigma_{\mu\nu} dV &= S^{-}_{\mu\nu}, \end{aligned} \tag{5.9}$$

where

$$S^{\pm}_{\mu\nu} \equiv \int_{x_3 = \pm d/2} x_\nu \sigma_{\mu 3} dx_1 dx_2 = \int_{x_3 = \pm d/2} x_\nu h_\mu b_3 dx_1 dx_2. \tag{5.10}$$

Here we have recalled the boundary values of the tensor elements $\sigma_{\mu 3}$ from Eq. (4.8) which are continuous across each boundary for $\mu = 1$ or 2. In fact, the last two equations in (5.9) coincide with Eqs. (4.14) and (4.15) obtained in our earlier discussion of conservation laws because the stress tensor satisfies the continuity equation outside the film even for time-dependent fields. However the first equation in (5.9) applies only to static solutions. An immediate consequence of all three equations is the set of relations

$$\int_{\text{all volume}} \sigma_{\mu\nu} dV = 0; \qquad \mu, \nu = 1 \quad \text{or} \quad 2, \tag{5.11}$$

where explicit surface contributions are no longer present. A special case that emphasizes the role of the magnetostatic interaction is obtained by contracting both sides of Eq. (5.11) with the 2D antisymmetric tensor,

$$\int \varepsilon_{\nu\mu} \sigma_{\mu\nu} dV = \int (m_1 h_2 - m_2 h_1) dV = 0, \tag{5.12}$$

a relation that is consistent with Eqs. (4.19) and (4.23) since both the orbital angular momentum ℓ and the total magnetic moment μ are time independent in a static solution.

The absence of explicit surface terms in Eq. (5.11) is not surprising because scaling arguments of the Derrick variety continue to apply in the x_1 and x_2 directions. Specifically Eq. (5.11) may be arrived at also by performing the linear transformation $x_1 \to \zeta_{11} x_1 + \zeta_{12} x_2$ and $x_2 \to \zeta_{21} x_1 + \zeta_{22} x_2$ in a static solution and by demanding that the resulting energy $W = W(\zeta)$ be stationary at $\zeta_{11} = 1 = \zeta_{22}$ and $\zeta_{12} = 0 = \zeta_{21}$. However the situation is different when one or both indices i, j in Eq. (5.7) are equal to 3.

Actually some useful information on the latter case can be obtained directly from the continuity equation (5.5) which is written as

$$\partial_\nu \sigma_{i\nu} + \partial_3 \sigma_{i3} = 0 \tag{5.13}$$

and implies that the double integrals $\int \sigma_{i3} dx_1 dx_2$, with $i = 1$, 2 or 3, are independent of x_3 but may assume different values in regions I, II, or III. In fact, all integrals vanish outside the film because they can be calculated at large $|x_3|$ where the tensor elements vanish. For $i = \mu = 1$ or 2 the integrals vanish also inside the film thanks to Eq. (4.9):

$$\int \sigma_{\mu 3} dx_1 dx_2 = 0, \qquad \mu = 1 \quad \text{or} \quad 2, \tag{5.14}$$

for any x_3. On the other hand,

$$\int \sigma_{33} dx_1 dx_2 = \begin{cases} 0, & |x_3| > d/2, \\ s, & -d/2 < x_3 < d/2, \end{cases} \tag{5.15}$$

where s is constant throughout the film but need not vanish. Collecting the above information we may also write

$$\int_{\text{all volume}} \sigma_{33} dV = sd, \tag{5.16}$$

which should be contrasted with Eq. (5.11) where the right-hand side vanishes.

We have thus derived a number of virial relations that must be satisfied by any static solution. We have also gathered sufficient information to make contact with relation (5.3) obtained for a strictly 3D medium. Indeed Eqs. (5.11) and (5.16) may be combined to yield

$$\int \text{tr}\sigma dV = sd, \tag{5.17}$$

where the integration extends over all volume, $\text{tr}\sigma = \sigma_{11} + \sigma_{22} + \sigma_{33}$ is the trace of the stress tensor, s the constant defined from Eq. (5.15), and d the film thickness. The trace is calculated by using the explicit expression of the stress tensor from Eqs. (3.18) and (3.19):

$$\text{tr}\sigma = w_e + 3(w_a + w_b) + (\mathbf{h} \cdot \mathbf{b}) - \frac{3}{2}\mathbf{b}^2, \tag{5.18}$$

where w_e, w_a and w_b are the exchange, anisotropy and bias energy densities. We may further insert in Eq. (5.18) the magnetic induction $\mathbf{b} = \mathbf{h} + \mathbf{m}$ to write

$$\text{tr}\sigma = w_e + 3(w_a + w_b) - \frac{1}{2}\mathbf{h}^2 + 4\left(-\frac{1}{2}\mathbf{h} \cdot \mathbf{m}\right) - \frac{3}{2}\mathbf{m}^2, \tag{5.19}$$

where the magnetostatic energy density appears both in the form entering Eq. (2.25) and that of Eq. (2.32), while in the last term we must set $\mathbf{m}^2 = 1$ within the film and zero outside. Therefore a more explicit form of Eq. (5.17) reads

$$W_e + 3[W_a + W_b + (W_m - W_m^{(0)})] = sd, \tag{5.20}$$

where we recognize the various pieces of the energy, as in relation (5.3), and $W_m^{(0)}$ originates in the last term of Eq. (5.19) and is equal to the magnetostatic energy of the ground state configuration $\mathbf{m}_0 = (0, 0, 1)$.

Virial relation (5.20) differs from (5.3) in two significant ways. First, a surface term appears in the right-hand side which is entirely due to the film geometry and is generally different from zero. Second, the (infinite) magnetostatic energy of the ground state, $W_m^{(0)}$, is subtracted out. Now implicit in the derivation of (5.3) was the assumption that the magnetostatic field vanishes at large distances, in all directions, so that the energy W_m is finite. This assumption is clearly false in a ferromagnetic film because $\mathbf{h} = -\mathbf{m}_0$ at large x_1 and x_2 and thus both W_m and $W_m^{(0)}$ are infinite. Nevertheless the difference $W_m - W_m^{(0)}$ appearing in Eq. (5.20) is expected to be finite for reasonable solutions. Furthermore this difference is not positive definite. In fact, using Eqs. (2.25) (2.32), we have $W_m = -\int (\mathbf{h} \cdot \mathbf{m} + \frac{1}{2}\mathbf{h}^2)\, dV$ so that

$$W_m - W_m^{(0)} = -\int (\mathbf{h} \cdot \mathbf{m} + \frac{1}{2}\mathbf{h}^2 + \frac{1}{2}\mathbf{m}^2)\, dV = -\int (\mathbf{h} + \mathbf{m})^2\, dV \leq 0, \tag{5.21}$$

with the equal sign when $\mathbf{h} = -\mathbf{m}$, that is for a uniform configuration only. So, the uniform magnetization configuration has maximum magnetostatic energy. As a result the magnetostatic field favors expansion of a domain with magnetization opposite to that of the ground state, i.e. it favors expansion of the bubble domains. This is balanced by the exchange, anisotropy and bias fields to produce a stable bubble of definite radius [3]. Therefore virial relation (5.20), unlike (5.3), does not a priori exclude nontrivial static solutions in a ferromagnetic film, irrespectively of the sign of the surface contribution in the right-hand side. An explicit example is worked out in the following section where s is negative and Eq. (5.20) is verified.

6. The fundamental magnetic bubble

The construction of static solutions with a nonvanishing winding number is an issue of significant practical interest and occupied most of the early studies of magnetic bubbles [1, 2]. Because of the long-range nature of the mangetostatic field and the related effects of finite film thickness, writing out the static equations (5.1) explicitly leads to a rather complex system that is not particularly illuminating. Hence the question was addressed through approximate solutions in the limit of a large quality factor κ [3], variational methods [25], and numerical simulations in the important special case of the fundamental ($Q = 1$) bubble [26]. However, in order to illustrate some basic aspects of our theoretical development, we shall need some detailed information on the profile of a bubble that is not easily accessible from the early work. We have thus decided to recalculate the $Q = 1$ bubble by a numerical method with a simple physical origin.

Suppose that some initial configuration with a given winding number Q evolves according to the Landau-Lifshitz equation (2.37) including dissipation. After a sufficiently long time interval precession effects are suppressed and the configuration eventually relaxes to a static solution of the Landau-Lifshitz equation with the same winding number. Since our aim in this section is only to obtain static solutions, the process may be accelerated using Eq. (2.37) with a very large dissipation constant λ. On introducing the rescaled time variable $\tau = t/\lambda$, the $\lambda \to \infty$ limit of Eq. (2.37) reads

$$\frac{\partial \mathbf{m}}{\partial \tau} + \mathbf{m} \times (\mathbf{m} \times \mathbf{f}) = 0, \qquad \mathbf{m}^2 = 1. \tag{6.1}$$

In view of Eq. (2.38) the energy decreases when the configuration evolves according to either Eq. (2.37) or its fully dissipative limit (6.1). The advantage of the latter is that it suppresses transients and leads to equilibrium with reasonable speed. Of course, the calculated static solution is independent of the details of the initial configuration provided that the winding number is kept fixed. Thus the initial condition may be chosen more or less at convenience and convergence may be improved by incorporating any a priori information on the expected static solution.

A substantial simplification occurs in the case of the fundamental bubble because of its *strict* axial symmetry; that is, *invariance* under a simultaneous rotation in the (x_1, x_2) plane and a corresponding azimuthal rotation of the magnetization. It is then convenient to use cylindrical coordinates defined from

$$x_1 = \rho \cos \phi, \qquad x_2 = \rho \sin \phi, \qquad x_3 = z. \tag{6.2}$$

A strictly axially symmetric configuration is of the general form

$$m_1 + i m_2 = (m_\rho + i m_\phi) e^{i\phi}, \qquad m_3 = m_z \tag{6.3}$$

where the radial (m_ρ), azimuthal (m_ϕ) and longitudinal (m_z) components are functions of only ρ and z,

$$m_\rho = m_\rho(\rho, z), \qquad m_\phi = m_\phi(\rho, z), \qquad m_z = m_z(\rho, z), \tag{6.4}$$

while they continue to satisfy the constraint

$$m_\rho^2 + m_\phi^2 + m_z^2 = 1. \tag{6.5}$$

The dissipative equation (6.1) becomes effectivelly two-dimensional and a significant simplification of the numerical problem results.

Specifically, when ansatz (6.3) is inserted in Eq. (6.1), the resulting equation retains the same form except that the three-component vector $\mathbf{m} = (m_1, m_2, m_3)$ is formally replaced by (m_ρ, m_ϕ, m_z) and the effective field $\mathbf{f}$ by (f_ρ, f_ϕ, f_z) with

$$\begin{aligned} f_\rho &= \Delta m_\rho - \frac{m_\rho}{\rho^2} - \kappa m_\rho + h_\rho, \\ f_\phi &= \Delta m_\phi - \frac{m_\phi}{\rho^2} - \kappa m_\phi + h_\phi, \\ f_z &= \Delta m_z + h_b + h_z, \end{aligned} \tag{6.6}$$

where the Laplace operator is reduced to

$$\Delta = \frac{\partial^2}{\partial \rho^2} + \frac{1}{\rho}\frac{\partial}{\partial \rho} + \frac{\partial^2}{\partial z^2}, \tag{6.7}$$

h_b is the bias field, and h_ρ, h_ϕ and h_z are the polar components of the magnetostatic field. Actually, the azimuthal component vanishes because

$$\boldsymbol{\nabla} \cdot \mathbf{m} = \frac{\partial m_\rho}{\partial \rho} + \frac{m_\rho}{\rho} + \frac{\partial m_z}{\partial z} \tag{6.8}$$

and hence the magnetostatic potential is a function of only ρ and z; $\psi = \psi(\rho, z)$. Therefore

$$h_\rho = -\frac{\partial \psi}{\partial \rho}, \qquad h_\phi = 0, \qquad h_z = -\frac{\partial \psi}{\partial z}, \tag{6.9}$$

and the polar components of the magnetic induction are

$$b_\rho = h_\rho + m_\rho, \qquad b_\phi = m_\phi, \qquad b_z = h_z + m_z. \tag{6.10}$$

For future reference we also quote some discrete symmetries of the reduced system of equations. First, given a static solution of the form (6.4), the configuration

$$m_\rho(\rho, z), \qquad -m_\phi(\rho, z), \qquad m_z(\rho, z) \tag{6.11}$$

is also a solution. Second, the parity relations

$$m_\rho(\rho,z) = -m_\rho(\rho,-z), \qquad m_\phi(\rho,z) = m_\phi(\rho,-z), \qquad m_z(\rho,z) = m_z(\rho,-z),$$
$$h_\rho(\rho,z) = -h_\rho(\rho,-z), \qquad h_\phi = 0, \qquad h_z(\rho,z) = h_z(\rho,-z), \tag{6.12}$$

are compatible with the evolution equation (6.1). In other words, if Eq. (6.1) is solved with an initial condition satisfying relations (6.12), the resulting static solution will satisfy the same relations.

To complete the description of strictly axially symmetric configurations we return briefly to the conservation laws (4.1) and (4.2). The relevant third component of the vorticity reduces to

$$\gamma_3 = \frac{1}{\rho}\frac{\partial m_z}{\partial \rho}. \tag{6.13}$$

Therefore the winding number calculated from Eq. (3.10) is given by

$$Q = \frac{1}{2}\int_0^\infty \frac{\partial m_z}{\partial \rho} d\rho = \frac{1}{2}[m_z(\infty,z) - m_z(0,z)] = 1, \tag{6.14}$$

provided that the magnetization approaches its ground-state value $m_z = 1$ at infinity and the value $m_z = -1$ at the origin. We further note the trivial fact that the moments I_μ vanish and the guiding center coincides with the origin of the coordinate system. Finally the orbital angular momentum is computed from Eqs. (4.2) and (6.13),

$$\ell = \frac{1}{2}\int_{-d/2}^{d/2} dz \int_0^\infty \frac{\partial m_z}{\partial \rho} 2\pi\rho^2 d\rho = -\int_{-d/2}^{d/2} dz \int_0^\infty (m_z - 1) 2\pi\rho d\rho, \tag{6.15}$$

where we have performed a partial integration taking into account that $m_z = 1$ at infinity. We then recognize in the right-hand side of Eq. (6.15) the total magnetic moment μ of Eq. (4.2). Hence $\ell = -\mu$ and

$$J = \ell + \mu = 0. \tag{6.16}$$

As expected, the total angular momentum vanishes for a strictly axially symmetric configuration. A related fact is that the radius r calculated from Eq. (4.29) with $\mathbf{R} = 0$ and $\ell = -\mu$ satisfies the relation

$$\mu = -2\pi d r^2, \tag{6.17}$$

which could also be arrived at by considering a crude model of a bubble where the magnetization points toward the north pole, $\mathbf{m} = (0,0,1)$, for $\rho > r$ and toward the south pole, $\mathbf{m} = (0,0,-1)$, for $\rho < r$.

A. The numerical algorithm

Eq. (6.1) is the starting point for the derivation of a numerical relaxation algorithm for the calculation of static solutions. For the calculation of the fundamental bubble we shall use the magnetization components (6.4) taking advantage of its axial symmetry, so that the relaxation equations become effectively two-dimensional.

Although the principle of the method is very simple, an efficient solution of the initial-value problem posed in Eq. (6.1) confronts us with a nontrivial numerical task; at every step of the time evolution one must solve the Poisson equation (2.27) in order to determine the magnetostatic field $\mathbf{h}$ and subsequently the effective field $\mathbf{f}$ from Eq. (6.6). Calculation of the latter near the film boundaries should also take into account the unpinned boundary condition (2.22). The remainder of this subsection will be devoted to the description of the details for the numerical calculation of the fundamental bubble. Specifically we shall describe the approximations needed to obtain a discrete version of Eq. (6.1). The unpinned boundary conditions as well as those entering due to the presence of the film surface will play an important role in this procedure.

For the integration in time we use the simplest forward difference method, that is, we substitute the left hand side of Eq. (6.1) by the simple discrete version of the time derivative:

$$\frac{\partial \mathbf{m}}{\partial \tau} \approx \frac{\mathbf{m}(\tau + \delta\tau) - \mathbf{m}(\tau)}{\delta\tau}. \tag{6.18}$$

The method is stable if the time step $\delta\tau$ is chosen small enough. The values that may be used depend on the spacing of the grid that is used for the discrete version of the space derivatives of $\mathbf{m}$. We also note that the discretization (6.18) in time does not preserve the magnitude of the vector $\mathbf{m}$. Thus, following a standard practice in this thesis, we normalize the vector $\mathbf{m}$ to unity at every time step, so that the constraint of constant magnitude of the magnetization is retained [27].

A two-dimensional numerical mesh will be used to describe the spatial variations of the magnetization. A sketch of it is given in Fig. 2, where the lattice sites are denoted by black circles. In the vertical direction, taken to be the z-direction the spacing is uniform and equal to Δz. In the horizontal direction we describe the variations of $\mathbf{m}$ in the radial ρ-direction. We distinguish three regions there. First we have the region in the bulk of the bubble where the magnetization is expected to vary slowly and basically point to the south pole. Second, the outer of the bubble region where the magnetization is expected to point to the north pole. Between these two regions we have the bubble domain wall where the magnetization changes quickly

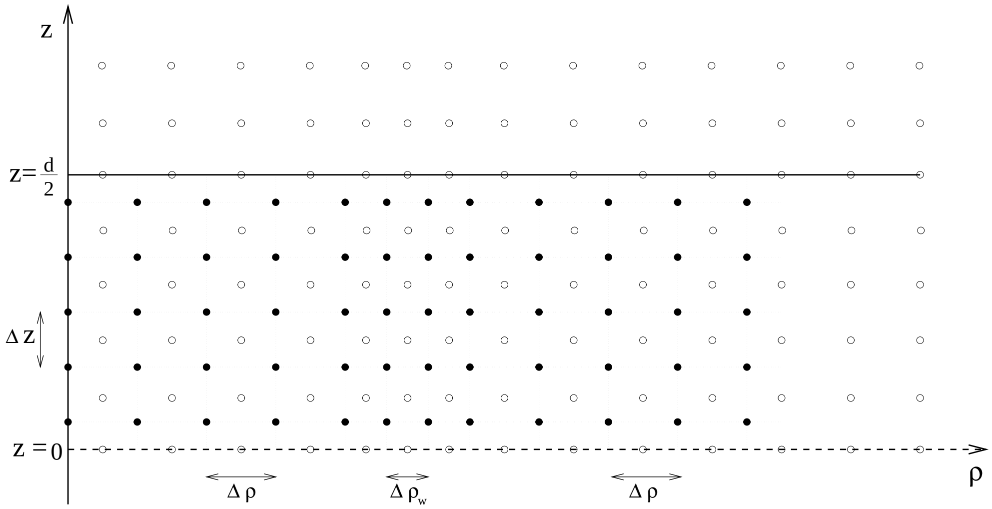

Fig. 2: A sketch of the numerical mesh used for the time evolution of the Landau-Lifshitz equation (denoted by black circles), and a corresponding mesh used for the numerical solution of the Poisson equation (2.27). The grids are both uniform in the vertical z-direction but they are both non-uniform in the horizontal ρ direction. The upper surface of the film ($z = d/2$) is denoted by a solid line on this figure. The center of the film ($z = 0$) is denoted by a dashed line. Note that the number of grid points presented here as well as the relative distances have been chosen for the sake of clarity of this sketch and do not correspond to actual number of points or relative distances used in the numerical algorithm of this section.

from the south to the north pole state. We use a lattice constant $\Delta\rho$ for the bulk of the bubble as well as for the outer of the bubble region, while a finer grid with constant $\Delta\rho_w$ is used to describe the domain wall.

Note that only the upper half of the film is drawn in Fig. 2, but the values of $\mathbf{m}$ at the lower half of the film are assumed to be known through the parity relations (6.12). The upper surface of the film is at $z = d/2$ where d is the film thickness and it is marked by a solid line while the center of the film ($z = 0$) is marked by a dashed line. Note also that no grid points are taken on the film boundary but they are only a distance $\Delta z/2$ from it. This convention will prove of significant help in the following and in particular, it will render easier and more elegant the magnetostatic field calculations.

The film is assumed infinite in the ρ-direction. So our grid has to be long enough in this direction. In fact, we use a grid approximately two times the bubble radius long, beyond the bubble domain wall. We note here that an ideal domain wall is exponentially localized and would not need such a long grid to be described. Nevertheless, the magnetostatic field entering in our calculations is a long range field and is responsible for a slow decay of the bubble domain wall magnetization to the ground state. Our grid proves long enough to overcome this difficulty and we check that the magnetization vector has reached its saturation value $\mathbf{m}_0 = (0, 0, 1)$ before the end of the numerical mesh in the ρ-direction.

In order to obtain a discrete version for the right hand side of Eq. (6.1), we need to discretize the effective field $\mathbf{f}$ of Eq. (6.6) on the numerical mesh of Fig. 2. The anisotropy and bias field terms give us no trouble and it is straightforward to be written at every lattice site. The calculation of the exchange field is a little more involved. We calculate the first derivatives of the magnetization using central differences while the second derivatives are calculated by the usual three point formula. The relevant calculations near the film surface should take into account the unpinned boundary condition (2.22). Special attention must be paid to the lattice points where the lattice spacing changes from $\Delta\rho$ to $\Delta\rho_w$. We use Taylor series expansions to find the corresponding expressions for the derivatives in ρ, at such points.

We now turn to the discussion of the calculation of the magnetostatic field which proves to be by far the most involved among the fields appearing in Eq. (6.6). This is because $\mathbf{h}$ is a non-local field and its calculation requires the solution of the boundary value Poisson problem (2.27). We first note that the magnetostatic potential Ψ as well as the field $\mathbf{h}$ have finite values, not only in the film, but also outside it. It is thus unavoidable that we solve the Poisson problem in the whole space, despite that only the values of $\mathbf{h}$ inside the film need to be known for the relaxation algorithm.

The analytical solution to the Poisson equation (2.27) is known in principle and it is given in Eq. (2.28) in integral form. So the calculation of $\mathbf{h}$ appears straightforward. But the numerical calculation of the triple integrals, involved in (2.27), is a slow process. Since the field $\mathbf{h}$ should be calculated for every time step of the relaxation algorithm, this method proves practically inapplicable. To complete this line of reasoning we also mention that the denominator in the integrand in Eq. (2.28) vanishes at the grid points, so that numerical calculation of improper integrals would be involved in the computations.

To avoid such difficulties we decided to follow a discretization scheme for the Poisson equation. We discretize Eq. (2.27) on the sites of the lattice denoted by white circles in Fig. 2. As opposed to the black circle lattice, the present one extends, not only inside, but also outside the film. We also note that the present lattice has points just on the film boundary, a fact that will be useful in applying the boundary conditions there. As a result, the two lattices are nested, that is, every point of the one lattice has four neighbors which belong to the other one.

The discretization of the Poisson equation on the lattice, results in a large number of coupled linear equations. A conjugate gradient method (CGM) has been used, which efficiently solves this system by taking successive steps to approach the exact solution. Such a method is most suitable to work in conjunction with our relaxation algorithm. This is because, the algorithm works iteratively changing the configuration only a little at every time step; so at every such step, the CGM need only take a few steps to adjust the potential Ψ to the evolving configuration. This method proves very efficient and rapid for our problem, provided that the numerical mesh is not too large.

The boundary conditions for the potential Ψ enter the calculations. We use the physical fact that Ψ vanishes away from the bubble (either inside or outside the film) provided that we subtract the uniform magnetization contribution. That is, we have the condition

$$\Psi(\mathbf{x}) - \Psi^{(0)}(\mathbf{x}) \underset{|\mathbf{x}|\to\infty}{\longrightarrow} 0. \tag{6.19}$$

where $\Psi^{(0)}$ is the uniform magnetization potential given in Eq. (2.30). Then we formally have to solve the Poisson equation with the condition (6.19). In practice, the values of Ψ would be known at the edges of the lattice $z \to \infty$, $\rho \to \infty$ by virtue of (6.19) provided that this is long enough compared to the bubble's radius. But since the potential falls off slowly away from the bubble, we would need a very large lattice in order to use (6.19). So, we decided to calculate the values of Ψ, through Eq. (2.28), at a series of sites around the bubble. Then, the Poisson equation can be solved by CGM within the region defined by this series of sites. Using such a combination of methods, the calculation of triple integrals is limited to only one series of sites on the lattice while, on the other hand, the lattice needed for the CGM can be considerably shortened. In order to end up with a lattice as short as possible for the CGM, we need calculate the values of Ψ at a series of sites as close as possible to the film surface. Nevertheless, this may result to numerical errors during the calculation of the integrals due to small denominators if we perform calculations too close to the boundaries. Thus, we perform the calculations at a horizontal series of sites a few lattice sites above the film boundary. We also perform similar calculations at a vertical series of sites, to the direction $\rho \to \infty$, away enough from the bubble. To complete this discussion we note that the relation $\Psi(z = 0) = 0$ holds true by virtue of the parity relations (6.12) and it can be used in the numerical algorithm.

On the film surface $z = d/2$, we have to apply the usual boundary conditions of electromagnetism. Namely, the potential Ψ should be continuous on crossing the film surface, while the normal to the surface component of $\mathbf{h}$ (h_z) should be discontinuous, the discontinuity being equal to the magnetization component m_z at that point. We notice that the first condition is easily applied thanks to the construction of our grid, having points just on the film surface. The second condition can be used to write the derivatives of Φ normal to the film surface and obtained the discrete version of the Poisson equation at the lattice sites on the film surface.

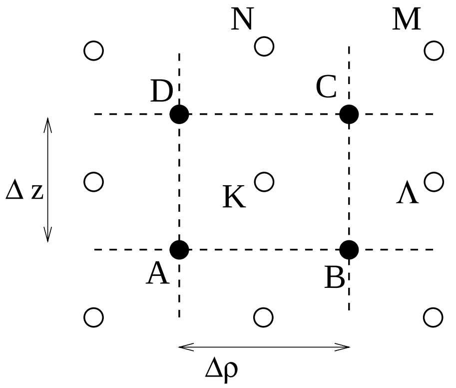

Fig. 3: Sketch of a small part of the nested lattices drawn in Fig. 2.

The description of the calculation of the magnetostatic field $\mathbf{h}$ is completed by the presentation of a discrete version of the term (6.8) used as a source term for the numerical solution of the Poisson equation. We shall also give a formula for the derivation of $\mathbf{h}$ from the numerically calculated magnetostatic potential Ψ. Note first that an initial configuration for the magnetization will be given on the black circle sites of the lattice in Fig. 2, while the divergence of $\mathbf{m}$ need be calculated on the white circle sites. To illustrate how this is done, we have drawn in Fig. 3 a small part of the two nested lattices inside the film. The derivatives of $\mathbf{m}$ at a generic white circle site K are written in terms of the values of $\mathbf{m}$ at the four neighboring black circle sites by use of the formulas

$$\begin{aligned} \frac{\partial \mathbf{m}}{\partial \rho}(\mathrm{K}) &\approx \frac{1}{2\,\Delta\rho}\,[\mathbf{m}(\mathrm{B})+\mathbf{m}(\mathrm{C})-\mathbf{m}(\mathrm{A})-\mathbf{m}(\mathrm{D})] \\ \frac{\partial \mathbf{m}}{\partial z}(\mathrm{K}) &\approx \frac{1}{2\,\Delta z}\,[\mathbf{m}(\mathrm{C})+\mathbf{m}(\mathrm{D})-\mathbf{m}(\mathrm{A})-\mathbf{m}(\mathrm{B})]\,. \end{aligned} \tag{6.20}$$

Needless to say that the constant $\Delta\rho$, in the above formulas, should be substituted by $\Delta\rho_w$ if (6.20) are applied in the domain wall region. The value of $\mathbf{m}$ at K, which is also needed in the computation of $(\boldsymbol{\nabla}\cdot\mathbf{m})(\mathrm{K})$, is approximated by

$$\mathbf{m}(\mathrm{K}) \approx \frac{1}{4}[\mathbf{m}(\mathrm{A})+\mathbf{m}(\mathrm{B})+\mathbf{m}(\mathrm{C})+\mathbf{m}(\mathrm{D})]. \tag{6.21}$$

The numerical error in formulas (6.20) (6.21) is of the order of the squared lattice spacing. These formulas are used to obtain a discrete version of $\boldsymbol{\nabla}\cdot\mathbf{m}(\mathrm{K})$ according to Eq. (6.8). The solution of the Poisson equation is then found by the CGM.

The result of the CGM algorithm is the calculation of the magnetostatic potential Ψ on the white circle lattice. But we notice now that the magnetostatic field $\mathbf{h}$ is given by the derivatives of Ψ through Eq. (6.9). So that, given Ψ on the white circle sites, we can calculate $\mathbf{h}$ on the black circle sites by use of formulas analogous to

(6.20). For instance the field at site C of Fig. 3 is given by

$$\begin{aligned} h_\rho(\mathrm{C}) &= -\frac{\partial\Psi}{\partial\rho}(\mathrm{C}) \approx -\frac{1}{2\,\Delta\rho}\,[\Psi(\Lambda)+\Psi(\mathrm{M})-\Psi(\mathrm{K})-\Psi(\mathrm{N})] \\ h_z(\mathrm{C}) &= -\frac{\partial\Psi}{\partial z}(\mathrm{C}) \approx -\frac{1}{2\,\Delta z}\,[\Psi(\mathrm{M})+\Psi(\mathrm{N})-\Psi(\mathrm{K})-\Psi(\Lambda)] \end{aligned} \tag{6.22}$$

These remarks conclude the calculation of the effective field **f** on the lattice.

Now, if Eq. (6.1) is solved for an initial condition with strict axial symmetry and winding number $Q = 1$, it will eventually lead to a static solution with the same symmetry and winding number. A simple choice of the initial configuration is given by the two-parameter family

$$m_\rho = 0, \qquad m_\phi = \pm\mathrm{sech}\,u, \qquad m_z = \tanh u, \tag{6.23}$$

with

$$u = \ln(\rho/\rho_0) + (\rho-\rho_0)/\delta_0, \tag{6.24}$$

which coincides with the variational ansatz employed by DeBonte [25] treating the constants ρ_0 and δ_0 as variational parameters. The constant ρ_0 is the naive radius of the bubble, i.e., the radius at which the third component of the magnetization vanishes, while both ρ_0 and δ_0 provide a measure of the wall width δ_w in a picture where the bubble is viewed as a curved domain wall:

$$\frac{1}{\delta_w} = \left.\frac{du}{d\rho}\right|_{\rho=\rho_0} = \frac{1}{\rho_0} + \frac{1}{\delta_0}. \tag{6.25}$$

On this occasion we recall that the width of an ideal (straight) domain wall in an infinite medium is

$$\Delta_w = \sqrt{\frac{A}{K}} \quad \text{or} \quad \frac{1}{\sqrt{\kappa}} \tag{6.26}$$

in the original or rationalized units, respectively (see Section 2). Needless to say, for our purposes the constants ρ_0 and δ_0 need not be determined variationally because the relaxation algorithm should lead to the true static solution for any choice of these parameters. However convergence may be accelerated when configuration (6.23) is as close as possible to the true bubble.

The description of the initial ansatz is completed noting that the ± freedom in Eq. (6.23) reflects the discrete symmetry (6.11). The specific choice of sign in m_ϕ will be referred to as the polarity of the bubble, the winding number being the same ($Q = 1$) for either polarity. Finally configuration (6.23) is independent of z and trivially satisfies the parity relations (6.12). Therefore the anticipated static solution will satisfy the same relations, even though it will develop a nontrivial z dependence.

At this point, one must specify the true parameters of the problem, namely the quality factor κ, the bias field h_b and the film thickness d. We have aimed at providing an illustration where the bubble radius is roughly equal to the film thickness and have thus arrived at the specific values (in rationalized units)

$$\kappa = 2, \qquad h_b = 0.32, \qquad d = 16\Delta_w = \frac{16}{\sqrt{\kappa}}, \tag{6.27}$$

which belong to a parameter regime that is thought to be ideal for the formation of magnetic bubbles [3]. A possible choice of the variational parameters in the initial ansatz (6.24) is accordingly given by $\rho_0 = 18\Delta_w$ and $\delta_0 = 1.1\Delta_w$ but it is certainly not unique. We finally mention that in all of the ensuing graphical illustrations of the fundamental bubble we invoke a slight departure from the rationalized physical units introduced in Section 2 and used throughout our theoretical development. Thus distances will now be measured in units of the ideal domain wall width $\Delta_w = 1/\sqrt{\kappa} = 1/\sqrt{2}$ in order to emphasize the wall structure of the calculated bubble. For instance, the film thickness will appear as $d = 16$.

We quote here the lattice constants used for the calculation of the bubble described in this section. In the z-direction the uniform lattice constant is $\Delta z = 0.57$ and corresponds to 14 lattice sites to this direction for the half film which is used in the numerical algorithm. We use 20 lattice sites in the ρ-direction to describe the bulk region of the bubble. Since the bubble radius is found to be approximately equal to the film thickness $d = 16$, we have used the value $\Delta\rho = 0.66$ for the lattice constant. At the domain wall we use a lattice spacing $\Delta\rho_w = 0.075$ in a series of 80 lattice sites. An other 40 lattice sites are used from there on with a spacing $\Delta\rho = 0.66$ to describe the region outside the bubble until the magnetization reaches its saturation value.

The value of the time step $\Delta\tau$ used, depends on the above mentioned values of the lattice spacing. We find that for the specific values used here, the algorithm is stable if the time step is chosen in the vicinity of $\Delta\tau = 5 \times 10^{-4}$.

B. The solution

The calculated fundamental magnetic bubble is illustrated in several ways. We mostly describe a $Q = 1$ bubble with positive polarity, originating in the initial ansatz (6.23) with the upper sign in m_ϕ, the results for negative polarity being inferred from

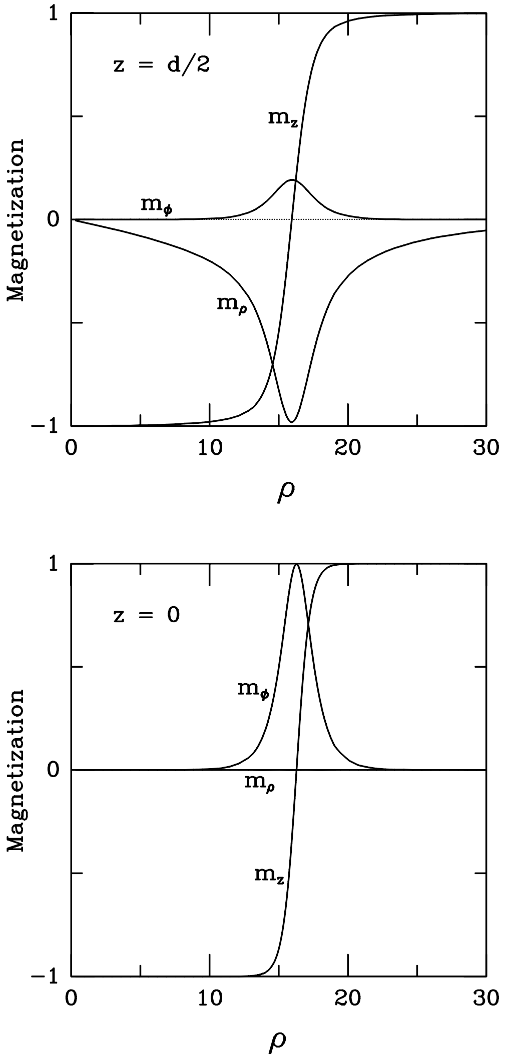

Fig. 4: The calculated magnetization for the fundamental (Q=1) magnetic bubble with positive polarity and parameters specified by Eq. (6.27). Results are given at the film center (z=0) and at the upper boundary $\left(z = d/2\right)$, whereas the corresponding results at the lower boundary $\left(z = -d/2\right)$ may be inferred from the parity relations (6.12). Here and in all subsequent graphical illustrations distance is measured in units of the ideal wall width $\Delta_w = 1/\sqrt{\kappa}$.

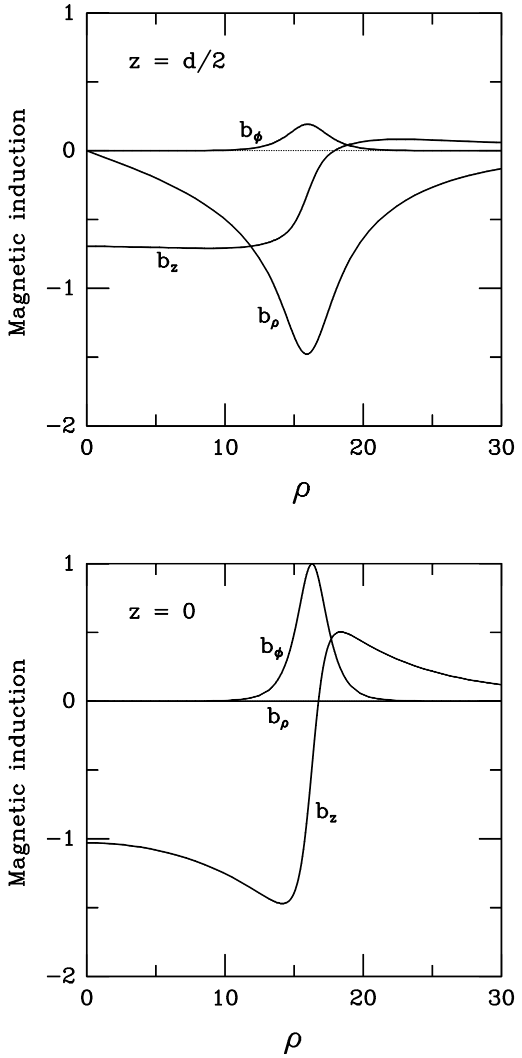

Fig. 5: The calculated magnetic induction for the Q=1 bubble; see caption of Fig. 4 for further explanations.

the discrete symmetry (6.11). Thus in Fig. 4 we display the dependence of the magnetization on the radial distance ρ at the film center ($z = 0$) and near the upper boundary ($z = d/2$); the ρ dependence near the lower boundary ($z = -d/2$) may be obtained from the parity relations (6.12). The corresponding results for the magnetic induction are shown in Fig. 5. One should keep in mind that the magnetostatic field extends beyond the film boundaries, but the calculated values will not be discussed

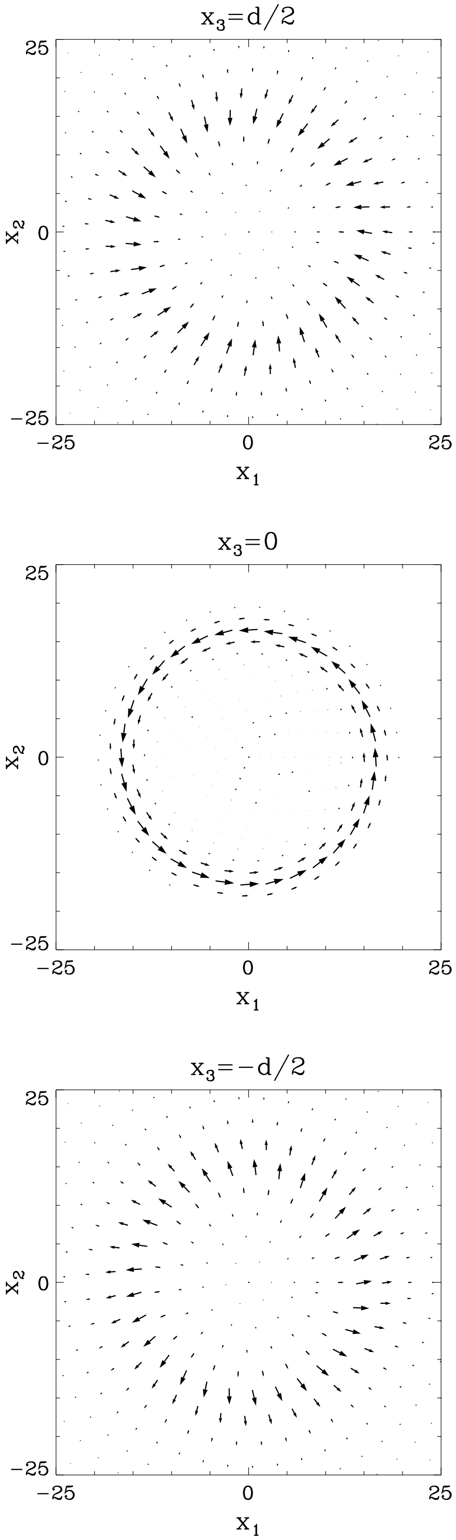

Fig. 6: Illustration of the Q=1 bubble with positive polarity through the projection of the magnetization vector field $\mathbf{m}$ on the (x_1, x_2) plane. The bubble is Bloch-like at the film center $(x_3=0)$ and Néel-like near the boundaries $(x_3 = \pm d/2)$.

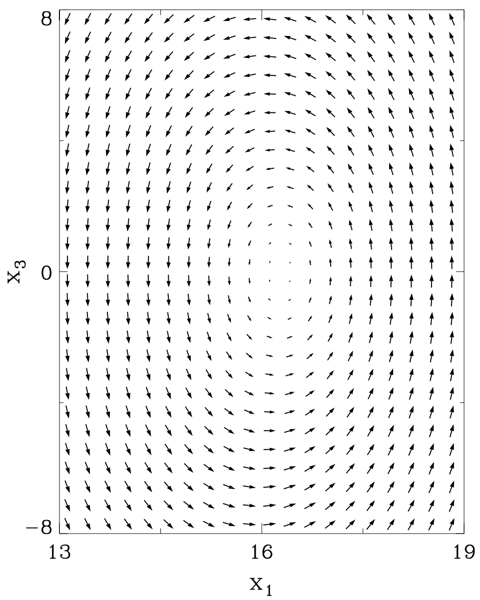

Fig. 7. Another view of the Q=1 bubble through the projection of $\mathbf{m}$ on the (x_1, x_3) plane.

further here.

Some important general features of the fundamental bubble are already apparent in Fig. 6. If we view the bubble as a curved domain wall, the wall is purely Bloch at the film center $(m_\rho = 0)$ and nearly Néel at the boundaries where the radial component m_ρ achieves significant values while the azimuthal component m_ϕ is small. A better view of the situation is obtained by plotting the projection of the magnetization vector $\mathbf{m}$ on the (x_1, x_2) plane in Fig. 6; whereas Fig. 7 illustrates the projection on a plane that contains the easy axis, which is chosen to be the (x_1, x_3) plane without loss of generality thanks to the axial symmetry.

The case of a $Q = 1$ bubble with negative polarity may be inferred from Eq. (6.11) applied, for example, to Fig.6.

The reflection $m_\phi \to -m_\phi$ will reverse the sense of circulation of the magnetization at the film center but will not significantly affect the picture at the boundaries where m_ϕ is small.

Having thus provided an overall view of the fundamental bubble, we now turn to the description of some important details. The simplest way to analyze the fine structure of the bubble is by recalling the concept of a vortex line introduced in Section 3. We first restate the condition of strict axial symmetry in terms of the spherical variables (2.33):

$$\Theta = \theta(\rho, z), \qquad \Phi = \phi + \chi(\rho, z), \tag{6.28}$$

where the functions θ and χ are independent of the angle ϕ and are related to the polar components of the magnetization by

$$\cos\theta = m_z, \qquad \chi = \arctan(m_\phi / m_\rho). \tag{6.29}$$

Therefore a vortex line is equivalently defined as the intersection of the two surfaces

$$m_z(\rho, z) = m_3, \qquad \phi + \chi(\rho, z) = \phi_0, \tag{6.30}$$

where m_3 and ϕ_0 are arbitrary constants in the intervals $[-1, 1]$ and $[0, 2\pi]$, respectively.

The first relation in (6.30) defines a curve in the (ρ, z) plane, illustrated in Fig. 8 for three typical values of m_3, and the surface obtained by a simple revolution of the curve around the third axis has the shape of a barrel. Of special interest is the case $m_3 = 0$ which may be used to define a (naive) radius of the bubble $\rho_0 = \rho_0(z)$ as the radius of the circular intersection of the barrel with the (x_1, x_2) plane at altitude z. We use the same symbol for the naive radius as for the variational parameter ρ_0 in Eq. (6.24) because the two coincide within the initial ansatz. The current definition of the radius is especially useful at the film boundaries where ρ_0 is the distance from the center of the bubble at which a sharp change in contrast takes place (see Fig. 6) that may be detected experimentally. In our numerical example we found that $\rho_0(z = \pm d/2) = 15.9\Delta_w$ which should be compared with the value at the film center $\rho_0(z = 0) = 16.3\Delta_w$, thus providing a measure of bubble bulging [3]. We also quote the average value of the naive radius

$$\bar{\rho}_0 = \frac{1}{d} \int_{-d/2}^{d/2} \rho_0(z) dz = 16.15\Delta_w \tag{6.31}$$

and compare it with the radius r defined by Eq. (4.29) and related to the total magnetic moment by Eq. (6.17):

$$r = 16.21\Delta_w. \qquad (6.32)$$

The radius r appears naturally within the theoretical development, as will become evident in the discussion of skew deflection in Section 7, whereas the naive radius ρ_0 is closer to what is actually measured in an experiment. Therefore the observed proximity of the numerical values quoted in Eqs. (6.31) and (6.32) is of special significance. Note incidentally that the calculated bubble radius for the specific parameters (6.27) is approximately equal to the film thickness.

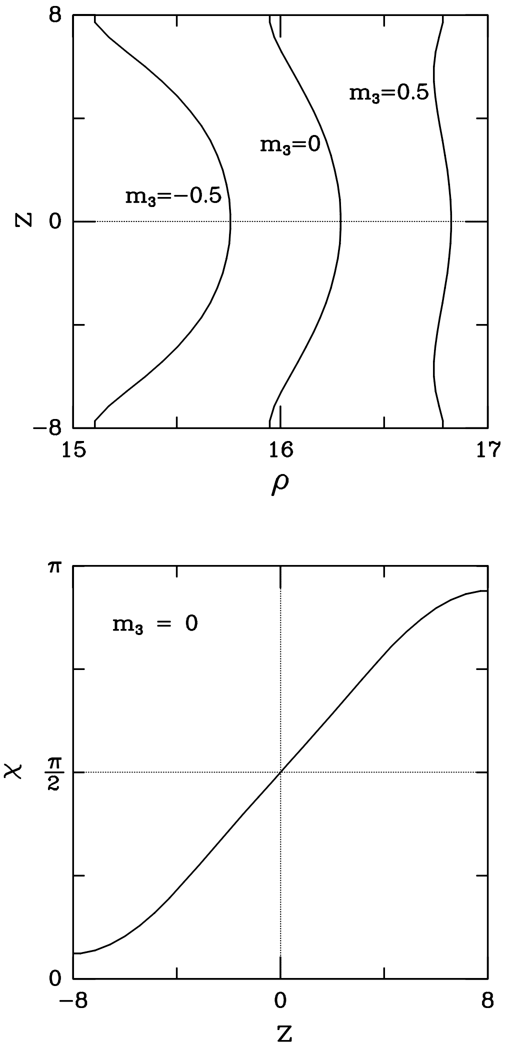

Fig. 8: The calculated curves $m_z(\rho, z) = m_3$ for $m_3=0, \pm 1/2$ (upper entry) and the z-dependence of χ along a vortex line (lower entry) for the Q=1 bubble with positive polarity; see the text for further explanations.

Next we consider the second relation in (6.30). We will not attempt to draw the corresponding surfaces, for various values of the constant ϕ_0, but examine directly their intersections (vortex lines) with a barrel at given m_3. Thus in Fig. 8 we also display the z-dependence of χ along a vortex line; that is, we plot the function $\chi(\rho(z; m_3), z) \equiv \chi(z; m_3)$ where $\rho(z; m_3)$ is the root of the algebraic equation $m_z(\rho, z) = m_3$ which depends on z and the particular value of m_3. At $m_3 = 0$, the root $\rho(z; m_3 = 0)$ reduces to the naive radius $\rho_0(z)$ discussed in the preceding paragraph. Actually Fig. 8 shows the z-dependence of χ along a vortex line only for $m_3 = 0$, but our numerical simulation furnished values for χ that are virtually indistinguishable when m_3 varies in the region $|m_3| < 1/2$. Nevertheless departures from such a universal behavior occur for $|m_3| > 1/2$.

The preceding findings are best summarized by the sketch of a typical vortex line

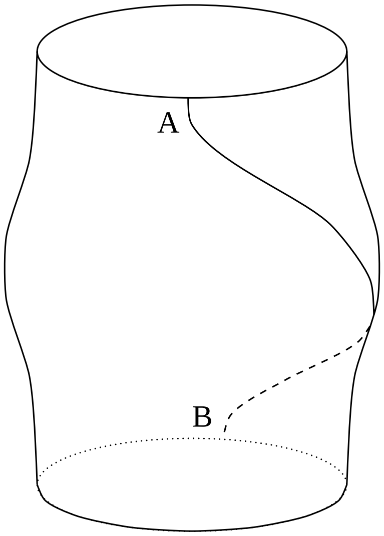

Fig. 9: Sketch of a typical vortex line for a Q=1 bubble with positive polarity. The sense of twist is reversed for a Q=1 bubble with negative polarity.

given in Fig. 9. Since the sum $\phi + \chi(\rho(z;m_3),z)$ must remain equal to a constant ϕ_0, a vortex line originating at a point A of the upper boundary, i.e., at given ϕ_0 and m_3, proceeds downward along the surface of the barrel at the same time twisting by an amount determined by the variation of χ illustrated in the lower part of Fig. 8. The vortex line eventually terminates at the lower boundary, at a point B, having suffered a total twist $\Delta\phi = -\Delta\chi = \chi(z = d/2; m_3) - \chi(z = -d/2; m_3)$ which generally depends on m_3. For the specific example $m_3 = 0$ shown in Fig. 8 the calculated total twist is $\Delta\phi = 158°$. This value remains practically the same in the range $|m_3| < 1/2$ but deviations do occur for $|m_3| > 1/2$. Finally we note that the vortex lines twist around the surface of a barrel counterclockwise for the $Q = 1$ bubble with positive polarity considered in our illustrations; the twist takes place clockwise for the $Q = 1$ bubble with negative polarity obtained through the discrete symmetry (6.11).

Returning to the topological classification discussed in Section 3, we note that all vortex lines in the fundamental magnetic bubble terminate at the film boundaries and do not tangle with each other. Hence a definition of a Hopf index is not possible, as expected for a film of finite thickness. On the other hand, the flux of vorticity through the plane (x_1, x_2) is equal to 4π for all z, thus leading to a unit winding number.

We also return to the virial relations derived in Section 5 and comment on the manner they are satisfied in our explicit calculation of the fundamental bubble. Because of the strict axial symmetry the surface integrals $S^{\pm}_{\mu\nu}$ of Eq. (5.10) reduce to

$$S^{\pm}_{\mu\nu} = S^{\pm}\delta_{\mu\nu}, \tag{6.33}$$

where $\delta_{\mu\nu}$ is the 2D Kronecker delta and

$$S^{\pm} = \frac{1}{2} \underset{x_3 = \pm d/2}{\int_0^\infty} \rho h_\rho b_z 2\pi\rho d\rho. \tag{6.34}$$

Hence relations (5.9) applied for $\mu \neq \nu$ simplify to

$$\int \sigma_{12} dV = 0 = \int \sigma_{21} dV, \tag{6.35}$$

which are valid in each region I, II or III separately. In fact, using the explicit expression of the stress tensor for an axially symmetric configuration, Eqs. (6.35) reduce to the single equation

$$\int h_\rho m_\phi dV = 0, \tag{6.36}$$

which is automatically satisfied thanks to the parity relations (6.12). Furthermore Eqs. (5.9) applied for $\mu = \nu = 1$ or 2 yield for the various regions

$$\begin{aligned} \int_{\mathrm{I}} \sigma_{11} dV &= \int_{\mathrm{I}} \sigma_{22} dV = S^+ - S^-, \\ \int_{\mathrm{II}} \sigma_{11} dV &= \int_{\mathrm{II}} \sigma_{22} dV = -S^+, \\ \int_{\mathrm{III}} \sigma_{11} dV &= \int_{\mathrm{III}} \sigma_{22} dV = S^-, \end{aligned} \tag{6.37}$$

as well as

$$\int \sigma_{11} dV = 0 = \int \sigma_{22} dV, \tag{6.38}$$

when the integration extends over all volume. The above relations were verified explicitly in our numerical simulation and were thus used to test its validity. We further verified the Derrick-like relation (5.20) in our specific numerical example where $W_e = 4134$, $W_a = 6008$, $W_b = 11952$, $W_m - W_m^{(0)} = -22573$, and $sd = -9713$; here energy is measured in the rationalized units introduced in Section 2.

7. Skew deflection

We are thus ready to study the main dynamical question posed in the Introduction. A static bubble with winding number Q initially located at, say, the origin of the coordinate system is subjected to an external magnetic field

$$\mathbf{h}_{\text{ext}} = (0, 0, h_{\text{ext}}), \qquad h_{\text{ext}} = h_{\text{ext}}(\mathbf{x}, t), \tag{7.1}$$

that points along the easy axis and its strength is some prescribed function of position and time. Our task is to determine the response of the bubble to such an external probe. In the absence of dissipation ($\lambda = 0$) the relevant dynamical equation is Eq. (2.15) extended according to

$$\mathbf{f} \to \mathbf{f} + \mathbf{h}_{\text{ext}}, \tag{7.2}$$

in order to include the effect of the applied field (7.1) which is turned on at $t = 0$. One must then solve the resulting equation with an initial condition provided by the static bubble and calculate the magnetization $\mathbf{m} = \mathbf{m}(\mathbf{x}, t)$ at all later times.

However a great deal can be learned without actually solving this initial-value problem thanks to the special nature of the conservation laws derived in Section 4. Since the position of the guiding center $\mathbf{R} = (R_1, R_2)$ is conserved in the absence of dissipation and external fields other than a uniform bias field, examining the rate at which $\mathbf{R}$ changes in the presence of the field (7.1) should yield direct information on the response of the bubble. Hence the vorticity $\boldsymbol{\gamma}$ now obeys the relation

$$\dot{\gamma}_i = \varepsilon_{ijk}[\partial_j \partial_\ell \sigma_{k\ell} - \partial_j(\mathbf{h}_{\text{ext}} \cdot \partial_k \mathbf{m})], \tag{7.3}$$

which is Eq. (3.11) or (3.15) extended according to Eq. (7.2). In particular, the evolution of the third component of the vorticity is governed by

$$\dot{\gamma}_3 = \varepsilon_{\nu\lambda}[\partial_\nu \partial_\ell \sigma_{\lambda\ell} - \partial_\nu(\mathbf{h}_{\text{ext}} \cdot \partial_\lambda \mathbf{m})], \tag{7.4}$$

where we have returned to the 2D notation for Greek indices, as in Section 4, except for the Latin index ℓ that is summed over all three values. The evolution of the moments I_μ of Eq. (4.1) is then given by

$$\dot{I}_\mu = \int \varepsilon_{\nu\lambda} x_\mu [\partial_\nu \partial_\ell \sigma_{\lambda\ell} - \partial_\nu(\mathbf{h}_{\text{ext}} \cdot \partial_\lambda \mathbf{m})] dV, \tag{7.5}$$

where the contribution of the first term may be shown to vanish by reasoning completely analogous to that used in the derivation of the conservation laws in Section 4. Implicit in the above statement is the assumption that the applied field (7.1) does not affect significantly the configuration of the bubble at large distances or, equivalently, it does not affect the ground state of the ferromagnet. We shall return to this assumption later in this section. Thus the evolution of the moments in the presence of the applied field is governed by

$$\dot{I}_\mu = -\int \varepsilon_{\nu\lambda} x_\mu \partial_\nu (h_{\text{ext}} \partial_\lambda m_3) dV = \int \varepsilon_{\mu\nu} h_{\text{ext}} \partial_\nu m_3 dV, \tag{7.6}$$

where we have taken into account that the field (7.1) points in the third direction and have also performed an elementary partial integration. On the assumption that $m_3 \to 1$ sufficiently fast at spatial infinity, one may perform a further partial integration to write

$$\dot{I}_\mu = -\int (\varepsilon_{\mu\nu}\partial_\nu h_{\text{ext}})(m_3 - 1)dV. \tag{7.7}$$

Also recall that the winding number is conserved even in the presence of the applied field provided that the latter does not destroy the ground state of the ferromagnet. Therefore the drift velocity of the bubble may be inferred from Eqs. (4.28) and (7.7):

$$V_\mu \equiv \dot{R}_\mu = -\frac{1}{4\pi dQ}\int (\varepsilon_{\mu\nu}\partial_\nu h_{\text{ext}})(m_3 - 1)dV. \tag{7.8}$$

This result for the drift velocity is not completely explicit because the third component of the magnetization appearing under the integral sign must still be determined through a detailed solution of the initial-value problem described in the introductory paragraphs of this section. However Eq. (7.8) already contains the essential information concerning the experimentally observed skew deflection of magnetic bubbles, for it suggests that the drift velocity will acquire a significant component mainly in a direction perpendicular to the gradient of the applied field.

In order to appreciate the physical content of Eq. (7.8) the applied field is written as

$$h_{\text{ext}} = g x_1, \qquad g = g(\mathbf{x}, t), \tag{7.9}$$

where the "gradient" g may still be a function of position and time. The two components of the drift velocity (7.8) are given equivalently by

$$V_1 = -\frac{1}{4\pi dQ}\int (x_1\partial_2 g)(m_3 - 1)dV, \qquad V_2 = \frac{1}{4\pi dQ}\int (g + x_1\partial_1 g)(m_3 - 1)dV. \tag{7.10}$$

The field is now restricted to the physically interesting situation where the gradient is nearly spatially uniform, i.e. $g \approx g(t)$, over a large region surrounding the bubble and drops to zero outside that region. Under such conditions all implicit assumptions made in deriving Eqs. (7.10) are satisfied. In particular, all partial integrations performed on the assumption that the field does not significantly alter the behavior of the bubble at large distances are justified. Nevertheless it is clear from Eqs. (7.10) that an especially transparent result would be obtained in the ideal limit where the gradient g is spatially uniform everywhere. Then

$$g = g(t); \qquad V_1 = 0, \qquad V_2 = \frac{\mu g}{4\pi dQ}, \tag{7.11}$$

where μ is the total magnetic moment defined in Eq. (4.2).

A completely uniform gradient would imply an infinite field at $x_1 \to -\infty$ opposing the magnetization in its ground state $\mathbf{m} = (0, 0, 1)$. Therefore, in the presence of some dissipation, the magnetization would align with the applied field almost immediately after the field is turned on and assume the value $\mathbf{m} = (0, 0, -1)$ far in the left plane. Such an instance would destroy the original topological structure of the bubble and obscure the question of skew deflection. Nevertheless the preceding criticism does not apply in the case of vanishing dissipation considered so far because the magnetization would then precess wildly around the easy axis far in the left plane but never align with the external field. Hence the uniform limit considered in Eq. (7.11) is mathematically meaningful in the absence of dissipation and provides the clearest, albeit idealized, illustration of the main theme discussed in this chapter.

Thus the guiding center of a bubble with $Q \neq 0$ moves in a direction perpendicular to the applied gradient, in analogy with the familiar Hall motion of an electric charge in a uniform magnetic field (the analog of the winding number) and a uniform electric field (the analog of the uniform magnetic-field gradient). Furthermore the drift velocity (7.11) is expressed in terms of quantities with a simple physical meaning. However this expression for the drift velocity is not completely explicit because the total moment is not conserved during the application of the gradient and thus acquires some time dependence $\mu = \mu(t)$ that can be determined only through a detailed solution of the initial-value problem. The moment μ would be conserved if the magnetostatic field were absent. Indeed the orbital angular momentum ℓ and the total magnetic moment μ would then be separately conserved in the absence of the applied field and, while the latter violates conservation of ℓ because it breaks rotational symmetry, it does not affect μ because it points in the third direction. Under such conditions Eq. (7.11) provides an explicit expression for the drift velocity since the conserved moment μ could then be calculated from the initial configuration of the (static) bubble. This situation occurs in the case of the 2D isotropic Heisenberg model where an analytical result for the drift velocity was given in Ref. [5] and was later verified by a numerical simulation in Ref. [10]. Detailed numerical simulations on this model will be presented in the next chapter.

Returning to the realistic case where the magnetostatic field is not negligible, we note that the total moment μ may still be calculated from the profile of the static bubble during the initial stages of the process. If we further restrict our attention to the fundamental bubble calculated in Section 6, the moment is related to the bubble radius through Eq. (6.17) and the initial drift velocity may be written as

$$Q = 1; \qquad V_1 = 0, \qquad V_2 = -\frac{1}{2} g r^2, \tag{7.12}$$

where we may substitute the numerical value for the bubble radius given in Eq. (6.32) which is approximately equal to the naive radius measured in an experiment. Now applying Eq. (7.12) for the speed $V = |V_2|$ yields

$$\frac{g r^2}{2V} = 1, \tag{7.13}$$

which is golden rule (1.1) with a deflection angle $\delta = 90^\circ$, as is appropriate in the absence of dissipation, and a winding number $Q = 1$.

However one should keep in mind that the above result provides only a partial verification of the golden rule for two reasons. First, Eq. (7.13) is in general violated during the late stages of the process because neither μ nor r are conserved; in particular, the relation $\mu = -2\pi d r^2$ is strictly valid only for a static bubble. Second, one must examine the extent to which (1.1) is valid in the presence of dissipation when the deflection angle is no longer equal to 90°. The last statement follows from the simple physical fact that dissipation induces a tendency for alignment of the magnetization with the external field, which drives the bubble also toward the left half plane where the field points along the negative third direction.

A. Initial drift velocity

In this subsection we shall calculate the initial drift velocity of the bubble when dissipation is present, based only on the conservation laws. In order to study the effect of dissipation more precisely we return to Eq. (2.37) and extend it according to Eq. (7.2) to write

$$\dot{\mathbf{m}} + (\mathbf{m} \times \mathbf{G}) = 0, \qquad \mathbf{m}^2 = 1, \tag{7.14}$$

where the effective field $\mathbf{G}$ is given by

$$\begin{gathered} \mathbf{G} = \lambda_1(\mathbf{f} + \mathbf{h}_{\text{ext}}) + \lambda_2[\mathbf{m} \times (\mathbf{f} + \mathbf{h}_{\text{ext}})], \\ \lambda_1 = \frac{1}{1+\lambda^2}, \qquad \lambda_2 = \frac{\lambda}{1+\lambda^2}. \end{gathered} \tag{7.15}$$

Since Eq. (7.14) is formally identical to the dissipationless equation, with the replacement $\mathbf{f} \to \mathbf{G}$, the time derivative of the vorticity may be inferred from Eq. (3.11) with the same replacement:

$$\dot{\gamma}_i = -\varepsilon_{ijk} \partial_j (\mathbf{G} \cdot \partial_k \mathbf{m}). \tag{7.16}$$

Substitution of the field $\mathbf{G}$ from Eq. (7.15) leads to

$$\dot{\gamma}_i = \varepsilon_{ijk}\partial_j\{\lambda_1\partial_\ell\sigma_{k\ell} - \lambda_1(\mathbf{h}_{\rm ext}\cdot\partial_k\mathbf{m}) - \lambda_2[\mathbf{m}\times(\mathbf{f}+\mathbf{h}_{\rm ext})]\cdot\partial_k\mathbf{m}\}, \tag{7.17}$$

a result that may be used to study the time evolution of the guiding center in a manner analogous to our earlier discussion in the absence of dissipation. The drift velocity is now given by

$$V_\mu = \frac{\varepsilon_{\mu\nu}}{4\pi dQ}\int[\lambda_1\mathbf{h}_{\rm ext} + \lambda_2[\mathbf{m}\times(\mathbf{f}+\mathbf{h}_{\rm ext})]\cdot\partial_\nu\mathbf{m}dV, \tag{7.18}$$

which reduces to Eq. (7.8) at vanishing dissipation.

The above result is highly implicit in that the magnetization in the right-hand side must still be determined through a detailed solution of the initial value problem. However some explicit information can be extracted from Eq. (7.18) for the early stages of the bubble motion. The magnetization may then be calculated from the static profile of the bubble for which $\mathbf{m}\times\mathbf{f} = 0$. Therefore the initial drift velocity is given by

$$V_\mu = \frac{\varepsilon_{\mu\nu}}{4\pi dQ}\int[\lambda_1\mathbf{h}_{\rm ext} + \lambda_2(\mathbf{m}\times\mathbf{h}_{\rm ext})]\cdot\partial_\nu\mathbf{m}dV, \tag{7.19}$$

where it is understood that the magnetization is that of a static bubble with winding number Q. Taking into account that the field points in the third direction and performing a partial integration in the first term yields the equivalent relation

$$V_\mu = -\frac{\varepsilon_{\mu\nu}}{4\pi dQ}\int[\lambda_1(\partial_\nu h_{\rm ext})(m_3-1) + \lambda_2 h_{\rm ext}(m_1\partial_\nu m_2 - m_2\partial_\nu m_1)]dV. \tag{7.20}$$

At this point, one should recall the assumptions on the gradient $g = g(\mathbf{x},t)$ discussed following Eq. (7.9) which are especially important in the presence of dissipation. Specifically the gradient must vanish outside a large region surrounding the bubble, for otherwise both the ground state and the topological structure of the bubble would be significantly altered. Yet the specific choice of the gradient at large distances will certainly affect the long-time behavior of the bubble but should not be crucial during the early motion. Therefore it is still meaningful to approximate the *initial* drift velocity by inserting in Eq. (7.20) the applied field $h_{\rm ext} = gx_1$ with a gradient $g = g(t)$ that is spatially uniform. If we further restrict Eq. (7.20) to the fundamental magnetic bubble calculated in Section 6 we find that

$$Q = 1; \qquad V_1 = -\lambda_2\frac{g\nu}{4\pi d}, \qquad V_2 = \lambda_1\frac{g(\mu+\lambda c)}{4\pi d}, \tag{7.21}$$

where λ is the dissipation constant, d is the film thickness, and the constants μ, ν and c are given by

$$\mu = \int (m_z - 1) dV, \qquad \nu = \frac{1}{2} \int (m_\rho^2 + m_\phi^2) dV,$$
$$c = \frac{1}{2} \int \rho \left(m_\rho \frac{\partial m_\phi}{\partial \rho} - \frac{\partial m_\rho}{\partial \rho} m_\phi \right) dV. \tag{7.22}$$

Here μ is the total moment, ν is essentially the anisotropy energy, and c vanishes on account of the parity relations (6.12). Therefore our final result for the initial drift velocity in the presence of dissipation is

$$V_1 = -\lambda_2 \frac{g\nu}{4\pi d}, \qquad V_2 = \lambda_1 \frac{g\mu}{4\pi d}. \tag{7.23}$$

Since the total moment μ is always negative and the constant ν positive, the guiding center moves off in the lower left plane with an initial deflection angle δ with respect to the negative x_1 axis given by

$$\tan \delta = \frac{V_2}{V_1} = \frac{1}{\eta \lambda} \quad \text{or} \quad \sin \delta = \frac{1}{\sqrt{1 + \eta^2 \lambda^2}}, \tag{7.24}$$

where the coefficient

$$\eta = -\frac{\nu}{\mu} = 0.08 \tag{7.25}$$

is calculated from Eqs. (7.22) using as input the static bubble. The specific numerical value quoted above corresponds to the specific choice of parameters made in Section 6. Finally we calculate the speed

$$V = \sqrt{V_1^2 + V_2^2} = \frac{\sqrt{1 + \eta^2 \lambda^2}}{1 + \lambda^2} \frac{g|\mu|}{4\pi d} \tag{7.26}$$

and relate it to the bubble radius through Eq. (6.17) and the deflection angle through Eq. (7.24):

$$\frac{gr^2}{2V} \sin \delta = \frac{1 + \lambda^2}{1 + \eta^2 \lambda^2}. \tag{7.27}$$

At vanishing dissipation ($\lambda = 0$) the deflection angle (7.24) becomes $\delta = 90°$ and relation (7.27) reduces to (7.13).

Relation (7.27) establishes contact with the semi-empirical golden rule (1.1) in the important special case of the fundamental magnetic bubble. For small values of the dissipation constant λ encountered in practice [1] the right-hand side of Eq. (7.27) is well approximated by unity, to within terms of order λ^2, and is thus consistent with

Eq. (1.1) applied for $Q = 1$. However this is again only a partial verification of the golden rule because Eq. (7.27) is strictly valid only for the initial drift velocity.

B. Steady state approximation

A complete verification would require first to ascertain that the bubble eventually reaches a steady state, namely a state with constant velocity and radius. Such a question could be addressed by a direct numerical solution of the initial-value problem posed in the first paragraph of this section. This numerical task is in several respects similar to the solution of the fully dissipative equation (6.1) described in Section 6, except for a technical difference that might prove crucial in practice. Because the applied field breaks rotational invariance the bubble looses its strict axial symmetry during skew deflection and thus leads to a 3D numerical simulation.

We shall not search for such a solution here but assume that a steady state is eventually reached when dissipation as well as a field gradient are present. We shall also not examine here conditions on the form of the external field that would guarantee the development of a steady state. In particular, it is not known whether or not a simple, almost uniform gradient, would actually lead to a steady state. In fact Thiele [4] seems to suggest that the field gradient may have to exhibit a carefully selected time dependence. Nevertheless, the assumption of a steady state for a moving bubble will lead to a certain prediction for its velocity as we shall see.

Let the magnetization be of the form $\mathbf{m} = \mathbf{m}(\mathbf{x} - \mathbf{v}t; \mathbf{v})$. We write the Landau-Lifshitz equation including dissipation and an external field in a form analogous to (2.12):

$$\dot{\mathbf{m}} + \mathbf{m} \times (\mathbf{f} + \mathbf{h}_{ext}) = \lambda\,(\mathbf{m} \times \dot{\mathbf{m}}). \tag{7.28}$$

Inserting the special form of $\mathbf{m}$ in this equation we find

$$\mathbf{m} \times (\mathbf{f} + \mathbf{h}_{ext}) = V_\nu(\partial_\nu \mathbf{m} - \lambda \mathbf{m} \times \partial_\nu \mathbf{m}) \tag{7.29}$$

where V_ν is the ν-th component of the bubble velocity. We take the cross product of both sides with $\partial_\mu \mathbf{m}$ and then take the inner product with $\mathbf{m}$. Integrating the resulting equation over all space we find

$$4\pi d Q \varepsilon_{\mu\nu} V_\nu + \lambda b_{\mu\nu} V_\nu - C_\mu = 0 \qquad \mu = 1 \text{ or } 2, \tag{7.30}$$

where

$$C_\mu \equiv -\int (h_{ext} \partial_\mu m_3)\, dV \tag{7.31}$$

and

$$b_{\mu\nu} \equiv \int (\partial_\mu \mathbf{m} \cdot \partial_\nu \mathbf{m}) dV = \int (\partial_\mu \Theta \partial_\nu \Theta + sin^2 \Theta \partial_\mu \Phi \partial_\nu \Phi) dV \tag{7.32}$$

is called the dissipation tensor [4]. Applying relation (7.30) for $\mu = 1$ and 2 yields a system of equations for the components of the velocity V_1 and V_2.

The algebraic manipulation of this system would be easy only if the dissipation tensor $b_{\mu\nu}$ would not depend on the velocity. But, since the profile of a moving bubble depends in general on the velocity, we have $b_{\mu\nu} = b_{\mu\nu}(\mathbf{v})$. Thus we invoke the approximation of weak external field. In fact Eq. (7.30) implies that the bubble velocity is small for weak fields. In this case we may approximate $b_{\mu\nu}$ by its value for a static bubble profile. Eqs. (7.30) become then a system of linear equations for V_1, V_2.

A simpler form for C_μ is obtained by applying a partial integration:

$$C_\mu = \int (\partial_\mu h_{ext})(m_z - 1) dV \tag{7.33}$$

and if we restrict the external field to the ideal form of a pure gradient $h_{ext} = g x_1$, we find

$$C_1 = g\mu, \qquad C_2 = 0, \tag{7.34}$$

where μ is given in Eq. (7.22). The system (7.30) is now solved to yield

$$V_1 = \frac{\lambda b_{22}}{\lambda^2 \mathrm{det} b + (4\pi d Q)^2} g\mu, \qquad V_2 = \frac{4\pi d Q - \lambda b_{12}}{\lambda^2 \mathrm{det} b + (4\pi d Q)^2} g\mu. \tag{7.35}$$

The criticism concerning the uniform gradient form of the external field, presented in connection with Eq. (7.11) applies here. Thus, it is not legitimate to use this form of $\mathbf{h}_{ext}$ in the present problem. Nevertheless, Eq. (7.35) can be considered to give the limiting result for the case of an external field which develops a uniform gradient over a large region surrounding the bubble and drops to zero outside this region. The form of a steady state magnetization considered here guarantees that the original topological structure of the bubble will not be destroyed by the external field even if we take the limiting case of a uniform gradient.

A simpler version of relations (7.35) is obtained by using some further informations about the initial profile of the bubble. Thus we assume that the bubble is axial symmetric (for instance, it is the fundamental bubble), i.e. it is described in its rest frame by spherical variables of the form $\Theta = \Theta(\rho)$ and $\Phi = \text{const.} \times \phi$, where ρ and ϕ are the usual polar variables defined from $x_1 = \rho\cos\phi$ and $x_2 = \rho\sin\phi$. Then the elements of the dissipation tensor (7.32) reduce to

$$\begin{aligned} b_{12} &= 0 = b_{21}, \\ b_{11} &= b_{22} = \frac{1}{2}(b_{11} + b_{22}) = W_e, \end{aligned} \tag{7.36}$$

where W_e is the exchange energy of the bubble and Eq. (7.35) becomes

$$V_1 = \frac{\lambda W_e}{\lambda^2 W_e^2 + (4\pi d Q)^2} g\mu, \qquad V_2 = \frac{4\pi d Q}{\lambda^2 W_e^2 + (4\pi d Q)^2} g\mu. \tag{7.37}$$

The speed of the bubble is then given by

$$V = (V_1^2 + V_2^2)^{1/2} = \frac{|g\mu|}{[\lambda^2 W_e^2 + (4\pi d Q)^2]^{1/2}}. \tag{7.38}$$

Since μ is negative we have that $V_1, V_2 < 0$ (if $g > 0$). Thus the bubble moves to the lower left plane. The deflection angle δ measured from the negative x-axis is given by

$$\sin\delta = \frac{-V_2}{V} = -\frac{4\pi d Q V}{g\mu}. \tag{7.39}$$

Relation (7.39) may also be written as

$$Q = -\frac{g\mu}{4\pi d V} \sin\delta. \tag{7.40}$$

In this relation we may further substitute the total magnetization $\mu = -2\pi d r^2$ obtained in Eq. (6.17) for the fundamental bubble, but is reasonable to hold for any bubble, and obtain the golden rule of bubble dynamics

$$Q = \frac{g r^2}{2V} \sin\delta. \tag{7.41}$$

In conclusion we note that the two approaches of this section, concerning the skew deflection of the bubble, lead to only a partial verification of the golden rule. In particular, we note that the question of the steady state motion of the bubble remains open.

Nevertheless the question was addressed and answered within a strictly 2D Skyrme model [11] which also leads to Eqs. (7.24) and (7.27) for the initial drift velocity. However it was found through an explicit numerical solution of the initial-value problem that a sharp transient period exists during which the deflection angle departs rapidly and significantly from Eq. (7.24). The transient period is followed by an intermediate regime where the deflection angle reaches a more or less constant value and the golden rule is verified in a rough manner. But a true steady state is never achieved and the finer predictions of the golden rule are not sustained. In particular, the long-time behavior of the bubble is sensitive to the details of the gradient at large distances.

We have performed numerical simulations for the 2D isotropic Heisenberg model along the lines of this section and the results will be presented in the next chapter. The steady state for a moving bubble is never achieved in this model for reasonable choices of the gradient. On the other hand the result obtained through the initial velocity approximation is found to remain valid for an intermediate period of time.

The results from the 2D Skyrme model [11] as well as from the 2D isotropic Heisenberg model could be used as a guide for future numerical investigations of the realistic quasi-2D model studied in the present chapter. We thus turn to a summary of our main conclusions given in the following section.

8. Concluding remarks

We believe to have provided a clear illustration of an important link that exists between the topological complexity of ferromagnetic structures and their dynamics. The most direct manifestation of such a link is the construction of unambiguous conservation laws as moments of the topological vorticity. The special dynamical features of magnetic bubbles become transparent and are formally related to more familiar situations such as the Hall effect of electrodynamics or the Magnus effect of fluid dynamics.

Our work has also revealed that some of the quantitative predictions of the early studies must be interpreted with caution. In particular, the golden rule is valid in its gross features but not in its details. Hence there exists room for further development of the dynamical theory of magnetic bubbles. Numerical simulations along the lines of those performed within the strictly 2D Skyrme model [11] could prove feasible and provide important hints concerning the remaining questions. There has also been some speculation to the effect that the dynamics might simplify for hard ($|Q| \gg 1$) bubbles, in analogy with the adiabatic dynamics of electric charges in strong magnetic fields [10]. The semi-empirical golden rule might then prove to be exact in the extreme large-Q limit and could possibly be corrected through a systematic adiabatic perturbation theory at finite Q.

In this chapter we have confined our attention to the response of a bubble to an externally applied magnetic-field gradient. However a field gradient is intrinsically present also in the problem of two or more interacting magnetic bubbles. Thus two interacting bubbles with winding numbers of the same sign are expected to orbit around each other, in analogy with the 2D motion of two electrons in a uniform magnetic field or two vortices in an ordinary fluid. Similarly two bubbles with opposite winding numbers (e.g., $Q = 1$ and $Q = -1$) should move in formation along roughly parallel lines, also in analogy with an electron-positron pair in a uniform magnetic field or a vortex-antivortex pair in a fluid. These expectations were confirmed through numerical simulations in the Skyrme model [11] and should be possible to establish both theoretically and experimentally in real ferromagnetic films. Analogous results are expected for interacting Abrikosov vortices in a superconductor [6].

CHAPTER II
THE ISOTROPIC HEISENBERG MODEL

1. Introduction

The results of Chapter I motivate the study of a much simpler model where both the analytical and the numerical work can be pushed further. In particular, we shall study the skew deflection of bubbles in the two-dimensional isotropic Heisenberg model. We use the rationalized form of the Landau-Lifshitz equation (I.2.15) and omit all terms except for the exchange in the effective field **f**:

$$\dot{\mathbf{m}} = \mathbf{m} \times \mathbf{f}, \qquad \mathbf{f} = \Delta \mathbf{m}, \qquad \mathbf{m}^2 = 1. \tag{1.1}$$

The magnetization is supposed to be a function of two spatial variables and the time, $\mathbf{m} = \mathbf{m}(x_1, x_2, t)$, and Δ denotes the Laplacian in two dimensions. The energy functional for model (1.1) is accordingly given by the exchange energy of Eq. (I.2.19) restricted to two dimensions.

In searching for nontrivial static solutions of Eq. (1.1) it will be useful to rewrite this equation by explicitly resolving the constraint on the vector variable **m**. We use the stereographic variable Ω defined from

$$\Omega = \frac{m_1 + i\, m_2}{1 + m_3}, \tag{1.2}$$

where m_i denotes the i-th component of **m**. The magnetization components are expressed through Ω by inverting relation (1.2):

$$m_1 = \frac{\Omega + \overline{\Omega}}{1 + \Omega\overline{\Omega}}, \qquad m_2 = \frac{1}{i}\,\frac{\Omega - \overline{\Omega}}{1 + \Omega\overline{\Omega}}, \qquad m_3 = \frac{1 - \Omega\overline{\Omega}}{1 + \Omega\overline{\Omega}}, \tag{1.3}$$

where $\overline{\Omega}$ denotes the complex conjugate of Ω. We also use the complex position variables $z = x_1 + i\,x_2$, $\bar{z} = x_1 - i\,x_2$ to write Eq. (1.1) as

$$\frac{i}{4}\,\dot{\Omega} = \Omega_{z\bar{z}} - \frac{2\,\overline{\Omega}}{1+\Omega\overline{\Omega}}\,\Omega_z\Omega_{\bar{z}}. \tag{1.4}$$

Static solutions satisfy the above equation with the time derivative absent:

$$\Omega_{z\bar{z}} - \frac{2\,\overline{\Omega}}{1+\Omega\overline{\Omega}}\,\Omega_z\Omega_{\bar{z}} = 0. \tag{1.5}$$

It is obvious that any function Ω of the complex variable z or $\bar{z}$ alone satisfies the above equation. Finite energy solutions are obtained with the choice $\Omega = \pi_1(z)/\pi_2(z)$ or $\Omega = \pi_1(\bar{z})/\pi_2(\bar{z})$, where π_1, π_2 are arbitrary polynomials. These are the well-known Belavin-Polyakov instantons [28], viewed here as static solutions in a 2+1-dimensional Heisenberg model.

In this Chapter we shall often use for illustration, as well as for numerical simulations, the special class of solutions

$$\Omega = \left(\frac{\bar{a}}{\bar{z}}\right)^n \qquad \text{and} \qquad \Omega = \left(\frac{a}{z}\right)^n, \tag{1.6}$$

where a is an arbitrary complex constant reflecting the scale invariance of the model (1.5). These solutions are such that $\Omega \to 0$ $(m_3 \to 1)$ at spatial infinity, that is, the boundary condition (I.3.4) is satisfied. On the other hand we have $\Omega \to \infty$ $(m_3 = -1)$ at the origin so that $z = 0$ may be considered the center of the bubble. Finally at $z = a$ we have $\Omega = 1$, or $m_3 = 0$, and hence $|a|$ can be taken as a naive definition of the bubble radius. The bubble solutions (1.6) can be written in terms of the magnetization vector components as

$$\begin{aligned} m_1 &= \frac{2a^n\rho^n}{\rho^{2n}+a^{2n}}\,\cos(n\phi), \\ m_2 &= \frac{2a^n\rho^n}{\rho^{2n}+a^{2n}}\,\sin(n\phi), \\ m_3 &= \frac{\rho^{2n}-a^{2n}}{\rho^{2n}+a^{2n}} \end{aligned} \qquad \text{and} \qquad \begin{aligned} m_1 &= \frac{2a^n\rho^n}{\rho^{2n}+a^{2n}}\,\cos(n\phi), \\ m_2 &= -\frac{2a^n\rho^n}{\rho^{2n}+a^{2n}}\,\sin(n\phi), \\ m_3 &= \frac{\rho^{2n}-a^{2n}}{\rho^{2n}+a^{2n}}, \end{aligned} \tag{1.7}$$

where ρ, ϕ are the polar coordinates.

The bubbles in a 2D model are characterized by an integer-valued winding number or topological charge Q, defined in analogy to the quantity (I.3.10):

$$Q = \frac{1}{4\pi}\int \gamma\, d^2x. \tag{1.8}$$

In this equation, γ is a topological vorticity defined as a 2D restriction of (I.3.1):

$$\gamma = -\frac{1}{2}\varepsilon_{\mu\nu}(\partial_\mu \mathbf{m} \times \partial_\nu \mathbf{m}) \cdot \mathbf{m}, \qquad \mu, \nu = 1, 2. \tag{1.9}$$

We find that the configurations (1.6) carry a winding number $Q = n$ and $-n$, respectively.

2. Conservation laws

We shall use the vorticity to construct the conservation laws and study the dynamics of bubbles in this model [5]. The conserved linear momentum is given by

$$p_\mu = \varepsilon_{\mu\nu} I_\nu, \qquad I_\nu = \int x_\nu \, \gamma \, d^2x \tag{2.1}$$

and guiding center coordinates can be defined by

$$R_\mu = \frac{\int x_\mu \, \gamma \, d^2x}{\int \gamma \, d^2x} = \frac{I_\mu}{4\pi Q}, \qquad \mu = 1 \text{ or } 2, \tag{2.2}$$

where Q and I_μ are given in Eqs. (1.8) and (2.1).

Similarly, the orbital angular momentum is expressed in terms of the vorticity through

$$\ell = \frac{1}{2}\int \rho^2 \gamma \, d^2x, \tag{2.3}$$

where $\rho^2 = x_1^2 + x_2^2$, while the total magnetization to the third direction is

$$\mu = \int (m_3 - 1) \, d^2x. \tag{2.4}$$

We mention here that ℓ and μ are conserved separately in the present isotropic Heisenberg model because the magnetostatic interaction is absent and hence the model is invariant in separate rotations of coordinates or spin vectors. The *mean squared radius* of the bubble is defined in terms of the angular momentum ℓ by

$$r^2 = \frac{\ell}{2\pi Q} - \mathbf{R}^2, \tag{2.5}$$

with ℓ and $\mathbf{R} = (R_1, R_2)$ given in Eqs. (2.3) and (2.2) respectively. Note that the radius r is a conserved quantity in this model.

An explicit calculation of the above quantities can be performed taking as an example the bubble solutions (1.6). The guiding center coordinates calculated from Eq. (2.2) vanish ($\mathbf{R} = 0$), which means that the bubble is set at the origin. More interestingly, the angular momentum (2.3) is

$$\ell = 2\pi Q \, \frac{(\pi/Q)}{\sin(\pi/Q)} \, |a|^2, \tag{2.6}$$

where $Q = \pm n$ is the topological charge of the bubbles. The mean squared radius defined in Eq. (2.5) is

$$r^2 = \frac{(\pi/Q)}{\sin(\pi/Q)} \, |a|^2. \tag{2.7}$$

For unit topological charge ($n = \pm 1$) the radius is divergent, reflecting the slow decay of the fundamental BP instanton. This property is certainly not shared by more realistic magnetic bubbles such as the fundamental bubble calculated in section I.6. In the opposite limit, $n \to \infty$, the bubble radius coincides with the naive definition $r = |a|$.

The total magnetization can also be calculated for the examples (1.6). Using Eq. (2.4) we find

$$\mu = -2\pi \, \frac{(\pi/Q)}{\sin(\pi/Q)} \, |a|^2, \tag{2.8}$$

which naturally is a negative quantity ($\mu < 0$). Eqs. (2.7), (2.8) imply the simple relation

$$\mu = -2\pi r^2, \tag{2.9}$$

which is a formula with a simple geometrical meaning. If we imagine a crude model for the bubble in which m_3 takes the value -1 for radial distances smaller than the bubble radius r and the value $+1$ otherwise, then $m_3 - 1$ takes the values -2 and 0 respectively, and the total magnetization is indeed given by Eq. (2.9).

3. Skew deflection

A bubble initially at rest is now subjected to a uniform magnetic field $\mathbf{h}_{ext}$ which is accounted for by the simple replacement $\Delta\mathbf{m} \to \Delta\mathbf{m} + \mathbf{h}_{ext}$ in Eq. (1.1). If the field is pointing in the third direction i.e. it is of the form (I.7.1) the evolution of the guiding center coordinates is given by a formula analogous to (I.7.8):

$$V_\mu \equiv \dot{R}_\mu = -\frac{1}{4\pi Q} \int (\varepsilon_{\mu\nu} \partial_\nu h_{ext})(m_3 - 1) \, d^2x. \tag{3.1}$$

A uniform gradient of the form $h_{ext} = gx_1$, where $g = g(t)$, gives the simple result

$$V_1 = 0, \qquad V_2 = \frac{\mu g}{4\pi Q}, \qquad Q = \pm n. \tag{3.2}$$

In the current model, the total magnetization μ, defined in Eq. (2.4), is a conserved quantity even in the presence of an external field since this is pointing in the third direction. This is because such a field does not break the rotational invariance of the model around the third axis. Thus we may substitute in Eq. (3.2) the initial value for the total magnetization given in Eqs. (2.8) and (2.9) to get a completely explicit result valid for all times.

$$V_1 = 0, \qquad V_2 = -\frac{gr^2}{2Q}, \tag{3.3}$$

which is consistent with the golden rule (I.1.1) applied for $V = |V_2|$ and $\delta = \pm 90^o$ as is appropriate in the absence of dissipation. Numerical simulations presented later in this Chapter, confirm the above predictions and also shed light on the extent to which the bubble follows the motion of its guiding center.

In the presence of dissipation conservation laws alone do not suffice to determine the drift velocity at all times. Nevertheless the *initial drift velocity* is given by the 2D restriction of (I.7.20):

$$V_\mu = -\frac{\varepsilon_{\mu\nu}}{4\pi Q} \int [\lambda_1(\partial_\nu h_{ext})(m_3 - 1) + \lambda_2 h_{ext}(m_1\partial_\nu m_2 - m_2\partial_\nu m_1)] d^2x. \tag{3.4}$$

The discussion following Eq. (I.7.20) concerning the form of the gradient applies here without change. Keeping those precautions in mind, we use the simple uniform gradient field $h_{ext} = gx_1$ with $g > 0$ and also insert the static solutions of Eq. (1.6) in Eq. (3.4) to calculate the *initial drift velocity*:

$$V_1 = -\lambda_2 \frac{g\nu}{4\pi}, \qquad V_2 = \lambda_1 \frac{g\mu}{4\pi Q}, \qquad Q = \pm n, \tag{3.5}$$

where μ is the initial total magnetization given in Eq. (2.8), while the constant ν is defined from

$$\nu = \frac{1}{2} \int (m_1^2 + m_2^2) d^2x. \tag{3.6}$$

It is understood that m_1, m_2 are the initial values of the magnetization vector given in Eq. (1.7). Some algebra shows that

$$\nu = -\frac{\mu}{|Q|}. \tag{3.7}$$

We note that such a simple result depends crucially on the specific form of the bubble solutions (1.6) and is thus special to the current isotropic Heisenberg model. The drift velocity is then given by

$$V_1 = \lambda_2 \frac{g\mu}{4\pi|Q|}, \qquad V_2 = \lambda_1 \frac{g\mu}{4\pi Q}, \qquad Q = \pm n. \tag{3.8}$$

The speed of the bubble is

$$V = \sqrt{V_1^2 + V_2^2} = \sqrt{\lambda_1} \frac{g|\mu|}{4\pi|Q|}. \tag{3.9}$$

Substituting μ from Eq. (2.9) we obtain

$$V = \sqrt{\lambda_1} \frac{gr^2}{2|Q|}. \tag{3.10}$$

The deflection angle measured from the negative x_1 axis is accordingly given by

$$\sin\delta = -\frac{V_2}{V} = \frac{|Q|}{Q}\sqrt{\lambda_1}. \tag{3.11}$$

We now insert Eq. (3.11) in Eq. (3.10) to recover the golden rule

$$\frac{gr^2}{2V}\sin\delta = Q. \tag{3.12}$$

Thus, within the present model, we have derived the exact form of the golden rule (compare (3.12) to (I.1.1)) while in section I.7 only an approximate expression for the golden rule has been found as Eq. (I.7.27). But we note here that the derivation of Eq. (3.12) depends crucially on the analytical accident given in Eq. (3.7).

The discussion of this section actually establishes only a first contact with the golden rule for the isotropic Heisenberg model. In particular Eqs. (3.8) and (3.12) are valid only at the initial steps of the bubble motion. A complete investigation of the golden rule in the presence of dissipation would require (a) to examine the extent to which Eq. (3.12) remains valid during the late stages of the motion and (b) to determine whether or not the bubble moves coherently together with its guiding center. These issues have been addressed by a direct numerical solution of the initial value problem. But first we discuss a rather simple model of noninteracting spins which will serve as guide for a precise understanding of the numerical results.

4. The free spin model

The evolution of the guiding center coordinates in the absence of dissipation is given in Eq. (3.2) where we note that the velocity of the bubble is proportional to the strength of the external field gradient, whereas no trace of the exchange interaction strength is found. In close relation to this remark, approximation (3.4) is based on the assumption that the exchange interaction only sets the initial configuration as a static solution of this model and does not play any other role at the beginning of the process. The bubble is, at this initial stage, driven by the field h_{ext}. The numerical results of Refs. [10] suggest that the simple results obtained by this approximation describe the bubble motion fairly well, under certain conditions, for times longer than expected.

These remarks prompt us to examine in more detail the model of noninteracting spins which we shall call the free spin model. This will certainly be an oversimplified model but some general results that will be obtained will prove useful for comparison with the corresponding numerical and analytical results for the Heisenberg model.

The most suitable formalism for the present section is achieved through the stereographic variable. The equation of motion for Ω in an external field $\mathbf{h}_{ext} = (0, 0, h_{ext})$ is

$$\frac{i+\lambda}{4}\,\dot{\Omega} + \frac{h_{ext}}{4}\,\Omega = \Omega_{z\bar{z}} - \frac{2\overline{\Omega}}{1+\Omega\overline{\Omega}}\,\Omega_z\Omega_{\bar{z}} \tag{4.1}$$

with λ being the dissipation constant. We omit all terms but the external field in the right hand side of this equation to obtain the free spin model:

$$(i+\lambda)\,\dot{\Omega} + h_{ext}\,\Omega = 0. \tag{4.2}$$

The field h will be taken to be a function of the position variables only, for simplicity: $h_{ext} = h_{ext}(x_1, x_2)$. The above is a linear equation and its general solution is

$$\Omega(\mathbf{x}, t) = e^{-(\lambda_2 - i\lambda_1) h_{ext} t}\,\Omega_0, \tag{4.3}$$

where λ_1, λ_2 are defined in Eq. (I.2.37) and Ω_0 is the configuration at $t = 0$.

Within the present analysis, the candidates for the initial configuration Ω_0 are the static solutions of the exchange model and we shall use here for definiteness

$$\Omega_0 = \frac{a^n}{\bar{z}^n} \qquad a : \text{real constant}. \tag{4.4}$$

This choice for Ω_0 makes the time dependent solution (4.3) completely explicit and allows for the calculation of its general characteristics, such as the vorticity and the guiding center coordinates.

The vorticity can be calculated for the solution (4.3) by use of Eq. (1.9). Actually γ can be written in terms of the variable Ω as

$$\gamma = \frac{4(|\Omega_{\bar{z}}|^2 - |\Omega_z|^2)}{(1+\Omega\overline{\Omega})^2}. \tag{4.5}$$

Using this formula, we find

$$\gamma = \frac{4n}{\rho^2} \frac{a^{2n}\, \rho^{2n}\, e^{2\lambda_2 h_{ext} t}}{(a^{2n} + \rho^{2n}\, e^{2\lambda_2 h_{ext} t})^2} \left[n + [\lambda_2\, \rho\, (\partial_\rho h_{ext}) + \lambda_1 (\partial_\phi h_{ext})]\, t \right], \tag{4.6}$$

where ρ, ϕ are the polar variables and $\partial_\rho, \partial_\phi$ denote differentiation with respect to the corresponding variable. Integration of γ over all space should give the winding number result $Q = n$ multiplied by 4π. Before performing this integration, some assumptions have to be made for the form of the field h_{ext}. Based on the discussion and results of the two preceding sections, we shall suppose that h_{ext} develops a gradient in a certain direction. In particular, throughout this section we shall assume h_{ext} to be an odd function in the x_1 variable and even in x_2. Such a choice for h_{ext} includes the uniform gradient form and it also allows for more realistic fields. Then, the third term in Eq. (4.6) is odd in x_2 and give zero on integration, while the rest give the winding number as

$$Q = \frac{1}{4\pi} \int \gamma\, d^2x = 2n \int_0^\infty \frac{a^{2n}\, \rho^{2n-1}\, e^{2\lambda_2 h_{ext} t}}{(a^{2n} + \rho^{2n}\, e^{2\lambda_2 h_{ext} t})^2} \left[n + \lambda_2\, \rho\, (\partial_\rho h_{ext}) t \right]\, d\rho. \tag{4.7}$$

The integrand of the above equation can be written as a total derivative in ρ so that we obtain

$$Q = -n \int_0^\infty \frac{d}{d\rho} \left[\frac{a^{2n}}{a^{2n} + \rho^{2n}\, e^{2\lambda_2 h_{ext} t}} \right] d\rho = n. \tag{4.8}$$

The integration in the last relation can be carried out only if we make the assumption that $h_{ext}(x_1, x_2)$ is finite at spatial infinity. This condition is important in the above and in the subsequent calculations. A uniform gradient field does not satisfy such a condition, as we have already discussed in the previous section.

A rederivation of result (3.2) within the context of the present free spin model should be possible since, as we have mentioned in the beginning of this section, it does not depend on any parameters related to the exchange interaction. We shall give this derivation here for the configuration (4.4). We first write the vorticity (4.6) for $\lambda = 0$ $(\lambda_1 = 1, \lambda_2 = 0)$ and for a field h_{ext} taken to be the uniform gradient used in section 3 (with g a constant). The result is

$$\gamma = -\frac{4n}{\rho^2} \frac{a^{2n}\, \rho^{2n}}{(a^{2n} + \rho^{2n})^2} \left(n + g\, x_2\, t \right). \tag{4.9}$$

The moment of this vorticity $I_1 = \int x_1 \gamma \, d^2x$ is easily seen to vanish since the integrand is odd. The moment I_2 is

$$I_2 = -\int \frac{4n}{\rho^2} \, \frac{a^{2n}\, \rho^{2n}}{(a^{2n}+\rho^{2n})^2} \, \left(n\, x_2 + g\, x_2^2\, t \right) \, d^2x. \tag{4.10}$$

The first term in this integral is odd in x_2 and vanishes on integration. The second term can be written, using polar coordinates ρ, ϕ, as

$$I_2 = -g\, t\, 2\pi \int_0^\infty \frac{2n\, a^{2n}\, \rho^{2n}}{(a^{2n}+\rho^{2n})^2} \, \rho \, d\rho, \tag{4.11}$$

where we have performed a trivial integration in ϕ. The integrand can be written as a sum of two terms by use of the relation

$$\frac{2n\, a^{2n}\, \rho^{2n+1}}{(a^{2n}+\rho^{2n})^2} = \frac{2\, a^{2n}\, \rho}{a^{2n}+\rho^{2n}} - \frac{d}{d\rho} \left[\frac{a^{2n}\, \rho^2}{a^{2n}+\rho^{2n}} \right]. \tag{4.12}$$

The second term on the right hand side of Eq. (4.12) gives zero on integration, since it is a total derivative vanishing at the edges of the integration interval (for $n > 1$) while the first term, integrated in ρ, is related to the conserved total spin μ quoted in Eq. (2.4). Thus we finally have

$$I_2 = -g\, t\, 2\pi \int_0^\infty \frac{2\, a^{2n} \rho \, d\rho}{a^{2n}+\rho^{2n}} = g\, \mu\, t. \tag{4.13}$$

Putting together the results of this paragraph we have for the evolution of the guiding center of the bubble

$$V_1 \equiv \dot{R}_1 = 0, \qquad\qquad V_2 \equiv \dot{R}_2 = \frac{\mu g}{4\pi n}, \tag{4.14}$$

thus reaching to the same result as in Eq. (3.2).

The presence of dissipation will significantly change the situation. We first note that the uniform gradient field cannot be used in the present analysis. So in what follows we suppose that the field h_{ext} is finite at spatial infinity. We suppose in this section that h_{ext} is odd in the x_1 variable and even in x_2, but the analytic calculation of the guiding center coordinates as a function of time is not feasible for such an arbitrary field in the presence of dissipation. Guided by the results of the previous section and in particular by Eq. (3.8), we shall attempt to calculate the following quantity:

$$R_1 - \lambda\, R_2 = \frac{1}{4\pi n} \int (x_1 \gamma - \lambda\, x_2 \gamma) \, d^2x. \tag{4.15}$$

We substitute γ from Eq. (4.6) in the above equation. Some terms under the integral appear to be odd in x_2 giving zero on integration. The remaining terms are written as

$$\begin{aligned} R_1 - \lambda R_2 &= \frac{1}{\pi} \int \frac{a^{2n}\, \rho^{2n-2}\, e^{2\lambda_2 h_{ext} t}}{(a^{2n} + \rho^{2n} e^{2\lambda_2 h_{ext} t})^2} \left[n\, x_1 + \lambda_2 \left(\partial_1 h_{ext} \right) \rho^2\, t \right]\, d^2 x = \\ &= \frac{1}{2\pi} \int \frac{d}{dx_1} \left[\frac{a^{2n}}{a^{2n} + \rho^{2n} e^{2\lambda_2 h_{ext} t}} \right]\, dx_1 dx_2 = 0 \end{aligned} \tag{4.16}$$

where, in the last integration, we have a total derivative integrated from minus to plus infinity, whence the vanishing result. The symbol ∂_1 in the above relation denotes differentiation with respect to x_1.

Eq. (4.16) determines the orbit of the bubble as a straight line with inclination angle δ with respect to the x_1 axis, with $\tan\delta = R_2/R_1 = 1/\lambda$. This result is consistent with the result (3.8) obtained within the exchange model. It is valid for the initial stages of the bubble motion within the exchange model and it is strictly correct for all times in the present free spin model. The question arises to what extent does the presence of the exchange interaction changes it at later stages of the bubble motion.

A more important question is whether the guiding center faithfully describes the position of the bubble. In the case of the free spin model the bubble is not expected to move coherently since the vector $\mathbf{m}$ only precesses around the field $\mathbf{h}_{ext}$. Solution (4.3) helps us confirm this picture. We see, for instance, that at every time t, we have $|\Omega| \to \infty$ at the origin. This means that the point where $m_3 = -1$, which can be thought of as the center of the bubble, stays still during the evolution of the configuration. This is certainly enough to exclude a coherent bubble motion.

On the other hand, the presence of the exchange interaction is expected to help the bubble move in a more organized way thus following its guiding center. These questions may be answered by numerical simulations which will show the domain of validity of Eq. (4.16) within the Heisenberg model as well as the details of the bubble motion.

5. Numerical integration

In this section we shall describe a numerical integration in time of the exchange model in the presence of an external field gradient. The results obtained within the free spin model in the preceding section will serve as a guide to the present numerical simulations and will also help us in the interpretation of the dynamics of the exchange model. In some respects we shall follow Ref. [10].

When no dissipation is present, the numerical solution should reproduce the exact result (3.2) for the evolution of the guiding center coordinates, which was also found as Eq. (4.14) within the free spin model. In the presence of dissipation, we expect that the guiding center of the bubble will follow the simple result (3.8), but deviations from it are expected to be observed soon. The details of the bubble motion will also be an important product of the numerical simulations, since the description of the bubble position through the guiding center coordinates relies upon the assumption of a coherent motion of the bubble.

The numerical calculations will use a discrete version of the equations of motion. We use second order difference to approximate the Laplacian on a 2D lattice. We also use an external field of the form

$$h_{ext} = g\, x_1\, e^{-(\rho/b)^m} \qquad \rho = \sqrt{x_1^2 + x_2^2}, \quad g, b, m : \text{constants}, \tag{5.1}$$

throughout our numerical calculations. This form fulfills all the requirements imposed in our theoretical development, namely it develops a nearly uniform gradient around the origin and it vanishes at infinity.

The time evolution algorithm requires an initial configuration which will be taken to be a static solution of the exchange model. In particular we shall use the one given in Eq. (4.4). We make the choice $a = 1$ which sets the scale for the present problem and also take $n = 2$ which sets the topological charge to $Q = 2$. With these choices, the configuration is written in terms of the magnetization vector $\mathbf{m}$ as

$$m_1 = \frac{2\rho^2}{\rho^4 + 1} \cos 2\phi, \qquad m_2 = \frac{2\rho^2}{\rho^4 + 1} \sin 2\phi, \qquad m_3 = \frac{\rho^4 - 1}{\rho^4 + 1}. \tag{5.2}$$

To obtain a discrete version of this configuration, we must set the lattice spacing. Since the naive bubble radius a is equal to unity we choose

$$\delta = 0.05 \tag{5.3}$$

so that the naive bubble radius is equal to 20 lattice sites. We then expect that variations of the spin variable are slow so that we are close to the continuum limit.

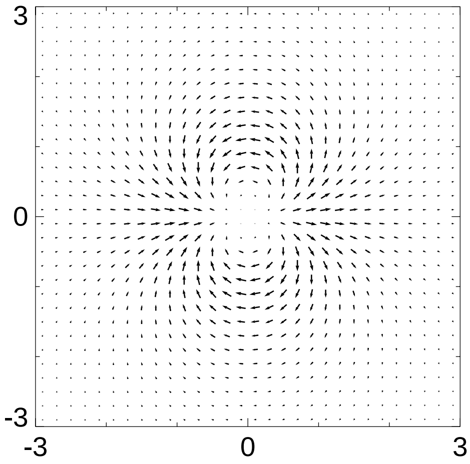

Fig. 10a: A 2D plot of the spin vector $\mathbf{m}$ for the bubble (5.2). $\mathbf{m}$ is represented by its projection in the (12) plane.

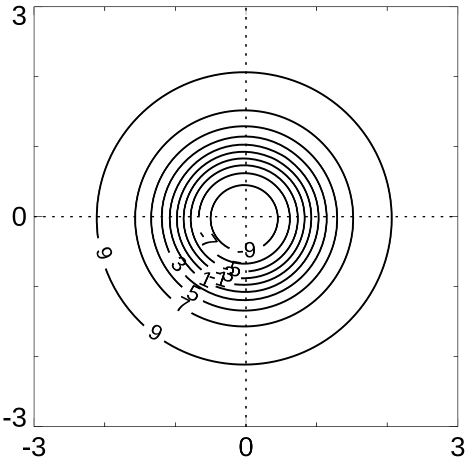

Fig. 10b: A contour plot of the third component of the spin, multiplied by a factor of ten ($10\ m_3$), for the bubble (5.2).

In fact, this discretization proves more than adequate to describe configuration (5.2) but it is only enough to describe the bubble evolution in time so that departures from the continuum limit do not occur too soon.

We fit configuration (5.2) in a 240×240 lattice, with the center of the bubble, i.e. the point where $S_3 = -1$, placed at the origin. A 2D plot of it is given in Fig. 10a. Only a small part (central part) of the lattice is drawn and the spin is drawn every fifth lattice site. Fig. 10b presents a contour plot of the third component of the spin vector for (5.2). Actually, we have plotted the quantity $10 S_3$, so that the number 10 in the contours corresponds to the spin pointing to the north pole, while -10 corresponds to the spin pointing to the south pole. To conclude the discussion on the initial configuration, we note that, despite that the $Q = 1$ bubble might seem simpler for the simulations, we shall avoid it for two related reasons. First, it has infinite total magnetization μ, as we have already mentioned in Section 2, a fact that would obscure the simplicity of our results. Second, because of the low decay of its spin field which would require a very large lattice to be described.

For the field h_{ext} in Eq. (5.1) we choose $b = 4$, so that a nearly uniform field gradient develops in a large area surrounding the bubble, while we take $m = 4$ so that the field quickly falls to zero away from the bubble. The strength of the gradient is taken $g = 1$. So the field used in our simulations is

$$h_{ext} = x_1 \, e^{-(\rho/4)^4}, \qquad \rho = \sqrt{x_1^2 + x_2^2}. \tag{5.4}$$

The integration in time is performed by a fourth order Runge-Kutta method, with a time step chosen at the vicinity of $\delta\tau = 5 \times 10^{-4}$. This proves enough to produce a stable algorithm, but we note that when the exchange interaction is omitted, i.e. when the free spin model is simulated, the time step can be chosen two orders of magnitude larger. The constraint of constant magnitude for the magnetization ($\mathbf{m}^2 = 1$), is implemented by reinforcing it in every step of the time integration algorithm [27]. This, considerably improves the stability of the algorithm. We finally note that because of the accumulating numerical errors and the gradual complication of the evolving configuration, the accuracy of the calculated quantities is getting poorer as the simulation time passes.

Simulations for vanishing dissipation have been performed first. We simulate both the free spin model and the full exchange model with external field. The evolution of the moments of the vorticity follow quite accurately Eq. (3.2) (or (4.14)) for both cases, while the details of the evolving configuration differ significantly in the two cases. We shall not give further details for these simulations but we believe that all the essential features of the bubble's time evolution emerge also when dissipation is present.

Thus, we shall give here the details for the simulation of the dissipative algorithm. We use a dissipation constant λ =0.25 and we run the program until the time τ =3. This time interval proves enough for the essential characteristics of the bubble motion to be revealed. We believe that the calculated results are accurate to a few percent. For instance, the topological charge is calculated numerically as 1.991 at $\tau = 0$ and 1.957 at $\tau = 3$, instead of the exact value $Q = 2$.

The evolution of the guiding center coordinates is given in Fig. 11a. Formula (2.2) has been used for the calculation of R_1, R_2, while the discrete derivatives, needed for the calculation of the vorticity, have been calculated with the central differences prescription of Ref. [10]. The solid lines show the results obtained from the exchange model and the dashed lines show the corresponding results from a free spin model simulation. Fig. 11b show the corresponding bubble velocity calculated as the numerical derivative of $\mathbf{R}$. Our first remark on these figures is that the free spin model calculations for R_μ follow the simple result (4.16) to within numerical accuracy, that is the ratio R_1/R_2 is constant throughout the motion and equal to 0.25. On the other hand the values of $V_\mu = \dot{R}_\mu$ at $\tau = 0$, read form Fig 11b, are very close to the values calculated by use of (3.4), with m_1, m_2, m_3 taken from Eq. (5.2). The values found from Eq. (3.4) are $\dot{R}_1(\tau = 0) = -0.086$, $\dot{R}_2(\tau = 0) = -0.345$ while the numerically calculated values are $\dot{R}_1(\tau = 0) = -0.081$, $\dot{R}_2(\tau = 0) = -0.321$.

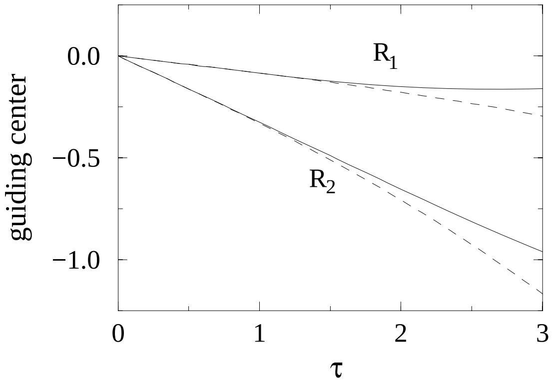

Fig. 11a: Evolution of the guiding center coordinates of the bubble (5.2), with a dissipation constant λ =0.25 and under the influence of an external field (5.4). The dashed lines correspond to the free spin model simulations and the solid lines to the exchange model with external field.

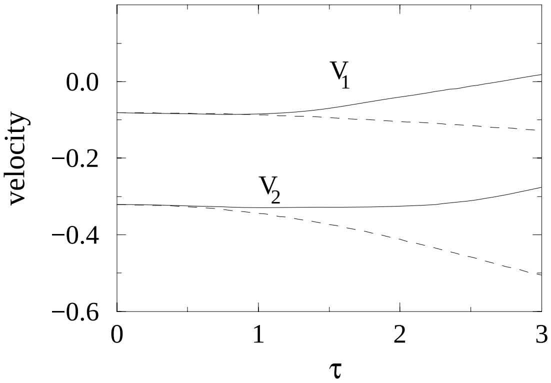

Fig. 11b: The drift velocity of the bubble $V_\mu = \dot{R}_\mu$, calculated as the numerical derivative of the guiding center presented in Fig. 11a. The dashed lines correspond to the free spin model simulations and the solid lines to the exchange model with external field.

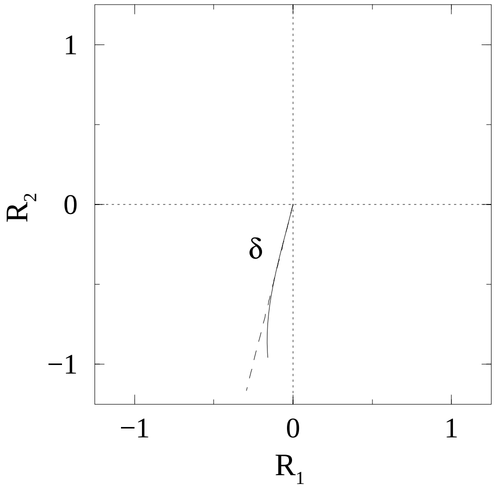

Fig. 11c: The orbit of the bubble (5.2), i.e. a plot of R_1 versus R_2, using the numerical data of Fig. 11a. The dashed lines correspond to the free spin model simulations and the solid lines to the full exchange model with external field.

The unexpected result read off from Fig. 11a or 11b is that deviations of the guiding center or velocity for the exchange model, from the simple results obtained within the free spin model, occur only at late times. An other way to see this is to plot the orbit of the bubble, that is a diagram of R_1 versus R_2. This is given in Fig. 11c and it shows that the bubble evolving in the exchange model (solid line) follows the straight line orbit derived within the free spin model (dashed line) for significantly long times and deviates from it, after it has traveled a distance approximately equal to its radius.

In order to give a semi-theoretical explanation for these numerical results, we have organized an expansion in time for the expressions of the guiding center coordinates R_1 and R_2. These expressions are written in terms of the vorticity quoted in Eq. (4.6) with the field h_{ext} that of Eq. (5.1). When the exchange interaction and the field h_{ext} are included in the equations of motion, very involved algebraic calculations have to be performed in order to find terms in the expansion for R_1, R_2 higher than the second order in time. So, we are obliged to resort to symbolic calculation computer

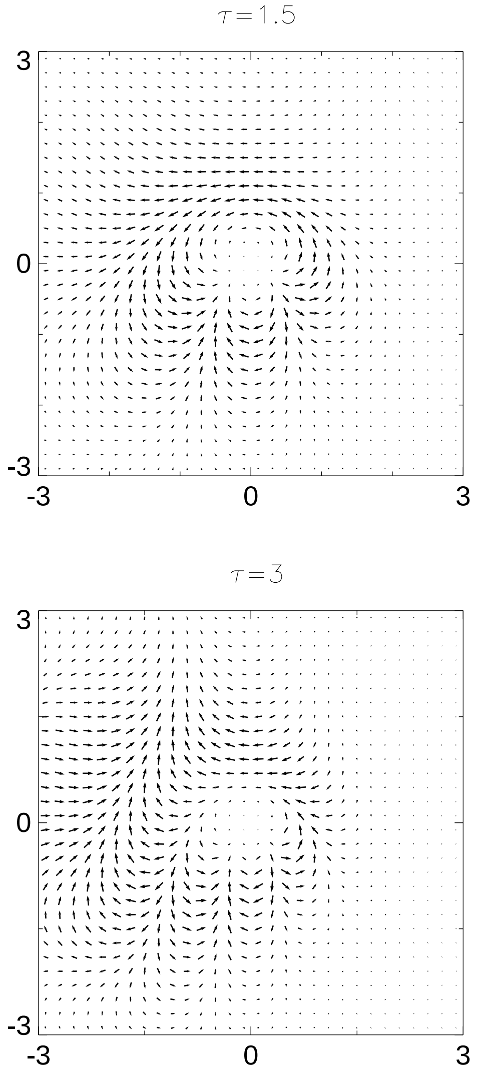

Fig. 12a: Vector plot of the magnetization **m** represented through its projection on the (12) plane. The bubble (5.2) is evolved within the free spin model. We use field (5.4) and a dissipation constant λ =0.25. We give two snapshots, at times τ =1.5 and τ =3.

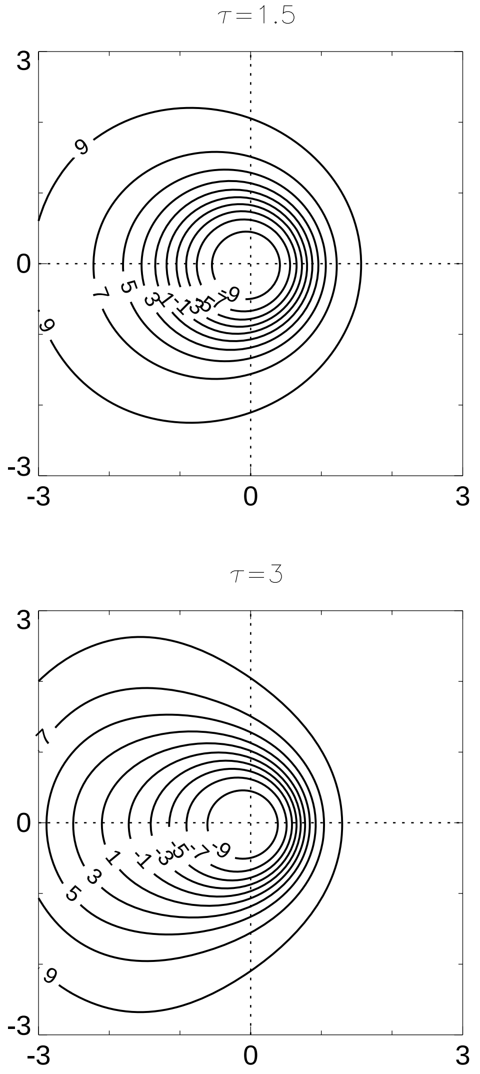

Fig. 12b: Contour plot of the third component of the magnetization multiplied by ten: $10m_3$. The bubble (5.2) is evolved within the free spin model. We use field (5.4) and a dissipation constant λ =0.25. We give two snapshots, at times τ =1.5 and τ =3.

programs. We have used for this purpose "MATHEMATICA" and have found no trace of the exchange interaction in the first three terms of the two time expansions. In the fourth term, the exchange interaction is involved in both expansions only when dissipation is present, so that the difference from the corresponding free spin calculation is $O(t^4)$ in both R_1 and R_2. Correspondingly, the difference in the components of the drift velocity $V_\mu = \dot{R}_\mu$ is $O(t^3)$.

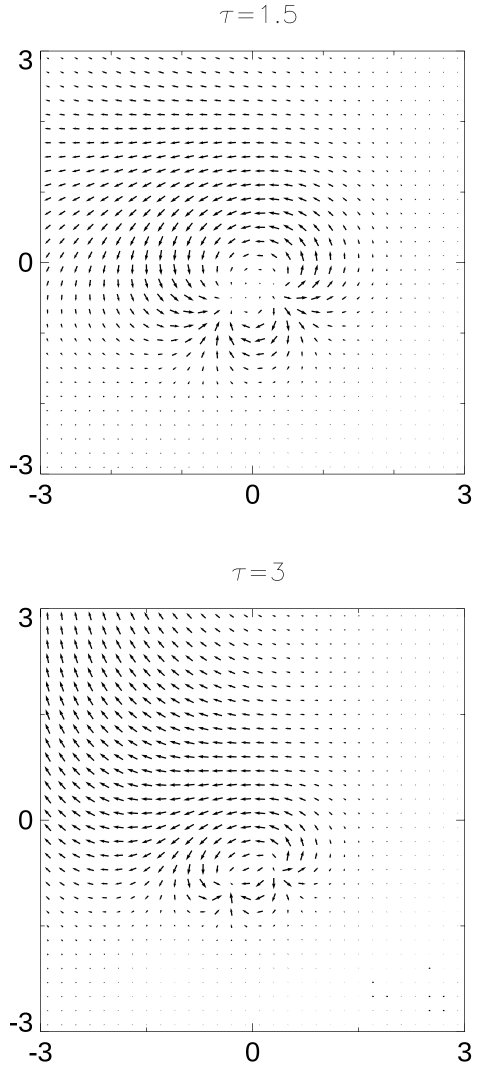

Fig. 13a: Vector plot of the magnetization $\mathbf{m}$ represented through its projection on the (12) plane. The bubble (5.2) is evolved within the exchange model with the external field (5.4). We use a dissipation constant λ =0.25. We give two snapshots, at times τ =1.5 and τ =3.

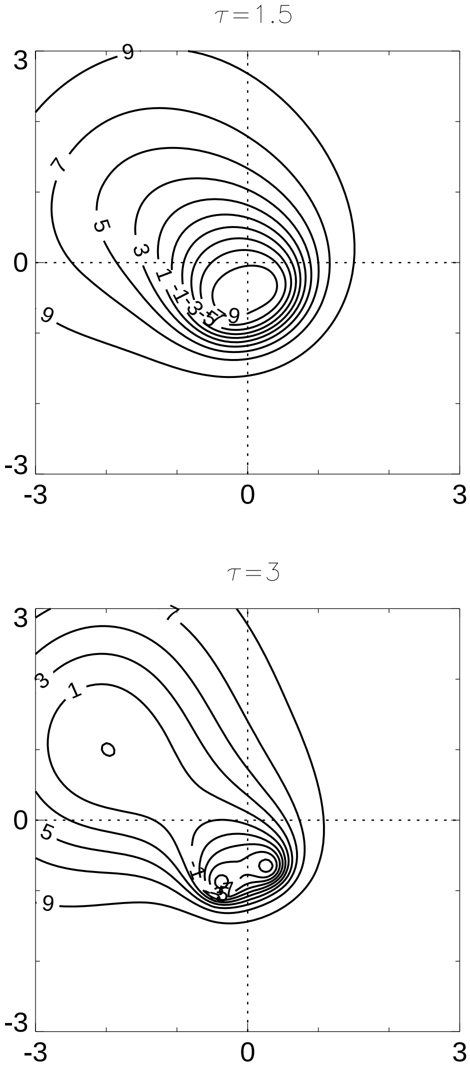

Fig. 13b: Contour plot of the third component of the magnetization multiplied by ten: $10m_3$. The bubble (5.2) is evolved within the exchange model with the external field (5.4). We use a dissipation constant λ =0.25. We give two snapshots, at times τ =1.5 and τ =3.

Figs. 11a,b,c as well as the time series expansions give a picture of the overall motion of the bubble, but the details of the configuration are also important. As we mentioned at the end of Section 4, we do not expect a coherent bubble motion in the free spin model. To confirm this expectation we give in Fig. 12a a 2D vector plot produced with the results of our numerical simulation of the free spin model at times $\tau = 1.5$ and $\tau = 3$. The magnetization vector is represented by its projection on the (12) plane. In Fig. 12b, we give the corresponding contour plots for the third component of the magnetization. Actually we give the contour plot of the quantity $10m_3$. From these two figures we only observe a distortion of the bubble during the process without any sign of a bubble moving as a whole. In particular the point where $S_3 = 0$, defined some times as the center of the bubble, is always set at the origin.

The situation changes to a considerable extent when the exchange model is simulated. In Figs. 13a and 13b we give the corresponding 2D spin plots and also the contour plots for m_3 which should be compared to those of Figs. 12a,b. Figs. 13a,b show that the exchange interaction helps the bubble move in a more rigid way. This is clear even at $\tau = 1.5$, that is, before any difference in the evolution of the guiding center coordinates between the two models occur. Nevertheless, the bubble does not move in a rigid way even when the exchange interaction is present. But this is, to a large extent, attributed to the conformal invariance of the model and the ensuing metastability of the bubble. We note especially the shrinking of the configuration which can be attributed to the scale invariance of the Heisenberg model.

To avoid the effects introduced due to the scale invariance of the Heisenberg model we may add a Skyrme term in the Hamiltonian to set a scale and thus stabilize the bubble [11]. If an external field is also included in this model, the motion of the bubble is rather coherent and basically follow the motion of the guiding center. However a sharp transient period is observed at the beginning of the process and then the bubble follows an almost straight line orbit for an intermediate period of time; but a steady state is never achieved and the long time behavior of the bubble is sensitive to the details of the gradient at large distances.

In conclusion we have found that the general features of the bubble motion are clear and independant of the particular model. Furthermore the bubble is generaly following its guiding center but the details of its motion depend on the model as well as on the form of the external field. On the other hand, a pair of bubble with winding numbers of the same sign are expected to orbit around each other while two bubbles with winding numbers with opposite sign should move in formation along roughly parallel lines. Numerical simulations within the Skyrme model [11] have confirmed this picture and have shown that each of the bubbles move in a coherent way and follow quite faithfully their guiding centers.

CHAPTER III

TWO-DIMENSIONAL ANTIFERROMAGNETS

1. Introduction

We have seen in the previous chapters that topological magnetic solitons have been studied extensively in the case of ferromagnets (FM). Extensive studies have also been performed for weak ferromagnets (WFM). In both cases a nonvanishing magnetization develops in the ground state, albeit by a different physical mechanism, which allows a detailed experimental investigation by standard techniques [1,9]. In contrast, direct experimental evidence for pure antiferromagnetic (AFM) solitons is limited. Nevertheless, theoretical arguments suggest that static AFM solitons should exist for essentially the same reason as in ordinary ferromagnets, even though their dynamics is significantly different.

The dynamics is now governed by suitable extensions of the relativistic nonlinear σ model [9] instead of the Landau-Lifshitz equation [1]. Therefore dynamical concepts familiar from the theory of FM domain walls and bubbles need to be reanalyzed within the relativistic theory. It is our general purpose in this chapter to pursue a study of the dynamics of two-dimensional (2D) AFM solitons that emphasizes the influence of the underlying topological structure. Our starting point is some recent work on AFM and WFM domain walls [29] which revealed that some important issues in the derivation of the associated nonlinear σ model had been mistreated in earlier treatments. We are thus sufficiently motivated to extend the analysis of Refs. [29] to the case of layered or 2D antiferromagnets whose significance has increased in recent years in connection with high-T_c superconductivity.

In the present work we proceed by a combination of numerical and analytical methods. Numerical calculations will be performed within the standard discrete spin model. However a transparent interpretation of the numerical results could not be achieved without the aid of a continuum approximation at the heart of which lies the relativistic nonlinear σ model. A complete account of the continuum model is given in Section 2 where we discuss, in particular, the relevance of certain parity-breaking contributions that are implicit in spin models involving antiferromagnetic interactions. Numerical and analytical results are then combined in Section 3 to provide a complete description of static AFM vortices.

Subsequent sections are devoted to a detailed study of some special dynamical features due to the underlying topology. For instance, head-on collisions of vortices are examined in Section 4 and shown to exhibit a characteristic 90° scattering pattern familiar from similar studies of relativistic skyrmions and monopoles [30, 27]. The most surprising element is described in Section 5 where it is shown that an applied uniform magnetic field affects vortex dynamics rather profoundly. We follow the theoretical analysis We follow the theoretical analysis given in Chapters I and II and establish a direct link between topology and dynamics by means of the conservation laws of linear and angular momentum expressed as moments of a suitable topological vorticity. Possible phenomenological implications of the derived dynamical picture are further discussed in the concluding Section 6. The present chapter is based on the work presented in [31].

2. The nonlinear σ model

We shall study a spin system described by the Hamiltonian

$$W = \sum_{ij} [J\, \mathbf{S}_{i,j} \cdot (\mathbf{S}_{i+1,j} + \mathbf{S}_{i,j+1}) + \frac{1}{2} g (S^3_{i,j})^2], \tag{2.1}$$

where the summation extends over all sites of a square lattice, $\mathbf{S}_{i,j}$ is the spin vector at site (i,j) and $S^3_{i,j}$ its third component. Both the exchange constant J and the anisotropy constant g are taken to be positive and hence (2.1) describes a Heisenberg antiferromagnet with an easy-plane single ion anisotropy.

The spin variables are treated as classical vectors with constant magnitude s and satisfy the equation of motion

$$\frac{\partial \mathbf{S}_{i,j}}{\partial t} = \mathbf{S}_{i,j} \times \mathbf{F}_{i,j}, \qquad \mathbf{S}^2_{i,j} = s^2, \tag{2.2}$$

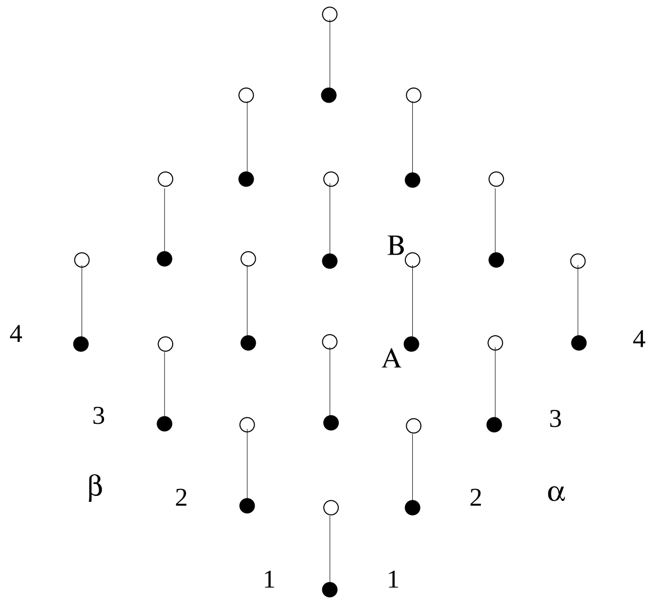

Fig. 14: Illustration of the dimerization process for a finite portion of the square lattice cut along the diagonals. Solid and open circles denote the sites of the two intertwining sublattices.

where the effective field $\mathbf{F}$ is determined from the general relation

$$\mathbf{F}_{i,j} = -\frac{\partial W}{\partial \mathbf{S}_{i,j}}, \tag{2.3}$$

or, more explicitly, by

$$\mathbf{F}_{i,j} = -J(\mathbf{S}_{i+1,j} + \mathbf{S}_{i-i,j} + \mathbf{S}_{i,j+1} + \mathbf{S}_{i,j-1}) - gS^3_{i,j}\mathbf{e}, \tag{2.4}$$

where $\mathbf{e} = (0, 0, 1)$ is a unit vector along the third direction. The exchange contribution in the effective field (2.4) contains fewer than four terms on the perimeter of a finite lattice, the precise number of such terms being equal to the number of nearest neighbors. All dynamical simulations presented in this chapter will be based on the above relatively simple set of discrete equations adapted to an open finite lattice.

However, in order to pursue an efficient study of the dynamics, we also consider a continuum approximation which is possible at weak anisotropy,

$$\varepsilon = \sqrt{\frac{g}{J}} \ll 1, \tag{2.5}$$

where soliton structures extend over a large number of sites given roughly by $1/\varepsilon$. The continuum limit is not completely straightforward because of the implicit antiferromagnetic discontinuity as one moves from site to site. It is then important to first identify dynamical variables that may possess a smooth limit as $\varepsilon \to 0$.

In one dimension continuity is achieved by a simple dimerization process [29]. A square lattice may also be thought of as a collection of dimers, as illustrated in Fig. 14 for a finite lattice cut along the diagonals. The sites of the original square lattice are depicted by two sets of (solid and open) circles which form two intertwining sublattices. This designation is used merely to indicate that the two spins of any given dimer belong to different sublattices. In particular, the ground (Néel) state is such that the two spins point in opposite directions but are uniform on each sublattice. Because of the easy-plane anisotropy the Néel state is polarized along any direction in the plane perpendicular to the third axis. This azimuthal degeneracy of the ground state will play an important role in the following.

A generic dimer AB (see Fig. 14) is labeled by a pair of indices (α, β) numbered consecutively $(\alpha, \beta = 1, 2, \ldots, N)$. In our explicit illustrations N is taken to be even, but this is only a minor technical assumption. Let us denote by $\mathbf{A}_{\alpha,\beta}$ and $\mathbf{B}_{\alpha,\beta}$ the two spins of dimer AB. Eq. (2.2) is then written as a system of two coupled equations,

$$\frac{\partial \mathbf{A}_{\alpha,\beta}}{\partial t} = \mathbf{A}_{\alpha,\beta} \times \mathbf{F}_{\alpha,\beta} \qquad \frac{\partial \mathbf{B}_{\alpha,\beta}}{\partial t} = \mathbf{B}_{\alpha,\beta} \times \mathbf{G}_{\alpha,\beta}, \tag{2.6}$$

where the effective fields $\mathbf{F}$ and $\mathbf{G}$ are given by

$$\begin{aligned} \mathbf{F}_{\alpha,\beta} &= -J(\mathbf{B}_{\alpha,\beta} + \mathbf{B}_{\alpha-1,\beta} + \mathbf{B}_{\alpha,\beta-1} + \mathbf{B}_{\alpha-1,\beta-1}) - gA^3_{\alpha,\beta}\mathbf{e}, \\ \mathbf{G}_{\alpha,\beta} &= -J(\mathbf{A}_{\alpha,\beta} + \mathbf{A}_{\alpha+1,\beta} + \mathbf{A}_{\alpha,\beta+1} + \mathbf{A}_{\alpha+1,\beta+1}) - gB^3_{\alpha,\beta}\mathbf{e}, \end{aligned} \tag{2.7}$$

for a generic point inside the lattice. The exchange contributions in Eq. (2.7) contain only two terms for each point on the perimeter of the finite lattice of Fig. 14.

As a first step in the derivation of a continuum approximation we introduce the discrete set of variables

$$\eta = \sqrt{2}\,\varepsilon(\alpha - \alpha_0), \qquad \xi = \sqrt{2}\,\varepsilon(\beta - \beta_0), \tag{2.8}$$

which become continuous in the limit $\varepsilon \to 0$ and provide a measure of distances along the diagonals of the square lattice. Actual distances are given by $a\eta/\varepsilon$ and $a\xi/\varepsilon$ where a is the physical distance between two neighboring magnetic ions. The lattice constant a will not appear in our theoretical development except when various quantities of interest will have to be translated in physical units. Finally the convenient choice $\alpha_0 = (N+1)/2 = \beta_0$ in Eq. (2.8) sets the origin of the coordinate system at the center of the lattice of Fig. 14.

The main assumption supported by numerical calculations is that the spin variables $\mathbf{A}_{\alpha,\beta}$ and $\mathbf{B}_{\alpha,\beta}$ approach smooth continuum limits $\mathbf{A} = \mathbf{A}(\eta, \xi)$ and $\mathbf{B} = \mathbf{B}(\eta, \xi)$

at weak anisotropy ($\varepsilon \to 0$). Then we make the substitutions $\mathbf{A}_{\alpha,\beta} \to \mathbf{A}$ and $\mathbf{B}_{\alpha,\beta} \to \mathbf{B}$ in Eqs. (2.6)-(2.7) together with the Taylor expansions

$$\begin{aligned} \mathbf{A}_{\alpha\pm1,\beta} &\to \mathbf{A} \pm \delta\mathbf{A}_\eta + \frac{1}{2}\delta^2\mathbf{A}_{\eta\eta}, \\ \mathbf{A}_{\alpha,\beta\pm1} &\to \mathbf{A} \pm \delta\mathbf{A}_\xi + \frac{1}{2}\delta^2\mathbf{A}_{\xi\xi}, \\ \mathbf{A}_{\alpha\pm1,\beta\pm1} &\to \mathbf{A} \pm \delta(\mathbf{A}_\eta + \mathbf{A}_\xi) + \frac{1}{2}\delta^2(\mathbf{A}_{\eta\eta} + \mathbf{A}_{\xi\xi} + 2\mathbf{A}_{\eta\xi}), \end{aligned} \tag{2.9}$$

and similar expansions for the field $\mathbf{B}$. Here subscripts denote differentiation with respect to the indicated arguments and

$$\delta = \sqrt{2}\,\varepsilon \tag{2.10}$$

is used as a temporary notational abbreviation. Eqs. (2.6) are then approximated by

$$\frac{\partial\mathbf{A}}{\partial t} = \mathbf{A}\times\mathbf{F}, \qquad \frac{\partial\mathbf{B}}{\partial t} = \mathbf{B}\times\mathbf{G}, \tag{2.11}$$

where

$$\begin{aligned} \mathbf{F} &= -J[4\mathbf{B} - 2\delta(\mathbf{B}_\eta + \mathbf{B}_\xi) + \delta^2(\mathbf{B}_{\eta\eta} + \mathbf{B}_{\xi\xi} + \mathbf{B}_{\eta\xi})] - gA_3\mathbf{e}, \\ \mathbf{G} &= -J[4\mathbf{A} + 2\delta(\mathbf{A}_\eta + \mathbf{A}_\xi) + \delta^2(\mathbf{A}_{\eta\eta} + \mathbf{A}_{\xi\xi} + \mathbf{A}_{\eta\xi})] - gB_3\mathbf{e}. \end{aligned} \tag{2.12}$$

This system of equations is not yet fully consistent because it appears to mix different powers of δ (or ε).

In order to obtain a consistent continuum model we proceed as in the 1D case studied in Ref. [29]. First, we introduce the linear combination of fields

$$\mathbf{m} = \frac{1}{2s}(\mathbf{A}+\mathbf{B}), \qquad \mathbf{n} = \frac{1}{2s}(\mathbf{A}-\mathbf{B}), \tag{2.13}$$

which satisfy the constraints

$$\mathbf{m}\cdot\mathbf{n} = 0, \qquad \mathbf{m}^2 + \mathbf{n}^2 = 1. \tag{2.14}$$

Second, we define a dimensionless time variable

$$\tau = 2\delta sJt = 2\sqrt{2}\,\varepsilon sJt. \tag{2.15}$$

An equivalent form of Eqs. (2.11) then reads

$$\begin{aligned}
\delta\frac{\partial \mathbf{m}}{\partial \tau} =& -\delta[(\mathbf{m}\times\mathbf{n})_\eta + (\mathbf{m}\times\mathbf{n})_\xi] + \frac{1}{2}\delta^2[\mathbf{n}\times(\mathbf{n}_{\eta\eta}+\mathbf{n}_{\xi\xi}+\mathbf{n}_{\eta\xi}) \\
& -\mathbf{m}\times(\mathbf{m}_{\eta\eta}+\mathbf{m}_{\xi\xi}+\mathbf{m}_{\eta\xi})] - \frac{1}{4}\delta^2[m_3(\mathbf{m}\times\mathbf{e}) + n_3(\mathbf{n}\times\mathbf{e})], \\
\delta\frac{\partial \mathbf{n}}{\partial \tau} =& 4(\mathbf{m}\times\mathbf{n}) + \delta[\mathbf{m}\times(\mathbf{m}_\eta+\mathbf{m}_\xi) - \mathbf{n}\times(\mathbf{n}_\eta+\mathbf{n}_\xi)] \\
& + \frac{1}{2}\delta^2[\mathbf{m}\times(\mathbf{n}_{\eta\eta}+\mathbf{n}_{\xi\xi}+\mathbf{n}_{\eta\xi}) - \mathbf{n}\times(\mathbf{m}_{\eta\eta}+\mathbf{m}_{\xi\xi}+\mathbf{m}_{\eta\xi})] \\
& - \frac{1}{4}\delta^2[m_3(\mathbf{n}\times\mathbf{e}) + n_3(\mathbf{m}\times\mathbf{e})].
\end{aligned} \tag{2.16}$$

A simple inspection of the above equations suggests that consistency is obtained if $\mathbf{m}$ is of order δ. Then the leading approximation of the second equation is

$$\delta\frac{\partial \mathbf{n}}{\partial \tau} = 4(\mathbf{m}\times\mathbf{n}) - \delta[\mathbf{n}\times(\mathbf{n}_\eta+\mathbf{n}_\xi)] \tag{2.17}$$

and the constraints of Eq. (2.14) reduce to

$$\mathbf{m}\cdot\mathbf{n} = 0, \qquad \mathbf{n}^2 = 1, \tag{2.18}$$

to within terms of order δ^2. Therefore taking the cross product of both sides of Eq. (2.17) with $\mathbf{n}$ and using the constraints (2.18) yields

$$\mathbf{m} = \frac{\varepsilon}{2\sqrt{2}}[-(\mathbf{n}_\eta+\mathbf{n}_\xi) + (\mathbf{n}\times\dot{\mathbf{n}})], \tag{2.19}$$

where we have restored the small parameter ε from Eq. (2.10). Finally Eq. (2.19) is inserted in the first of Eqs. (2.16) to give in the limit $\varepsilon \to 0$ the differential equation

$$\mathbf{n}\times\mathbf{f} = 0, \qquad \mathbf{f} = \ddot{\mathbf{n}} - \Delta\mathbf{n} + n_3\mathbf{e}, \tag{2.20}$$

where Δ is the 2D Laplacian

$$\Delta = \frac{\partial^2}{\partial\eta^2} + \frac{\partial^2}{\partial\xi^2}. \tag{2.21}$$

It is understood that terms of order ε^2 in Eqs. (2.18), (2.20) and order ε^3 in Eq. (2.19) have been neglected.

Therefore the continuum approximation is governed mainly by Eq. (2.20) which is a simple extension of the relativistic nonlinear σ model to include a single ion anisotropy. The corresponding velocity of light is equal to unity thanks to our choice of rationalized space and time variables. In our conventions, the spin magnitude s is a simple multiple of the Planck constant (e.g., $s = \frac{1}{2}\hbar$) and thus carries dimension of action, sJ of frequency and $s^2 J$ of energy. The ratio ε of Eq. (2.5) is dimensionless, so is the time variable τ of Eq. (2.15). Also recalling that actual distances are given by $a\eta/\varepsilon$ and $a\xi/\varepsilon$, where a is the lattice constant, we conclude that velocity is measured in units of

$$c = 2\sqrt{2}asJ, \tag{2.22}$$

which coincides with the phase velocity of pure AFM magnons on a square lattice in the long-wavelength limit. More generally, the magnon velocity is given by

$$c = 2asJ\sqrt{\frac{z}{2}}, \tag{2.23}$$

where z is the lattice coordination number. Applied for a square lattice ($z = 4$) Eq. (2.23) reduces to Eq. (2.22), whereas for a chain ($z = 2$) it yields the limiting velocity $c = 2asJ$ of Refs. [29].

Needless to say, a complete description of the original spin model requires knowledge of both fields $\mathbf{m}$ and $\mathbf{n}$. On the other hand, given a solution $\mathbf{n} = \mathbf{n}(\eta, \xi, \tau)$ of the nonlinear σ model, the field $\mathbf{m}$ may be determined from Eq. (2.19) by simple differentiations and may thus be viewed as an auxiliary field. Yet this apparently straightforward result has been controversial. For instance, the parity-breaking gradient terms in Eq. (2.19) were recently derived within the 1D model and shown to be important for various structural properties of AFM and WFM domain walls [29]. The possible occurrence of such terms had been anticipated on symmetry grounds [32] but this possibility was overlooked in the literature for a long time [33].

One should stress that symmetry arguments do not predict the precise coefficients of the parity-breaking gradient terms in Eq. (2.19) and are generally susceptible to overinterpretation. The danger from this dimerization ambiguity is already present in one dimension and was completely analyzed in Refs. [29]. The situation is only compounded in two dimensions. For example, had we chosen to work with a horizontal instead of the vertical dimerization of Fig. 14, the nonlinear σ model of Eq. (2.20) would not be affected but the gradient terms in Eq. (2.19) would appear as $\mathbf{n}_\eta - \mathbf{n}_\xi$ instead of $\mathbf{n}_\eta + \mathbf{n}_\xi$. This is an indication that the local values of the field $\mathbf{m}$ are sensitive to the mode of dimerization and cannot be literally interpreted as magnetization. However no real mathematical or physical ambiguity appears when the results of a calculation or an experiment are consistently interpreted in reference to a specific mode of dimerization. But an attempt to measure the "magnetization" $\mathbf{m}$ by standard

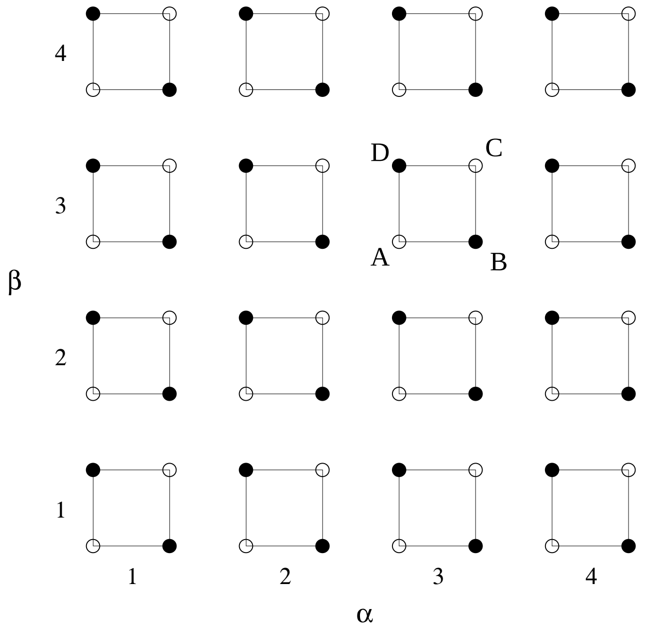

Fig. 15: Illustration of the tetramerization process of a finite portion of the square lattice.

techniques may lead to a fuzzy magnetization curve around any nontrivial soliton structure, unless spin values can be resolved at every site [29].

To press the above picture further we note that dimerization is not the only way to achieve continuity on a square antiferromagnetic lattice. We may also consider the tetramerous configuration illustrated for a finite lattice in Fig. 15. Each tetramer is again labeled by two indices α and β numbered consecutively $(\alpha, \beta = 1, 2, \ldots, N)$ and spin values are smooth as one moves from corresponding sites of one tetramer to the next. Let us again denote by $\mathbf{A}_{\alpha,\beta}$, $\mathbf{B}_{\alpha,\beta}$, $\mathbf{C}_{\alpha,\beta}$ and $\mathbf{D}_{\alpha,\beta}$ the spins on a generic tetramer $ABCD$ shown in Fig. 15, in terms of which the original equation of motion (2.2) may be written as a system of four coupled equations analogous to Eqs. (2.6). This new system may then be used for the derivation of the continuum approximation by a method similar to the one explained earlier within the dimerization scheme of Fig. 14.

We omit the lengthy algebraic details and simply state the final results. We now use the Cartesian coordinates

$$x = 2\varepsilon(\alpha - \alpha_0), \qquad y = 2\varepsilon(\beta - \beta_0), \tag{2.24}$$

which are related to the coordinates η and ξ of Eq. (2.8) by a 45° rotation. Here the origin of the coordinate system is again set at the center of the lattice of Fig. 15 by choosing the arbitrary constants as $\alpha_0 = (N+1)/2 = \beta_0$. Next we assume that the four spins on a tetramer approach smooth continuum limits when $\varepsilon \to 0$ denoted by $\mathbf{A}, \mathbf{B}, \mathbf{C}$ and $\mathbf{D}$ which are some functions of the spatial coordinates x and y of Eq. (2.24) and the time variable τ of Eq. (2.15). A more convenient set of fields is given by

$$\begin{aligned} \mathbf{m} &= \frac{1}{4s}(\mathbf{A}+\mathbf{B}+\mathbf{C}+\mathbf{D}), \qquad & \mathbf{n} &= \frac{1}{4s}(\mathbf{A}-\mathbf{B}+\mathbf{C}-\mathbf{D}), \\ \mathbf{k} &= \frac{1}{4s}(\mathbf{A}+\mathbf{B}-\mathbf{C}-\mathbf{D}), \qquad & \mathbf{l} &= \frac{1}{4s}(\mathbf{A}-\mathbf{B}-\mathbf{C}+\mathbf{D}), \end{aligned} \tag{2.25}$$

and satisfy the constraints

$$\begin{aligned} \mathbf{m}^2+\mathbf{n}^2+\mathbf{k}^2+\mathbf{l}^2 &= 1, \qquad & \mathbf{m}\cdot\mathbf{k}+\mathbf{n}\cdot\mathbf{l} &= 0, \\ \mathbf{m}\cdot\mathbf{n}+\mathbf{k}\cdot\mathbf{l} &= 0, \qquad & \mathbf{m}\cdot\mathbf{l}+\mathbf{n}\cdot\mathbf{k} &= 0. \end{aligned} \tag{2.26}$$

In the strict continuum limit ($\varepsilon \to 0$) the constraints reduce to

$$\mathbf{m}\cdot\mathbf{n} = \mathbf{k}\cdot\mathbf{n} = \mathbf{l}\cdot\mathbf{n} = 0, \qquad \mathbf{n}^2 = 1, \tag{2.27}$$

the fields $\mathbf{m}, \mathbf{k}$ and $\mathbf{l}$ are expressed in terms of $\mathbf{n}$ by

$$\mathbf{m} = \frac{\varepsilon}{2\sqrt{2}}(\mathbf{n}\times\dot{\mathbf{n}}), \qquad \mathbf{k} = -\frac{\varepsilon}{2}\mathbf{n}_x, \qquad \mathbf{l} = -\frac{\varepsilon}{2}\mathbf{n}_y, \tag{2.28}$$

and $\mathbf{n}$ itself satisfies the differential equation

$$\mathbf{n}\times\mathbf{f} = 0, \qquad \mathbf{f} = \ddot{\mathbf{n}} - \Delta\mathbf{n} + n_3\mathbf{e}, \tag{2.29}$$

where Δ is the 2D Laplacian

$$\Delta = \frac{\partial^2}{\partial x^2} + \frac{\partial^2}{\partial y^2}. \tag{2.30}$$

It is again understood that Eqs. (2.27)-(2.29) are accurate to within terms of order ε^2.

Although the field $\mathbf{n}$ defined in Eq. (2.25) is not directly related to the field $\mathbf{n}$ of Eq. (2.13), its continuum dynamics is still governed by the nonlinear σ model of Eq. (2.29) which is equivalent to Eq. (2.20). However a clear distinction between the two formulations emerges at the level of the auxiliary fields. We now need three such fields ($\mathbf{m}, \mathbf{k}$ and $\mathbf{l}$) which are expressed in terms of $\mathbf{n}$ through Eqs. (2.28). These relations reenforce our earlier remarks concerning parity-breaking contributions, namely that they are sensitive to the specific mode of taking the continuum limit. For instance, such contributions are no longer present in the field $\mathbf{m}$ but their effect is accounted for by the new auxiliary fields **k** and **l**. Once again we must conclude that the local values of the field **m** cannot be interpreted literally as magnetization.

The perplexing nature of the auxiliary fields calls for a summary of our main strategy. The continuum model is extensively used to motivate the results discussed in subsequent sections. But all numerical calculations are based on the original discrete equation (2.2). The actual calculations may be performed on an open finite lattice either of the type shown in Fig. 14 or that of Fig. 15. The explicit results may then be employed to construct the fields **m** and **n** in the former case and the fields **m**, **n**, **k** and **l** in the latter. In both cases the validity of the respective continuum models can be verified explicitly for a sufficiently weak anisotropy ($\varepsilon \ll 1$). Nonetheless several apparent paradoxes emerged in the course of our investigation which were all resolved in favor of the formulation presented in this section.

3. Static vortices

We consider first the problem of finding interesting static solutions within the continuum model. In both formulations developed in the previous section, the basic issue is to determine the field **n** from the nonlinear σ model and then proceed with the calculation of the auxiliary fields. Time derivatives vanish in the static limit and one obtains the reduced equations

$$\mathbf{n} \times \mathbf{f} = 0, \qquad \mathbf{f} = -\Delta \mathbf{n} + n_3 \mathbf{e}. \tag{3.1}$$

It proves convenient to derive the field **f** from a variational argument,

$$\mathbf{f} = \frac{\delta W}{\delta \mathbf{n}}, \qquad W = \frac{1}{2} \int [(\partial_\mu \mathbf{n} \cdot \partial_\mu \mathbf{n}) + n_3^2] dx dy, \tag{3.2}$$

where W is the energy functional in the static limit (see Section 5). The repeated index is summed over two distinct values $\mu = 1$ and 2 corresponding to the two spatial coordinates x and y (or η and ξ). It is also useful to resolve the constraint $\mathbf{n}^2 = 1$ explicitly using, for example, the spherical parametrization

$$n_1 = \sin\Theta \cos\Phi, \qquad n_2 = \sin\Theta \sin\Phi, \qquad n_3 = \cos\Theta \tag{3.3}$$

in terms of which

$$W = \frac{1}{2} \int [(\partial_\mu \Theta \partial_\mu \Theta) + \sin^2\Theta \, (\partial_\mu \Phi \partial_\mu \Phi) + \cos^2\Theta] dx dy \tag{3.4}$$

and Eqs. (3.1) are equivalent to

$$\frac{\delta W}{\delta \Theta} = 0 = \frac{\delta W}{\delta \Phi}, \tag{3.5}$$

or

$$\Delta\Theta + [1 - (\partial_\mu \Phi \partial_\mu \Phi)] \cos\Theta \sin\Theta = 0, \qquad \partial_\mu(\sin^2\Theta\, \partial_\mu \Phi) = 0. \tag{3.6}$$

It should be noted that the above static equations are formally identical to those encountered in easy-plane ferromagnets. However the physical interpretation of the field **n** is now different and the actual construction of the corresponding AFM solitons on the discrete lattice is effected by the prescriptions of Section 2.

The simplest solution of Eqs. (3.6) is the ground state configuration $\Theta = \frac{\pi}{2}$ and $\Phi = \phi_0$, where ϕ_0 is an arbitrary constant, for which the energy achieves its absolute minimum ($W = 0$). Such a simple configuration ($n_1 = \cos\phi_0$, $n_2 = \sin\phi_0$, $n_3 = 0$) is consistent with our earlier remark that the ground state is the usual Néel state with spins polarized along any direction in the (12) plane. Nontrivial static solutions are also stationary points of the energy functional W and are subject to limitations imposed by the familiar scaling theorem of Derrick [13]. Applied for the functional (3.4) Derrick's argument yields the virial relation

$$\int \cos^2\Theta \, dxdy = 0. \tag{3.7}$$

Therefore one must conclude that nontrivial static solutions with finite energy do not exist.

The above argument does not exclude interesting solutions with infinite energy such as vortices. In fact, the possible existence of vortices is probed by a suitable generalization of the Derrick theorem [31]. Eq. (3.7) is then replaced by

$$\int \cos^2\Theta \, dxdy = \pi, \tag{3.8}$$

which not only does not exclude the possibility of vortex solutions but predicts the actual value of their anisotropy energy. However the exchange energy is logarithmically divergent.

To obtain an explicit solution we consider the usual cylindrical coordinates $x = \rho\cos\phi$, $y = \rho\sin\phi$ and make the following ansatz for a vortex located at the origin:

$$\Theta = \theta(\rho), \qquad \Phi = \kappa(\phi + \phi_0), \tag{3.9}$$

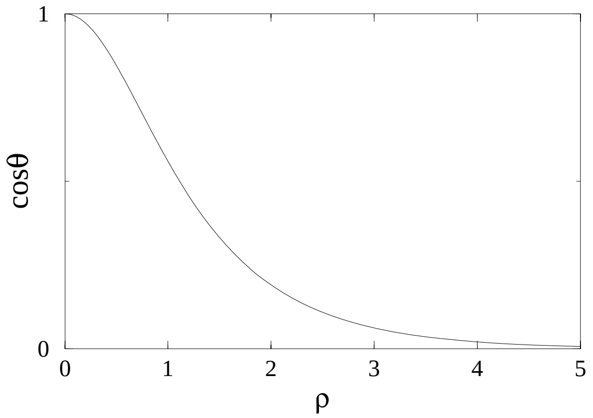

Fig. 16: The numerically calculated profile of a static vortex at weak anisotropy.

where $\kappa = \pm 1$ will be referred to as the vortex number and ϕ_0 is an arbitrary constant reflecting the azimuthal symmetry. Then the second equation in (3.6) is automatically satisfied and the first yields

$$\frac{1}{\rho}\frac{\partial}{\partial\rho}\left(\rho\frac{\partial\theta}{\partial\rho}\right) + \left(1 - \frac{1}{\rho^2}\right)\cos\theta\sin\theta = 0. \tag{3.10}$$

The energy (3.4) is accordingly reduced to

$$W = \frac{1}{2}\int_0^\infty \left[\left(\frac{\partial\theta}{\partial\rho}\right)^2 + \frac{\sin^2\theta}{\rho^2} + \cos^2\theta\right](2\pi\rho d\rho) \tag{3.11}$$

and its stationary points are solutions of Eq. (3.10). This equation is consistent with the asymptotic behavior

$$\theta \underset{\rho\to 0}{\approx} c_1\rho, \qquad \theta \underset{\rho\to\infty}{\approx} \frac{\pi}{2} - \frac{c_2 e^{-\rho}}{\sqrt{\rho}}, \tag{3.12}$$

where c_1 and c_2 are some constants. The actual solution depicted in Fig. 16 was calculated numerically via a relaxation algorithm applied to the restricted energy functional (3.11) taking into account the boundary values (3.12).

Furthermore we note that for every solution θ of Eq. (3.10) a new solution is obtained by the formal replacement $\theta \to \pi - \theta$. Hence the complete result for the field $\mathbf{n} = (n_1, n_2, n_3)$ reads

$$n_1 = \sin\theta\cos[\kappa(\phi+\phi_0)], \qquad n_2 = \sin\theta\sin[\kappa(\phi+\phi_0)], \qquad n_3 = \nu\cos\theta, \tag{3.13}$$

where $\theta = \theta(\rho)$ is taken from Fig. 16, while the vortex number κ and the polarity ν are given by

$$\kappa = \pm 1, \qquad \nu = \pm 1, \tag{3.14}$$

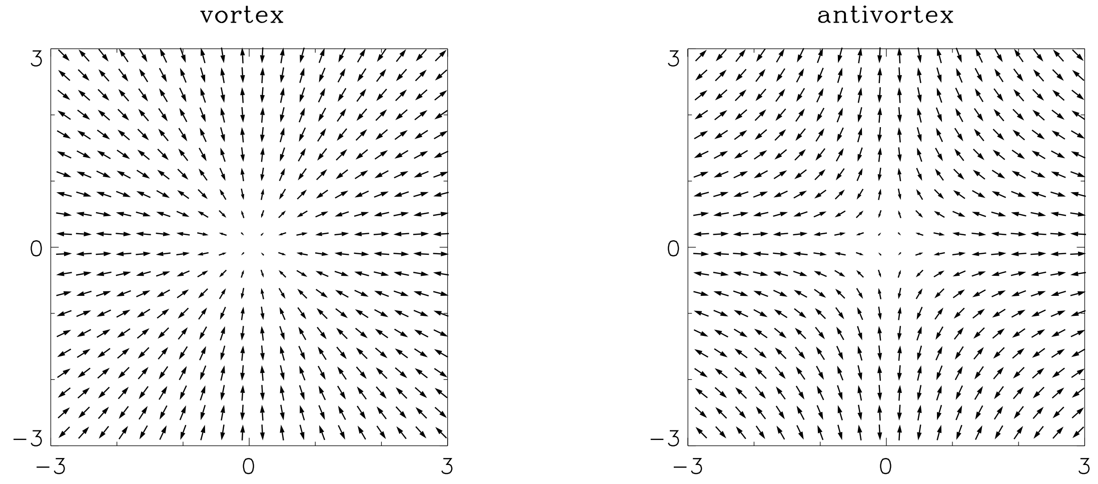

Fig. 17: Spin vectors of a vortex and an antivortex projected on the (12) plane. Spins are shown at every fourth site of the original lattice and distances on the grid are measured according to Eq. (2.24) applied with ε =0.1.

taken in any combination. In other words, both the vortex ($\kappa = 1$) and the antivortex ($\kappa = -1$) come in two varieties ($\nu = \pm 1$).

The asymptotic behavior (3.12) makes it evident that the centrifugal (second) term in the energy (3.11) diverges logarithmically with the size of the system but the remaining terms are finite. In fact, the numerically calculated anisotropy contribution was found to be in excellent agreement with virial relation (3.8). The weak (logarithmic) divergence of the total energy is not necessarily an obstacle to the production of vortices in an antiferromagnet. In this respect, one should recall that vortices are easily produced in a rotating cylindrical bucket filled with an ordinary fluid or a superfluid [34]. Furthermore vortex-antivortex pairs have finite energy and should play an important role in thermodynamics.

Keeping with the strategy outlined in the concluding paragraph of Section 2, we must comment on the manner in which Eq. (3.13) furnishes a vortex on the discrete lattice. The field $\mathbf{n}$ of Eq. (3.13) may be used to calculate the auxiliary field $\mathbf{m}$ of Eq. (2.19) or the fields $\mathbf{m}, \mathbf{k}$ and $\mathbf{l}$ of Eq. (2.28), applied for a static solution ($\dot{\mathbf{n}} = 0$), and thereby determine the original spin configuration on the lattices of Fig. 14 and Fig. 15, respectively. As a check of consistency we have used the resulting spin configuration as initial condition within a fully-dissipative algorithm [29] applied to the complete energy functional (2.1) on a 200 × 200 lattice. The calculated relaxed state accurately reproduced both the profile of Fig. 16 and the corresponding auxiliary fields for a reasonably small value of the anisotropy constant ($\varepsilon = 0.1$). The spin values on the discrete lattice are partially illustrated in Fig. 17 for both a vortex and an antivortex and exhibit the characteristic antiferromagnetic discontinuity between the two sublattices. Finally we mention that a similar calculation of an AFM vortex can be found in Ref. [35] using an Ising-like instead of a single-ion anisotropy.

Since the vortex solutions described above are present for any finite value of the anisotropy, however weak, it is also of interest to examine the extreme limit of vanishing anisotropy. The static equations (3.1) then reduce to

$$\mathbf{n} \times \Delta \mathbf{n} = 0, \qquad \mathbf{n}^2 = 1 \tag{3.15}$$

and are equivalent to the O(3) nonlinear σ model in a 2D Euclidean space. The small parameter ε hidden in the definition of spatial coordinates is no longer related to an anisotropy constant but is an intrinsic scale set by the actual spread of localized solitons. The implied arbitrariness of ε is reflected by the scale invariance of Eq. (3.15) and is already an indication that the corresponding solitons are metastable. Explicit solutions of Eq. (3.15) are the well-known Belavin-Polyakov (BP) instantons [28] viewed here as static solitons in the 2+1 dimensional theory of current interest. They differ from the vortex (3.13) mainly in the asymptotic value of the field $\mathbf{n}$ which is now given by

$$\mathbf{n} \underset{|\mathbf{x}| \to \infty}{\longrightarrow} (0, 0, 1) \tag{3.16}$$

and coincides with the ground state configuration of the isotropic antiferromagnet defined up to a global O(3) rotation. Therefore the BP instantons may be called AFM bubbles, by analogy to FM bubbles [1], discussed in Chapters I and II of this thesis. These are classified by the Pontryagin index or winding number Q defined in Eq. (I.3.10) which is written here again in the present notation:

$$Q = \frac{1}{4\pi} \int q \, dx dy, \qquad q = \frac{1}{2} \varepsilon_{\mu\nu} (\partial_\nu \mathbf{n} \times \partial_\mu \mathbf{n}) \cdot \mathbf{n}, \tag{3.17}$$

where $\varepsilon_{\mu\nu}$ is the 2D antisymmetric tensor. The topological density q may also be expressed in terms of the spherical variables as

$$q = \varepsilon_{\mu\nu} \sin\Theta \, \partial_\nu \Theta \partial_\mu \Phi. \tag{3.18}$$

and we have seen that it plays an important role in the dynamical theory of FM bubbles [5,12].

An examination of the asymptotic behavior of Eq. (3.13) suggests that a vortex may be viewed roughly as a half bubble. To push this remark further we calculate the density q for the vortex configuration (3.13),

$$q = \frac{\kappa \nu}{\rho} \frac{\partial \cos\theta}{\partial \rho}, \tag{3.19}$$

where $\theta = \theta(\rho)$ must be taken from Fig. 16. Therefore the winding number calculated from Eq. (3.17) is found to be

$$Q = \frac{1}{2}\kappa\nu[\cos\theta(\infty) - \cos\theta(0)] = -\frac{1}{2}\kappa\nu \tag{3.20}$$

and depends on both the vortex number κ and the polarity ν. This result confirms the vague notion that a vortex is topologically equivalent to a half bubble ($Q = \pm\frac{1}{2}$). However a modified topological charge that is related to the vortex number but not the polarity will arise more naturally in the dynamical context of Section 5.

4. Head-on collisions

Although static AFM solitons are similar to those encountered in ferromagnets, their dynamics is significantly different. For comparison purposes, it is useful to recall at this point the two main dynamical features of FM bubbles: (a) An FM bubble cannot be found in free translational motion; it is always spontaneously pinned or frozen within the ferromagnetic medium. (b) An FM bubble tends to move in a direction perpendicular to an applied magnetic field gradient. For example, a single bubble will undergo a 90° deflection with respect to an externally supplied uniform gradient in the absence of dissipation. In the case of two or more interacting bubbles, a gradient arises intrinsically and leads to a characteristic relative motion similar to the Hall motion of electric charges in a uniform magnetic field or the motion of vortices in a fluid [11].

Property (a) is clearly not the case for AFM bubbles or vortices because of the Lorentz invariance of the underlying nonlinear σ model. Indeed, for any static vortex $\mathbf{n} = \mathbf{n}(\mathbf{x})$ constructed in the preceding section, a vortex propagating freely with an arbitrary speed $v < 1 (= c)$ in, say, the x-direction may be obtained by the elementary Lorentz transformation

$$\mathbf{n}(x, y) \rightarrow \mathbf{n}\left(\frac{x - v\tau}{\sqrt{1 - v^2}}, y\right). \tag{4.1}$$

One may then calculate the corresponding auxiliary fields from Eq. (2.19) or (2.28), taking into account that the dynamical contribution $(\mathbf{n} \times \dot{\mathbf{n}})$ is no longer vanishing, and subsequently construct the spin configuration on the discrete lattice to obtain a rigidly moving AFM vortex.

Similarly, there is no reason to believe that property (b) is sustained for AFM bubbles or vortices. Yet one should expect that topology will continue to play an important role within the relativistic dynamics. A possible manifestation of a topological effect occurs in the dynamics of two bubbles in a head-on collision. Such a process was studied extensively in the context of the isotropic O(3) nonlinear σ model and shown to exhibit a characteristic 90° scattering pattern [36]. This pattern is certainly unusual from the point of view of ordinary particle dynamics but strongly reminiscent of the 90° deflection of FM bubbles in a field gradient. Of course, the above analogy is superficial but indicates that both the Landau-Lifshitz and the relativistic dynamics are influenced by the underlying topology.

The isotropic nonlinear σ model is special in several ways. In particular, its scale invariance leads to metastable bubbles of arbitrary radius. The radius of each bubble changes during collision and never returns to its initial value [36]. A healthier situation arises in the presence of anisotropy which sets a definite scale for the soliton size. Then individual solitons may be deformed during scattering but will always bounce back to their original shape well after collision. The AFM vortices constructed in Section 3 are examples of 2D solitons with definite scale and their dynamics will be the subject of the remainder of this chapter.

The simplest dynamical experiment is to consider the evolution of a pair of two identical vortices which are initially at rest at a relative distance d. Because vortices are extended structures, the above initial configuration is not uniquely defined and generally depends on the details of the physical process that brings the two vortices to their initial positions. However such details may be important for a short transient period but are not expected to significantly influence the global properties of the ensuing motion, especially when the initial distance d is large. Therefore there exists significant freedom in the construction of the initial configuration. The simplest choice is to consider the product ansatz

$$\Omega(x,y) = \Omega_1\left(x-\frac{d}{2},y\right)\Omega_1\left(x+\frac{d}{2},y\right), \tag{4.2}$$

where Ω is the complex stereographic variable

$$\Omega = \frac{n_1+in_2}{1+n_3} = \tan(\Theta/2)\,e^{i\Phi} \tag{4.3}$$

for the vortex pair and Ω_1 is the corresponding variable for a single vortex. In view of Eq. (3.13) we may write

$$\Omega_1\left(x\pm\frac{d}{2},y\right) = \frac{\sin\theta_\pm}{1+\nu\cos\theta_\pm}e^{i\kappa(\phi_\pm+\phi_0)}, \tag{4.4}$$

where

$$\theta_\pm=\theta(\rho_\pm), \qquad \rho_\pm=\sqrt{\left(x\pm\frac{d}{2}\right)^2+y^2}, \qquad \phi_\pm=\arctan\frac{y}{x\pm\frac{d}{2}}, \tag{4.5}$$

and $\theta = \theta(\rho)$ is the profile of Fig. 16. In our simulations we made the specific choices $\kappa = 1$, $\nu = -1$ and $\phi_0 = 0$. The product ansatz (4.2) is then written as

$$\Omega = f(\rho_+)e^{i\phi_+}f(\rho_-)e^{i\phi_-}, \qquad f(\rho_\pm) = \cot\frac{\theta_\pm}{2} \tag{4.6}$$

and represents a pair of two identical vortices initially at rest, at a relative distance d on the x-axis.

The remaining steps for a complete specification of the initial configuration on the discrete lattice of, say, Fig. 15 proceed as follows. The field $\mathbf{n}$ is obtained by inverting Eq. (4.3) according to Eq. (II.1.3). The auxiliary fields $\mathbf{m}, \mathbf{k}$ and $\mathbf{l}$ are then computed from Eq. (2.28) applied for a static configuration ($\mathbf{n} \times \dot{\mathbf{n}} = 0$). The original spin variables $\mathbf{A}, \mathbf{B}, \mathbf{C}$ and $\mathbf{D}$ on a generic tetramer with coordinates (α, β) are determined from Eq. (2.25) applied for the discrete set of points $x = 2\varepsilon(\alpha - \alpha_0)$ and $y = 2\varepsilon(\beta - \beta_0)$ of Eq. (2.24) with $\alpha, \beta = 1, 2, \ldots, N$. The spin configuration is thus specified at every site of the original lattice.

Having determined the initial configuration, the ensuing evolution of the vortex pair was calculated by a numerical solution of the initial-value problem (2.2)-(2.4) using a fourth-order Runge-Kutta algorithm. Typical runs were performed on a 200×200 lattice for a reasonably weak anisotropy $\varepsilon = 0.1$ that leads to a respectable grid $[-10, 10]$ for the dimensionless position variables x and y. The rigidity of our numerical results was frequently checked on larger lattices, up to 400×400, and stability was improved by reenforcing the constraint $\mathbf{S}_{i,j}^2 = s^2$ at every site of the lattice after every Runge-Kutta step. This numerical trick was borrowed from related simulations in the isotropic nonlinear σ model [27, 36]. On this occasion, it should be emphasized that we do not directly simulate the dynamics of the σ model but rather of the original Heisenberg antiferromagnet. A byproduct of this fact was that various theoretical predictions based on the continuum approximation of Section 2 were verified in detail. In particular, we have been able to illuminate numerous subtle points in connection with the parity-breaking contributions in the auxiliary fields.

The results of the numerical simulation described above revealed no surprises when the two vortices are initially at rest; they begin to drift away from each other along the x-axis apparently in order to minimize their interaction energy. Therefore the calculated behavior is similar to that of two ordinary particles interacting with a repulsive potential. Nevertheless this behavior is already significantly different from the one observed in the case of two interacting FM bubbles which would rotate around each other irrespectively of whether the potential is repulsive or attractive [11].

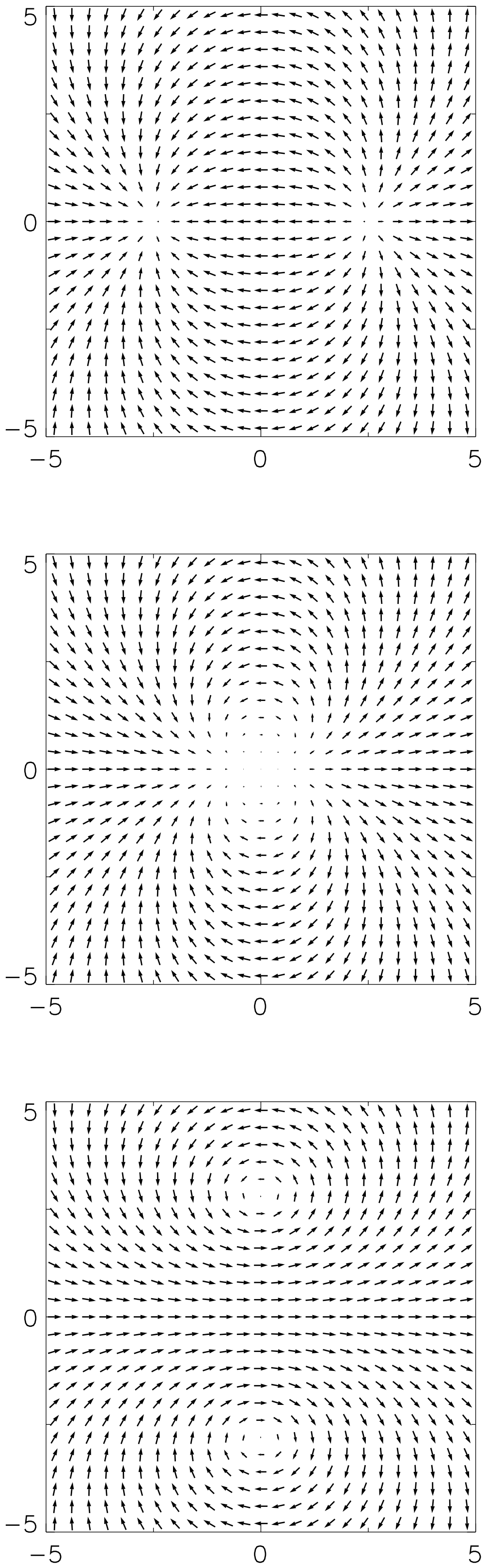

Fig. 18: Three characteristic snapshots of a head-on collision of two like vortices originating at a relative distance d=5 on the x-axis with initial velocities $\mathbf{v}_1$=(0.65, 0) and $\mathbf{v}_2$=(-0.65, 0). After collision the two vortices scatter at 90° and suffer an internal phase shift also equal to 90°. Vectors represent the projection of the field $\mathbf{n}$ on the (12) plane.

A more interesting situation arises when the two vortices in Eq. (4.6) are initially Lorentz boosted to velocities $\mathbf{v}$ and $-\mathbf{v}$ and are thus set on a head-on collision course on the x-axis. As expected, the two vortices begin to discelerate thanks to their mutual repulsion. However the future of the process depends crucially on the magnitude of the initial velocity. At low velocities the two vortices approach each other to a minimum distance at which they come to rest and then turn around and move off in opposite directions. When the initial speed exceeds a certain critical value the vortices again discelerate but come sufficiently close to a relative distance where the interaction potential seems to have become attractive. The vortices then begin to accelerate toward each other until they overlap almost completely. More importantly, they subsequently split and reemerge as two separate vortices moving off along the positive and negative y-direction, thus undergoing a 90° scattering analogous to the one observed in numerical simulations of bubbles in the pure O(3) model [36]. The main difference here is that vortices regain their initial shape except for a flip of their internal phase equal to $\phi_0 = \frac{\pi}{2}$.

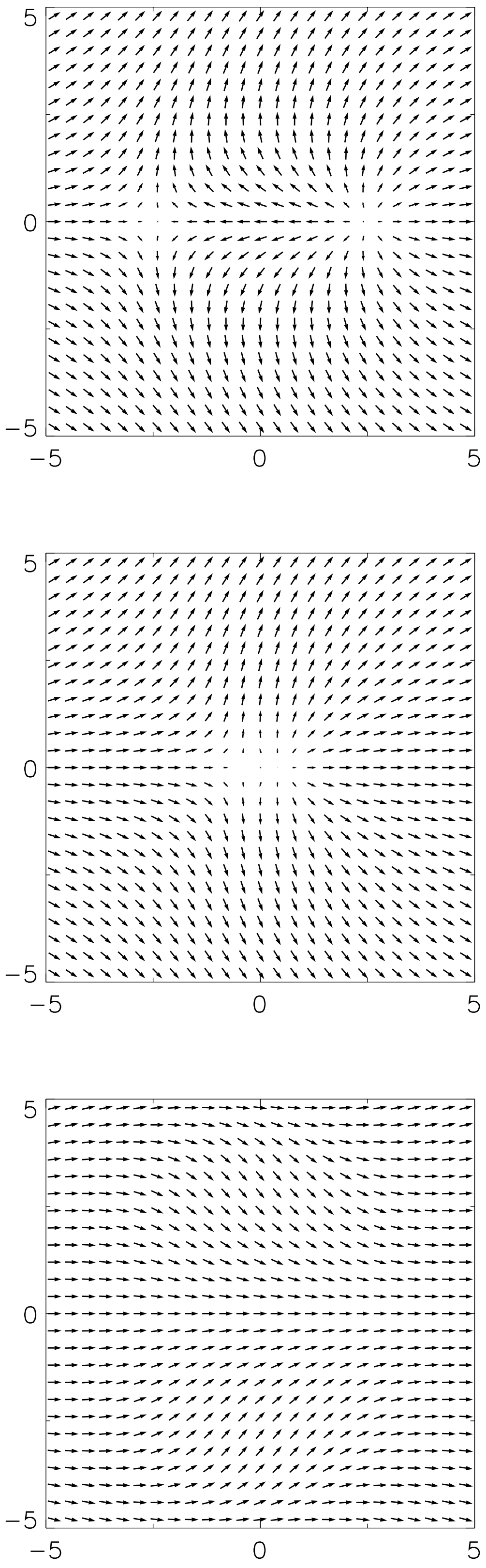

Fig. 19: Three characteristic snapshots of the annihilation process of a vortex and an antivortex that are initially at rest at a relative distance d=5 on the x-axis. The vortex and the antivortex converge toward each other and are eventually annihilated into spinwaves. Vectors represent the projection of the field $\mathbf{n}$ on the (12) plane.

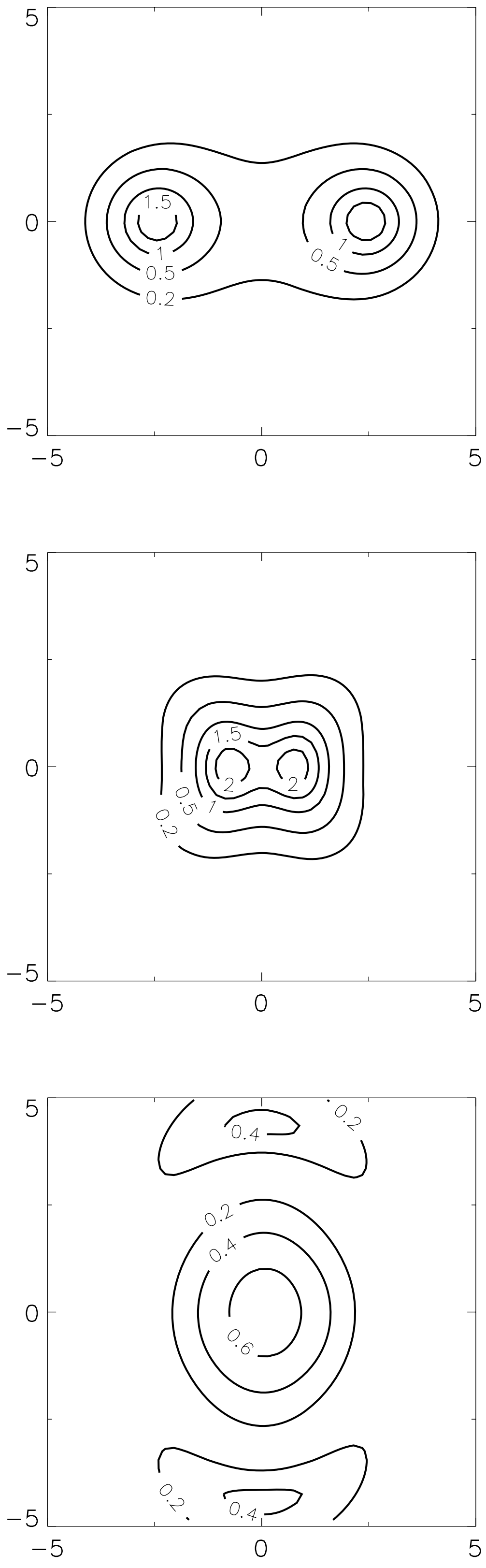

Fig. 20: Level contours of the energy density corresponding to the vortex-antivortex annihilation process shown in Fig. 19. After collision two distinct energy lumps emerge along the positive and negative y-axis but eventually dissipate into spinwaves.

The situation described above is illustrated in Fig. 18 which depicts three characteristic snapshots of the collision of two like vortices that start from an initial relative distance $d = 5$ with velocities $\mathbf{v}_1 = (0.65, 0)$ and $\mathbf{v}_2 = (-0.65, 0)$. We have chosen to illustrate only the field $\mathbf{n}$, through its projection on the (12) plane, and hence the antiferromagnetic discontinuity present in Fig. 17 is not apparent in Fig. 18. However we have actually calculated the spin values on the original lattice and then proceeded with the determination of $\mathbf{n}$ as well as the auxiliary fields. We were thus able to confirm several important details of the formulation presented in Section 2.

The picture changes drastically in the case of a vortex-antivortex pair initially at rest, at a relative distance d on the x-axis. Such a pair is initially described by the product ansatz

$$\Omega = f(\rho_+)e^{i\phi_+} f(\rho_-)e^{-i\phi_-}, \tag{4.7}$$

where notation is the same as in Eq. (4.6). The subsequent evolution was again studied by a numerical calculation similar to the one described earlier for a pair of two like vortices. The vortex and the antivortex now begin to accelerate toward each other apparently because their interaction potential is attractive. Fig. 19 depicts three characteristic snapshots of the field $\mathbf{n}$ which indicate that the resulting spin configuration shows no sign of a nontrivial topological structure, or that the vortex-antivortex pair is annihilated. Nevertheless a closer examination of the time evolution of the energy density shown in Fig. 20 suggests that the annihilation process is not completely dull. Indeed two distinct lumps of energy are emitted along the positive and negative y-axis which do not correspond to any well defined soliton structures and eventually dissipate into spinwaves. It is interesting that a tendency for a 90° scattering persists even in the present case [36].

To summarize, our calculation of head-on collisions of AFM vortices confirms what appears to be a robust feature of relativistic topological solitons [27, 30, 36]. It is more than clear that a simple theoretical explanation of the observed behavior should be possible to obtain almost independently of the specific dynamical model. However such an explanation has thus far been offered only within the context of some variant or other of collective coordinates. For example, vortices in a Higgs model were discussed along those lines in Ref. [37] and shown to exhibit 90° scattering, at least in the so-called Bogomonly limit. At this point, we do not have a convincing theoretical interpretation of our numerical data for head-on collisions. But in the case of AFM vortices in a uniform magnetic field, a theoretical explanation of the dynamics can be given following the theory of Chapter I for FM bubbles. This issue is taken up in the next section.

5. Vortices in a magnetic field

The effect of an applied uniform magnetic field $\mathbf{H}$ is accounted for by including a Zeeman term in the Hamiltonian (2.1),

$$W \to W - g_0 \mu_0 \sum_{ij} (\mathbf{H} \cdot \mathbf{S}_{i,j}), \tag{5.1}$$

where $g_0 \sim 2$ is the gyromagnetic ratio and $\mu_0 = e/2mc$ is the Bohr magneton divided by the Planck constant. AFM vortices then acquire the general dynamical features of FM bubbles described in the beginning of Section 4. Such a radical change of behavior was already speculated in Ref. [38] and is established here by means of unambiguous conservation laws that link the dynamics with the underlying topology. The derived qualitative picture is then confirmed by direct numerical simulations.

The classical ground state is now obtained by assigning a spin value $\mathbf{A}$ on the first sublattice (solid circles) and a value $\mathbf{B}$ on the second (open circles). We further introduce the unit vectors $\mathbf{a} = \mathbf{A}/s$ and $\mathbf{b} = \mathbf{B}/s$ to write for the energy of such a configuration

$$W/s^2 J\Lambda = 2(\mathbf{a} \cdot \mathbf{b}) + \frac{1}{4}\varepsilon^2(a_3^2 + b_3^2) - \frac{g_0\mu_0}{2sJ}\mathbf{H} \cdot (\mathbf{a} + \mathbf{b}), \tag{5.2}$$

where ε is the dimensionless anisotropy constant of Eq. (2.5) and Λ is the total number of lattice sites assumed to be large. For a field of strength H applied along the third direction the minimum of (5.2) is achieved by the canted spin configuration of Fig. 21, defined up to an arbitrary azimuthal rotation, where the canting angle is given by

$$\sin\delta = \frac{H}{H_c}, \qquad H_c = \frac{(8 + \varepsilon^2)sJ}{g_0\mu_0}, \tag{5.3}$$

for field values in the range $H < H_c$. Above the critical field H_c a transition takes place into a ferromagnetic phase ($\delta = \frac{\pi}{2}$). Actually we shall mostly study the parameter regime where both the anisotropy and the applied field are weak, namely

$$\varepsilon \ll 1, \qquad H \ll H_c \approx \frac{8sJ}{g_0\mu_0}, \tag{5.4}$$

which are conditions for the validity of a continuum approximation and are sufficiently nonstringent for practical applications. For future reference, Fig. 21 also displays the two vectors

$$\mathbf{m} = \frac{1}{2}(\mathbf{a} + \mathbf{b}), \qquad \mathbf{n} = \frac{1}{2}(\mathbf{a} - \mathbf{b}), \tag{5.5}$$

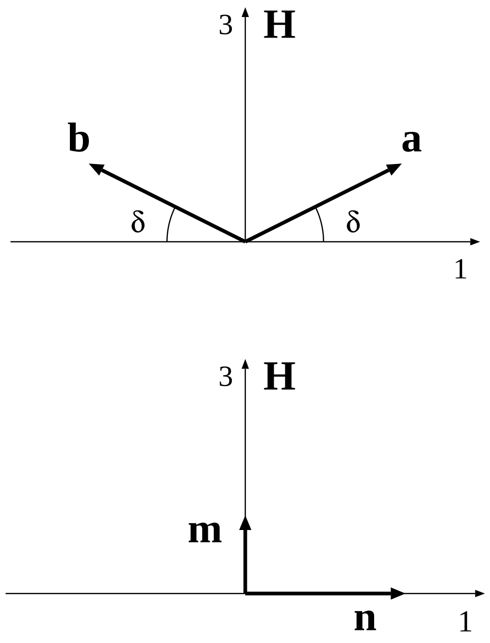

Fig. 21: Schematic illustration of the ground state in the presence of an external uniform magnetic field along the symmetry (third) axis. The canting angle δ is given by Eq. (5.3).

which may be expressed in terms of the canting angle as

$$\begin{aligned} \mathbf{m} &= (0,0,\sin\delta) \approx (g_0\mu_0 H/8sJ)(0,0,1), \\ \mathbf{n} &= (\cos\delta,0,0) \approx (1,0,0), \end{aligned} \tag{5.6}$$

where the second steps have been restricted to the parameter regime (5.4). Therefore a nonvanishing magnetization $\mathbf{m}$ develops along the third direction whereas $\mathbf{n}$ is confined in the basal plane.

When the field is turned on, the Néel state is set in a precessional mode that eventually relaxes into the canted state of Fig. 21 thanks to some dissipative process or other that is always present in a realistic antiferromagnet. Throughout this section we shall assume that the field has been turned on sufficiently long to ensure that equilibrium has been achieved in the ground state. The argument is carried out in five steps described in the following five subsections.

A. The continuum model

We now return to the discrete equations (2.6)-(2.7) which we extend according to

$$\mathbf{F}_{\alpha,\beta} \rightarrow \mathbf{F}_{\alpha,\beta} + g_0\mu_0\mathbf{H}, \qquad \mathbf{G}_{\alpha,\beta} \rightarrow \mathbf{G}_{\alpha,\beta} + g_0\mu_0\mathbf{H}. \tag{5.7}$$

It is also convenient to introduce the rationalized field [29]

$$\mathbf{h} = h\mathbf{e}, \qquad h = \frac{g_0 \mu_0 H}{2\sqrt{2}\varepsilon s J}. \tag{5.8}$$

Eqs. (2.16) are then extended simply by adding a term $\delta(\mathbf{m} \times \mathbf{h})$ to the right-hand side of the first equation and $\delta(\mathbf{n} \times \mathbf{h})$ to the second, where $\delta = \sqrt{2}\varepsilon$. The remaining algebraic details will be omitted here because they are similar to those of Section 2.

Hence the continuum limit is now governed by the strong inequalities

$$\varepsilon, \varepsilon h \ll 1, \tag{5.9}$$

the fields $\mathbf{m}$ and $\mathbf{n}$ continue to satisfy the constraints

$$\mathbf{m} \cdot \mathbf{n} = 0, \qquad \mathbf{n}^2 = 1, \tag{5.10}$$

the auxiliary field $\mathbf{m}$ is given by

$$\mathbf{m} = \frac{\varepsilon}{2\sqrt{2}}[-(\mathbf{n}_\eta + \mathbf{n}_\xi) + (\mathbf{n} \times \dot{\mathbf{n}}) - \mathbf{n} \times (\mathbf{n} \times \mathbf{h})] \tag{5.11}$$

and the field $\mathbf{n}$ satisfies the differential equation

$$\mathbf{n} \times \mathbf{f} = 0, \qquad \mathbf{f} = \ddot{\mathbf{n}} - \Delta\mathbf{n} + 2(\mathbf{h} \times \dot{\mathbf{n}}) + (\mathbf{n} \cdot \mathbf{h})\mathbf{h} + n_3\mathbf{e}. \tag{5.12}$$

As a check of consistency one may explicitly verify that the ground state values (5.6) are compatible with the above equations for parameters that satisfy the strong inequalities (5.9). Finally we note that Eq. (5.12) emerges also in connection with the tetramerization scheme of Fig. 15, while the associated auxiliary fields are

$$\begin{gathered} \mathbf{m} = \frac{\varepsilon}{2\sqrt{2}}[(\mathbf{n} \times \dot{\mathbf{n}}) - \mathbf{n} \times (\mathbf{n} \times \mathbf{h})], \\ \mathbf{k} = -\frac{\varepsilon}{2}\mathbf{n}_x, \qquad \mathbf{l} = -\frac{\varepsilon}{2}\mathbf{n}_y, \end{gathered} \tag{5.13}$$

which should be compared to Eqs. (2.28).

We may thus concentrate on the dynamics of the extended nonlinear σ model (5.12) where the effect of the applied field is twofold; it breaks Lorentz invariance and renormalizes the single ion anisotropy. An efficient study of the dynamics is carried out through a variational principle, namely

$$\mathbf{f} = -\frac{\delta\mathcal{A}}{\delta\mathbf{n}}, \tag{5.14}$$

where $\mathcal{A}$ is the action

$$\mathcal{A} = \int L\, dx dy d\tau, \tag{5.15}$$

and L is the corresponding Lagrangian density [9]

$$L = \frac{1}{2}[\dot{\mathbf{n}}^2 - (\partial_\mu \mathbf{n} \cdot \partial_\mu \mathbf{n})] + \mathbf{h} \cdot (\mathbf{n} \times \dot{\mathbf{n}}) - \frac{1}{2}[(\mathbf{n} \cdot \mathbf{h})^2 + n_3^2]. \tag{5.16}$$

We further resolve the constraint $\mathbf{n}^2 = 1$ explicitly using, for example, the spherical parametrization (3.3) to write

$$\begin{aligned} L =& \frac{1}{2}[\dot{\Theta}^2 + \sin^2\Theta\, \dot{\Phi}^2] - \frac{1}{2}[(\partial_\mu \Theta \partial_\mu \Theta) + \sin^2\Theta\, (\partial_\mu \Phi \partial_\mu \Phi)] \\ &+ h \sin^2\Theta\, \dot{\Phi} - \frac{1}{2}(1 + h^2) \cos^2\Theta. \end{aligned} \tag{5.17}$$

Hence there exist two pairs of canonical fields given by

$$\begin{aligned} \psi_1 &= \Theta, \qquad \pi_1 = \dot{\Theta} \\ \psi_2 &= \Phi, \qquad \pi_2 = \sin^2\Theta\, (\dot{\Phi} + h). \end{aligned} \tag{5.18}$$

The Hamiltonian is then obtained from

$$W = \int w\, dx dy, \qquad w = \pi_a \dot{\psi}_a - L, \tag{5.19}$$

where the repeated Latin index a is summed over the two distinct values of Eq.(5.18). A more explicit form of the energy density w expressed directly in terms of the field $\mathbf{n}$ reads

$$w = \frac{1}{2}[\dot{\mathbf{n}}^2 + (\partial_\mu \mathbf{n} \cdot \partial_\mu \mathbf{n})] + \frac{1}{2}(1 + h^2) n_3^2, \tag{5.20}$$

where we find no trace of the nonrelativistic term $\mathbf{h} \cdot (\mathbf{n} \times \dot{\mathbf{n}})$ of Eq. (5.16). The energy W is now measured in units of $2\sqrt{2}\varepsilon s^2 J$.

Therefore the extended nonlinear σ model (5.12) may be cast in the standard Hamiltonian form

$$\dot{\psi}_a = \frac{\delta W}{\delta \pi_a}, \qquad \dot{\pi}_a = -\frac{\delta W}{\delta \psi_a}; \qquad a = 1, 2, \tag{5.21}$$

which will be the basis for our subsequent theoretical discussion. For instance, the conserved linear momentum should be given by

$$p_\mu = -\int \pi_a \partial_\mu \psi_a\, dx dy, \tag{5.22}$$

and the angular momentum by

$$\ell = -\int \pi_a \varepsilon_{\mu\nu} x_\mu \partial_\nu \psi_a \, dxdy. \tag{5.23}$$

Using the canonical variables of Eq. (5.18) a more explicit form of linear momentum reads

$$p_\mu = -\int (\dot{\Theta}\partial_\mu\Theta + \sin^2\Theta\,\dot{\Phi}\partial_\mu\Phi + h\sin^2\Theta\,\partial_\mu\Phi) dxdy \tag{5.24}$$

and is in agreement with the expression quoted in Ref. [38]. However the field dependent term in Eq. (5.24) leads to an improper integral for vortex configurations for which $\Theta \sim \frac{\pi}{2}$ and $\Phi \sim \kappa\phi$ at spatial infinity. One would think that this difficulty may be resolved by modifying the momentum density by a total divergence, thus replacing $\sin^2\Theta\,\partial_\mu\Phi$ by $(\sin^2\Theta - 1)\partial_\mu\Phi = -\cos^2\Theta\,\partial_\mu\Phi$, which would indeed lead to proper behavior at infinity where $\cos\Theta = 0$. Nevertheless the ambiguity would then be shifted to the origin of the vortex where $\partial_\mu\Phi$ is singular, because Φ is multivalued, while $\Theta = 0$ or π and $\cos\Theta = \pm 1 \neq 0$.

The ambiguities in the linear momentum signal an important link between the dynamics and the underlying topological complexity, in analogy with the situation previously analyzed for FM bubbles. In turn, the relativistic dynamics of AFM vortices studied in earlier sections should be radically altered by the applied field. A complete resolution of the ambiguities is given in subsection C after the ground is prepared in subsection B.

B. Vorticity and the stress tensor

For any 2D field theory that can be brought to the standard Hamiltonian form (5.22) one may define a (scalar) vorticity

$$\gamma = \varepsilon_{\mu\nu}\partial_\mu \pi_a \partial_\nu \psi_a, \tag{5.25}$$

where $\varepsilon_{\mu\nu}$ is the 2D antisymmetric tensor ($\varepsilon_{11} = 0 = \varepsilon_{22}$, $\varepsilon_{12} = 1 = -\varepsilon_{21}$). Terminology is borrowed from fluid dynamics because the quantity γ shares with ordinary vorticity several formal properties. The time derivative of γ is calculated from the Hamilton equations to yield

$$\dot{\gamma} = -\varepsilon_{\mu\nu}\partial_\mu \tau_\nu \tag{5.26}$$

where the vector density

$$\tau_\nu = \frac{\delta W}{\delta \psi_a}\partial_\nu \psi_a + \frac{\delta W}{\delta \pi_a}\partial_\nu \pi_a \tag{5.27}$$

is analogous to the "force density" employed by Thiele [4] in the problem of FM bubbles. It is not difficult to see that τ_ν may be written as a total divergence,

$$\tau_\nu = \partial_\lambda \sigma_{\nu\lambda}, \tag{5.28}$$

where the tensor $\sigma_{\nu\lambda}$ is the stress tensor

$$\sigma_{\nu\lambda} = w\delta_{\nu\lambda} - \frac{\partial w}{\partial(\partial_\lambda \psi_a)}\partial_\nu \psi_a - \frac{\partial w}{\partial(\partial_\lambda \pi_a)}\partial_\nu \pi_a \tag{5.29}$$

calculated for a specific energy density w. Eq. (5.26) then reads

$$\dot{\gamma} = -\varepsilon_{\mu\nu}\partial_\mu \partial_\lambda \sigma_{\nu\lambda} \tag{5.30}$$

and proves to be fundamental for our purposes [5,12].

It should be noted that the preceding discussion makes no distinction between ordinary field theories and those endowed with nontrivial topological structure or related properties. However a clear distinction emerges when we consider the total vorticity

$$\Gamma = \int \gamma \, dxdy = \varepsilon_{\mu\nu} \int \partial_\mu \pi_a \partial_\nu \psi_a \, dxdy, \tag{5.31}$$

which is conserved by virtue of Eq. (5.30) for any field configuration with reasonable behavior at infinity. One may also write

$$\Gamma = \varepsilon_{\mu\nu} \int [\partial_\mu(\pi_a \partial_\nu \psi_a) - \pi_a \partial_\mu \partial_\nu \psi_a] dxdy \tag{5.32}$$

to indicate that a vanishing value of the total vorticity is the rule rather than the exception. Indeed, under normal circumstances, the first term in (5.32) is shown to vanish by transforming it into a surface integral at infinity and the second term also vanishes because $\varepsilon_{\mu\nu}\partial_\mu\partial_\nu\psi_a = 0$ for any differentiable function ψ_a. Yet the above conditions may not be met in a field theory with nontrivial topology, a fact closely related to the ambiguities discussed in connection with the linear momentum. In general, the canonical definition of conservation laws is rendered ambiguous when the total vorticity Γ is different from zero.

It is then important to examine more closely the definition of vorticity in the current model. Substitution of the canonically conjugate fields of Eq. (5.18) in Eq. (5.25) and straightforward algebraic manipulation yield the local vorticity

$$\gamma = \varepsilon_{\mu\nu}\partial_\mu(\dot{\mathbf{n}} \cdot \partial_\nu \mathbf{n}) + h\omega, \tag{5.33}$$

where

$$\omega = -\frac{1}{2}[\varepsilon_{\mu\nu} \sin(2\Theta)\, \partial_\nu(2\Theta)\partial_\mu \Phi]. \tag{5.34}$$

The first term in Eq. (5.33) is an uncomplicated total divergence which leads to a vanishing contribution in the total vorticity Γ of Eq. (5.31). Thus we may write

$$\Gamma = h \int \omega \, dx dy \tag{5.35}$$

and further note that the density ω of Eq. (5.34) resembles the Pontryagin density q of Eq. (3.18) except for an overall factor $-\frac{1}{2}$ and the replacement $\Theta \to 2\Theta$. The latter suggests considering the three-component vector $\mathbf{N} = (N_1, N_2, N_3)$ with

$$\begin{aligned} N_1 &= 2n_3 n_1 = \sin(2\Theta)\cos\Phi, \\ N_2 &= 2n_3 n_2 = \sin(2\Theta)\sin\Phi, \\ N_3 &= 2{n_3}^2 - 1 = \cos(2\Theta), \end{aligned} \tag{5.36}$$

which is also a unit vector field ($\mathbf{N}^2 = 1$). The density ω may then be written as

$$\omega = -\frac{1}{4}\varepsilon_{\mu\nu}(\partial_\nu \mathbf{N} \times \partial_\mu \mathbf{N}) \cdot \mathbf{N} \tag{5.37}$$

and should be compared to the standard Pontryagin density of Eq. (3.17). Furthermore the field $\mathbf{N}$ satisfies the simple boundary condition

$$\mathbf{N} \underset{|\mathbf{x}| \to \infty}{\longrightarrow} (0, 0, -1), \tag{5.38}$$

thanks to the condition $n_3 \to 0$ satisfied by all relevant field configurations, including the vortex configurations of Section 3. The net conclusion is that ω is actually the Pontryagin density for the field $\mathbf{N}$ and thus yields an integer-valued total vorticity

$$\Gamma = 2\pi h \kappa, \qquad \kappa = 0, \pm 1, \pm 2, \ldots, \tag{5.39}$$

where the integer κ will be referred to as the vortex number. Indeed an explicit calculation for a single vortex or antivortex ($\kappa = \pm 1$) discussed in Section 3 confirms Eq. (5.39) for any choice of the polarity ν, in contrast to Eq. (3.20) that depends on both the vortex number and the polarity.

To complete this level of description of the current model we quote an explicit expression for the stress tensor calculated from Eq. (5.29) using as input the energy density (5.20). The final result is

$$\sigma_{\nu\lambda} = w\delta_{\nu\lambda} - (\partial_\nu \mathbf{n} \cdot \partial_\lambda \mathbf{n}), \tag{5.40}$$

where the energy density w may be expressed directly in terms of the field $\mathbf{n}$ through Eq. (5.20).

Finally we give the 3D generalization of the discussion of this subsection. For instance, Eq. (5.30) becomes

$$\dot{\gamma}_i = -\varepsilon_{ijk} \partial_j \partial_l \sigma_{kl}, \tag{5.41}$$

where Latin indices $i, j, \ldots$ assume three distinct values and ε_{ijk} is the 3D antisymmetric tensor. The stress tensor in Eq. (5.41) is obtained by an obvious 3D extension of Eq. (5.40) and the vorticity $\boldsymbol{\gamma} = (\gamma_1, \gamma_2, \gamma_3)$ is given by

$$\gamma_i = \varepsilon_{ijk} \partial_j \pi_a \partial_k \psi_a = \varepsilon_{ijk} \partial_j (\dot{\mathbf{n}} \cdot \partial_k \mathbf{n}) + h\omega_i, \tag{5.42}$$

where the vector density $\boldsymbol{\omega} = (\omega_1, \omega_2, \omega_3)$ reads

$$\omega_i = -\frac{1}{4} \varepsilon_{ijk} (\partial_k \mathbf{N} \times \partial_j \mathbf{N}) \cdot \mathbf{N} \tag{5.43}$$

and generalizes the scalar Pontryagin density (5.37).

C. Conservation laws

We now return to the 2D theory and consider the derivation of unambiguous conservation laws. Since the main strategy was already explained in the related context of FM bubbles our description here will address only the essential points adapted to the present model. The appearance of a double derivative in the right-hand side of the fundamental relation (5.30) suggests that some of the low moments of the local vorticity γ must be conserved. Indeed the linear momentum $\mathbf{p} = (p_1, p_2)$ is given by

$$p_\mu = -\varepsilon_{\mu\nu} I_\nu, \qquad I_\nu = \int x_\nu \gamma \, dxdy, \tag{5.44}$$

and the angular momentum ℓ by

$$\ell = \frac{1}{2} \int \rho^2 \gamma \, dxdy, \tag{5.45}$$

where $\rho^2 = x^2 + y^2$. The list of conservation laws is completed by the total magnetization μ in the third direction,

$$\mu = \int [\mathbf{e} \cdot (\mathbf{n} \times \dot{\mathbf{n}}) - h n_3^2] dxdy, \tag{5.46}$$

which can be derived directly from the equation of motion.

The preceding identifications are made plausible by inserting the general expression for the vorticity given by Eq. (5.25) in Eqs. (5.44) and (5.45) and by freely performing partial integrations to recover the canonical forms of linear and angular momentum quoted in Eqs. (5.22) and (5.23) which are plagued by the ambiguities discussed in connection with Eq. (5.24). However no such ambiguities occur in Eqs. (5.44) and (5.45) because the local vorticity γ can be obtained directly from the field $\mathbf{n}$, rather than the angular variables, and is a particularly well defined quantity; see Eqs. (5.35) and (5.37). In other words, partial integrations should be performed with great care and are often unjustified.

The main point of this theoretical exercise is that the very structure of the conservation laws (5.44)-(5.46) suggests a radical change in the dynamical behavior of vortices in an applied field ($h \neq 0$). The effect of a nonvanishing total vorticity ($\Gamma = 2\pi h\kappa$) becomes apparent by considering the transformation of the moments I_ν of Eq. (5.44) under a translation of coordinates $\mathbf{x} \to \mathbf{x} + \mathbf{c}$ where $\mathbf{c} = (c_1, c_2)$ is a constant vector,

$$I_\nu \to I_\nu + \Gamma c_\nu, \tag{5.47}$$

which implies a nontrivial transformation of the linear momentum (5.44) when $\Gamma \neq 0$. This is surely an unusual property, because linear momentum should be expected to remain unchanged under a constant translation of the origin of coordinates, and indicates that the moments I_ν provide a measure of position rather than momentum. Such a fact is made explicit by considering the guiding center vector $\mathbf{R} = (R_1, R_2)$ with coordinates

$$R_\nu = \frac{I_\nu}{\Gamma} = \frac{1}{\Gamma}\int x_\nu \gamma \, dx dy, \tag{5.48}$$

which transforms as $\mathbf{R} \to \mathbf{R} + \mathbf{c}$ under a constant translation and is thus a measure of position of a spin configuration with $\Gamma \neq 0$. Nevertheless the vector $\mathbf{R}$ is conserved.

A related fact is that the familiar Poisson bracket algebra is significantly affected when $\Gamma \neq 0$. Using the canonical Poisson brackets,

$$\{\pi_a(\mathbf{x}),\, \psi_b(\mathbf{x}')\} = \delta_{ab}\delta(\mathbf{x} - \mathbf{x}'), \tag{5.49}$$

and the general expression of the local vorticity (5.25) in the definition of the linear momentum (5.44), it is not difficult to establish the relations

$$\{p_1, p_2\} = \Gamma, \qquad \{R_1, R_2\} = 1/\Gamma, \tag{5.50}$$

which are strongly reminiscent of the situation in the case of electron motion in a uniform magnetic field, the role of the latter being played here by the total vorticity Γ.

Similarly the angular momentum (5.45) actually provides a measure of the vortex size, a fact made explicit by considering the mean squared radius defined from

$$r^2 = \frac{1}{\Gamma}\int (\mathbf{x}-\mathbf{R})^2\gamma\, dxdy = \frac{2\ell}{\Gamma} - \mathbf{R}^2, \tag{5.51}$$

which is also conserved. Needless to say, the conservation laws (5.44) and (5.45) resume their ordinary physical significance at vanishing total vorticity ($\Gamma = 0$).

The observed transmutation in the physical significance of the conservation laws of linear and angular momentum implies a radical change in the dynamical behavior of topological solitons. For example, a single AFM vortex or antivortex ($\kappa = \pm 1$) in a uniform magnetic field carries a nonvanishing total vorticity ($\Gamma = \pm 2\pi h$) and thus cannot be found in a free translational motion ($\dot{\mathbf{R}} = 0$). It is always spontaneously pinned or frozen within the antiferromagnetic medium, in contrast to the freely moving vortices occurring in the relativistic theory at vanishing field. Vortex motion can occur in the presence of other vortices, but the dynamical pattern is also expected to be substantially different from the one obtained at vanishing field in Section 4. Specifically, interacting AFM vortices should now behave as ordinary vortices in a fluid or as electric charges in a uniform magnetic field, as demonstrated by direct simulations in subsection D.

The preceding discussion was kept deliberately general in order to emphasize that the emerging qualitative picture is valid in any field theory for which the total vorticity Γ may be different from zero. However it is now useful to express the conservation laws in a more explicit form that takes into account the specific structure of the current model. We thus insert the local vorticity of Eq. (5.33) in Eq. (5.44) to obtain the linear momentum

$$p_\mu = -\int [(\dot{\mathbf{n}}\cdot\partial_\mu \mathbf{n}) + h\varepsilon_{\mu\nu}x_\nu\omega]dxdy, \tag{5.52}$$

where we have performed a partial integration in the first term which is free of all ambiguities. Similarly the angular momentum (5.45) reads

$$\ell = \int [-\varepsilon_{\mu\nu}x_\mu(\dot{\mathbf{n}}\cdot\partial_\nu \mathbf{n}) + \frac{1}{2}h\rho^2\omega]dxdy. \tag{5.53}$$

As mentioned already, the above conservation laws possess their usual physical significance only at vanishing total vorticity, $\Gamma = 2\pi h\kappa = 0$, which may be achieved when either the applied field h or the vortex number κ vanishes. Otherwise one must consider the guiding center coordinates (5.48) or

$$R_\mu = \frac{1}{2\pi h\kappa}\int[-\varepsilon_{\mu\nu}(\dot{\mathbf{n}}\cdot\partial_\nu\mathbf{n}) + hx_\mu\omega]dxdy \tag{5.54}$$

and the radius r calculated from Eq. (5.51). It should be noted that the preceding conservation laws display some formal similarities to those derived in a model for a superconductor [6,7].

Finally we return briefly to the 3D theory discussed in the concluding paragraph of subsection B and quote the corresponding conservation laws of linear and angular momentum

$$\mathbf{p} = -\frac{1}{2}\int(\mathbf{r}\times\boldsymbol{\gamma})dV, \qquad \mathbf{l} = -\frac{1}{3}\int[\mathbf{r}\times(\mathbf{r}\times\boldsymbol{\gamma})]dV, \tag{5.55}$$

where $\mathbf{r} = (x,y,z)$, $dV = dxdydz$ and $\boldsymbol{\gamma} = (\gamma_1,\gamma_2,\gamma_3)$ is the vector vorticity field of Eq. (5.42). It is interesting that (5.55) are formally identical to the conservation laws derived in fluid dynamics, at least for incompressible fluids; see Eqs. (7.2.5) and (7.2.6) of Ref. [14].

D. Interacting vortices

In the presence of a bias field the static vortices of Section 3 adjust to a slightly different shape. It is not difficult to see that the functional form of a static vortex remains the same as in Eq. (3.13) except that $\theta = \theta(\rho)$ now satisfies the ordinary differential equation

$$\frac{1}{\rho}\frac{\partial}{\partial\rho}\left(\rho\frac{\partial\theta}{\partial\rho}\right) + \left(1 + h^2 - \frac{1}{\rho^2}\right)\cos\theta\sin\theta = 0, \tag{5.56}$$

which differs from Eq. (3.10) only by an additional easy-plane anisotropy with strength equal to h^2. Consequently Eq. (5.56) reduces to Eq. (3.10) by the simple rescaling $\overline{\rho} = \sqrt{1+h^2}\rho$ and the vortex profile $\theta = \theta(\overline{\rho})$ is again given by Fig. 16 with the replacement $\rho \to \overline{\rho}$. More importantly, the auxiliary fields (5.11) or (5.13) now contain field dependent terms that are crucial for a correct calculation of the actual spin values on the lattice of Fig. 14 or Fig. 15, respectively.

A pair of like vortices initially at rest is described by the product ansatz (4.2) taking into account the field dependent modifications discussed in the preceding paragraph. The ensuing time evolution of the vortex pair was obtained numerically. Instead of drifting away the two vortices actually begin to rotate around each other,

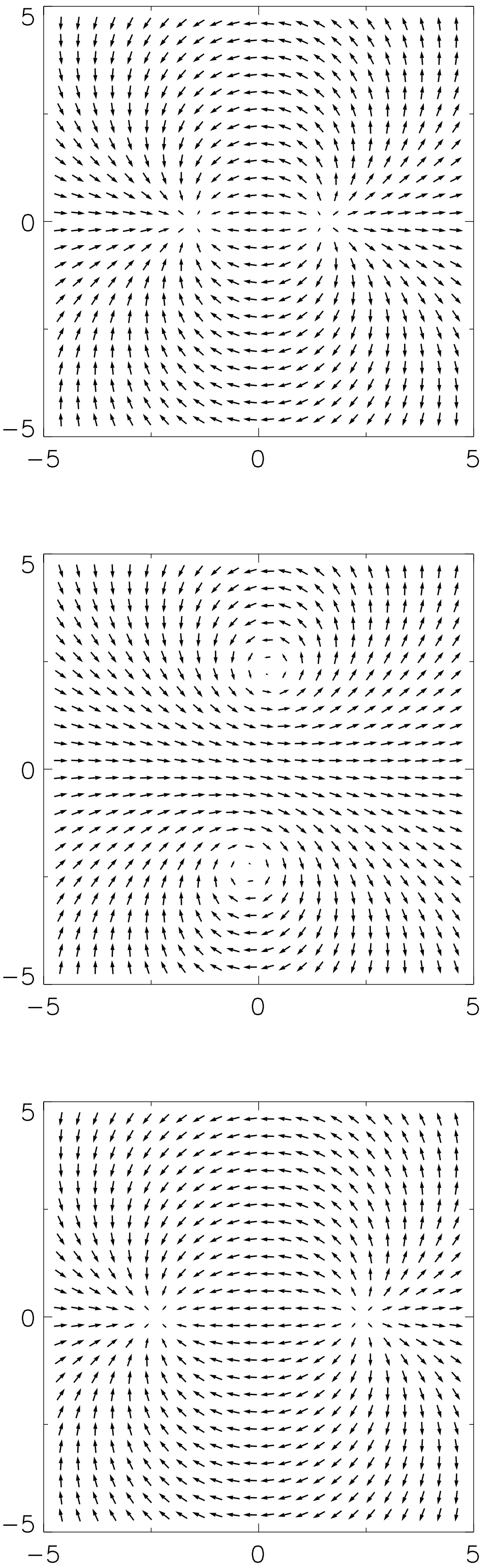

Fig. 22: Time evolution of a pair of like vortices in the presence of a bias field $h=1$. The two vortices are initially at rest, at a relative distance $d=3$ on the x-axis, and subsequently orbit around each other instead of drifting away. Together with the initial configuration of the field $\mathbf{n}$ projected on the (12) plane (upper entry) we provide snapshots at instances when the pair had rotated by 90° (middle entry) and 180° (lower entry). A 90° rotation in real space is always followed by a 90° internal phase shift.

in sharp contrast to the situation described in Section 4 at vanishing field. In other words, each vortex moves in a direction perpendicular to the applied force, in analogy with the skew deflection of FM bubbles in a field gradient analyzed in Chapters I and II. Fig. 22 illustrates the initial configuration together with two characteristic snapshots taken at time intervals such that the pair had rotated roughly by 90° and 180°, respectively. It is interesting to note that a 90° rotation of the pair in real space is always followed by a 90° internal phase shift of each vortex. Fig. 23 depicts the actual trajectories obtained by tracking the points where $|n_3| = 1$. Inspite of an apparent initial tendency to drift away, the two vortices eventually orbit around each other, in complete analogy with the 2D motion of two like vortices in an ordinary fluid or two interacting electrons in a uniform magnetic field. The observed departures of the trajectories of Fig. 23 from a circular shape correspond to the well-known Larmor oscillations in the electron problem. These oscillations are expected to be smoothed out in the limit of large relative distance.

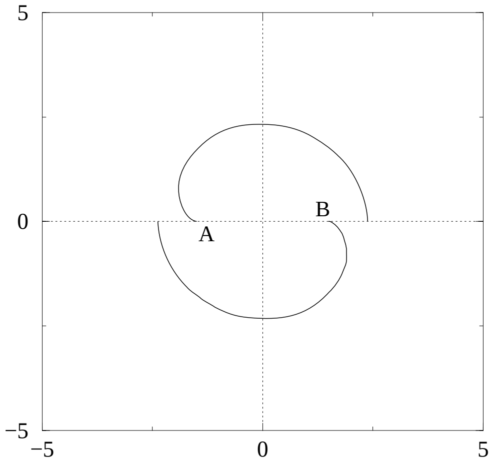

Fig. 23: Trajectories of the two rotating vortices of Fig. 22 obtained by tracking the points where $|n_3|=1$. The two vortices originated at points A and B on the x-axis and the process was interrupted after the pair had completed a 180° rotation.

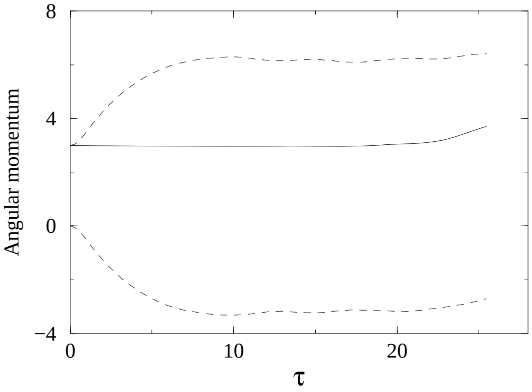

Fig. 24: Evolution of the angular momentum of the vortex pair of Figs. 22 and 23 calculated from Eq. (5.53). The total angular momentum ℓ (solid line) is fairly well conserved, except at late times when numerical instabilities develop on the finite lattice. The lower (upper) dashed line depicts the nontrivial time dependence of the first (second) term in Eq. (5.53).

The above results are consistent with the qualitative picture suggested by the conservation laws of subsection C. The two-vortex system carries a total vortex number $\kappa = 2$ and thus a nonvanishing total vorticity $\Gamma = 4\pi h$. The guiding center calculated from Eq. (5.54) is initially located at the origin of the coordinate system and remains fixed at all later times. The angular momentum was calculated numerically based on Eq. (5.53) and its time evolution is demonstrated in Fig. 24. Although the two pieces of Eq. (5.53) acquire a nontrivial time dependence, their sum is fairly well conserved. Furthermore the same general picture was obtained by repeating the calculation for a pair of vortices with the same vortex numbers ($\kappa_1 = \kappa_2$) but opposite polarities ($\nu_1 = -\nu_2$). This result is consistent with the fact that the driving issue is the total vorticity $\Gamma = 2\pi h(\kappa_1 + \kappa_2)$ which is independent of the polarities, in contrast to the ordinary winding number Q of Eq. (3.20).

The calculation was further repeated for a vortex-antivortex pair initially described by the product ansatz (4.7) incorporating the appropriate field dependent modifications. Recall that at vanishing field the vortex and the antivortex are attracted toward each other and are eventually annihilated. The situation is drastically different at nonvanishing field. The pair undergoes Kelvin motion roughly along parallel lines that are perpendicular to the line connecting the vortex and the antivortex.

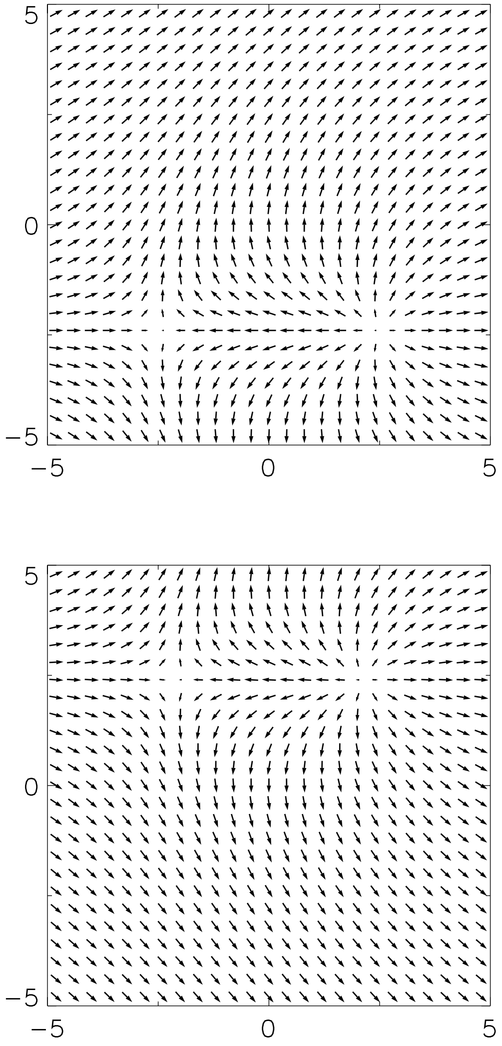

Fig. 25: Evolution of a vortex-antivortex pair in the presence of a bias field h=1. The vortex and the antivortex are initially at rest at the points (2.4, -2.4) and (-2.4, -2.4) of the xy-plane (upper entry). Instead of converging toward each other and annihilating, the pair moves in formation along the y-axis (Kelvin motion) as demonstrated by the snapshot of the lower entry taken at a later instance $(\tau \approx 20)$.

Fig. 25 depicts the initial configuration together with a snapshot taken at a later instance when the pair had moved in formation along the y-axis to a distance approximately equal to the initial relative separation. Fig. 26 demonstrates the actual trajectories (solid lines) obtained by tracking the points where $|n_3| = 1$. Therefore the derived picture is qualitatively identical to the Kelvin motion of a vortex-antivortex pair in an ordinary fluid or the Hall motion of an interacting electron-positron pair in a uniform magnetic field.

Returning to the conservation laws we note that the total vorticity of a vortex-antivortex pair vanishes ($\kappa = \kappa_1 + \kappa_2 = 0$ and hence $\Gamma = 0$). Therefore it is now meaningful to interpret (5.52) as the conserved total linear momentum of the system. A nonvanishing component develops only along the y-axis, i.e., along the direction of motion of the pair, and its conservation is demonstrated in Fig. 27. Again each of the two pieces in Eq. (5.52) exhibits a nontrivial time dependence but their sum is fairly well conserved. On the other hand, it is still meaningful to define individual guiding centers when the pair is widely separated. For example, approximate guiding centers for the vortex and the antivortex may be defined by restricting the integration in Eq. (5.54) to the right and left half plane and setting $\kappa = 1$ and $\kappa = -1$, respectively. The trajectories obtained by tracking the above approximate guiding centers are also shown in Fig. 26 (dashed lines) and are close to two parallel straight lines. The analogy with the motion of an electron-positron pair in a uniform magnetic field in now made more definite. The actual trajectories of the

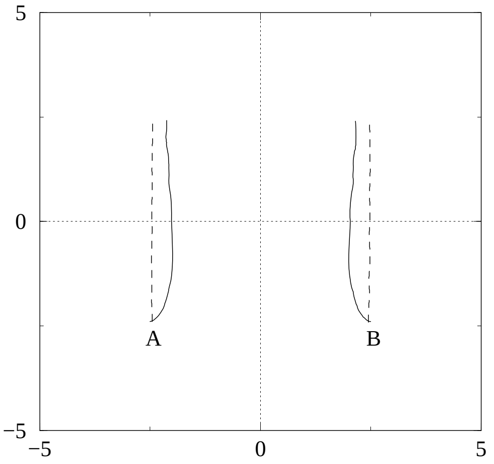

Fig. 26: Trajectories of the vortex and the antivortex of Fig. 25 originating at the points B=(2.4, -2.4) and A=(-2.4, -2.4). The actual trajectories (solid lines) were obtained by tracking the points where $|n_3|$=1. The trajectories of the guiding centers (dashed lines) were calculated from Eq. (5.55) restricted to the corresponding half planes and are remarkably close to two parallel straight lines.

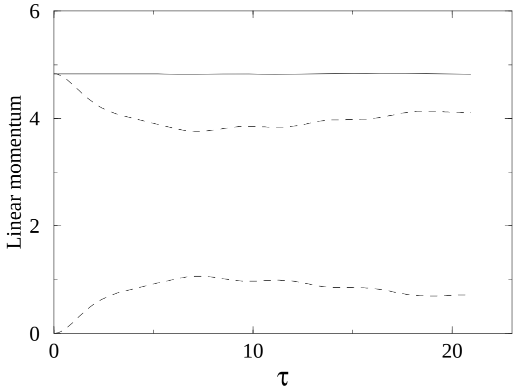

Fig. 27: Evolution of the linear momentum of the vortex-antivortex pair of Figs. 25 and 26 calculated from Eq. (5.52). (We display only the y-component because the x-component vanishes.) The total linear momentum (solid line) is fairly well conserved, whereas the lower (upper) dashed line depicts the nontrivial time dependence of the first (second) term of Eq. (5.52).

electron and positron undergo Larmor oscillations along the parallel trajectories of their guiding centers, which become increasingly narrower with increasing relative separation. The absence of more than one such oscillation in Fig. 26 is due to our (numerical) inability to follow the motion to a larger distance; see, however, a related calculation of interacting vortices in a charged fluid [7]. Finally we have verified that a vortex-antivortex pair ($\kappa_1 + \kappa_2 = 0$) exhibits Kelvin motion for any choice of relative polarities ($\nu_1 = \nu_2$ or $\nu_1 = -\nu_2$), a fact that reenforces the prominence of the total vorticity Γ in the study of dynamics.

To summarize, a simple comparison of the results of this subsection to those of Section 4 establishes that the dynamics of AFM vortices is profoundly altered by the applied field, in remarkable analogy with the familiar Hall effect. Nevertheless one should keep in mind that the effect of a bias field on AFM vortices would not have been as drastic without the aid of the underlying nontrivial topological structure.

E. The isotropic antiferromagnet

The special case of an isotropic Heisenberg antiferromagnet is important for both practical and theoretical purposes. The isotropic limit was briefly discussed in the concluding paragraphs of Section 3 in the absence of a bias field. It was then mentioned that the model possesses metastable AFM bubbles, instead of vortices, which are characterized by the standard Pontryagin index (3.17). However, when a bias field is turned on, the picture changes drastically for two reasons. First, the applied field itself supplies an effective easy plane anisotropy that leads to vortices instead of bubbles. Second, the dynamics of vortices departs significantly from the relativistic dynamics of the pure antiferromagnet.

In the remainder of this section we shall briefly describe the necessary modifications of the formalism to accommodate the isotropic model in a uniform magnetic field. Since a single ion anisotropy is no longer available to provide the small parameter ε of Eq. (2.5), such a parameter is now furnished by the applied field which is assumed to be weak:

$$\varepsilon = \frac{g_0 \mu_0 H}{2\sqrt{2} sJ} \ll 1. \tag{5.57}$$

The relevant dynamical equations are then obtained from our earlier results by the formal substitution $\mathbf{h} \to \mathbf{e} = (0, 0, 1)$, or $h \to 1$, and by omitting the contribution from the single ion anisotropy. Thus the dynamics of the field $\mathbf{n}$ is now governed by the parameter free Lagrangian

$$L = \frac{1}{2}[\dot{\mathbf{n}}^2 - (\partial_\mu \mathbf{n} \cdot \partial_\mu \mathbf{n})] + \mathbf{e} \cdot (\mathbf{n} \times \dot{\mathbf{n}}) - \frac{1}{2}(\mathbf{e} \cdot \mathbf{n})^2, \tag{5.58}$$

which leads to the equation of motion

$$\mathbf{n} \times \mathbf{f} = 0, \qquad \mathbf{f} = \ddot{\mathbf{n}} - \Delta \mathbf{n} + 2(\mathbf{e} \times \dot{\mathbf{n}}) + (\mathbf{n} \cdot \mathbf{e})\mathbf{e}. \tag{5.59}$$

The associated auxiliary fields are accordingly given by

$$\mathbf{m} = \frac{\varepsilon}{2\sqrt{2}}[-(\mathbf{n}_\eta + \mathbf{n}_\xi) + (\mathbf{n} \times \dot{\mathbf{n}}) - \mathbf{n} \times (\mathbf{n} \times \mathbf{e})], \tag{5.60}$$

for the lattice of Fig. 14, or

$$\begin{gathered} \mathbf{m} = \frac{\varepsilon}{2\sqrt{2}}[(\mathbf{n} \times \dot{\mathbf{n}}) - \mathbf{n} \times (\mathbf{n} \times \mathbf{e})], \\ \mathbf{k} = -\frac{\varepsilon}{2}\mathbf{n}_x, \qquad \mathbf{l} = -\frac{\varepsilon}{2}\mathbf{n}_y, \end{gathered} \tag{5.61}$$

for the lattice of Fig. 15. Finally we must set $h = 1$ throughout our discussion of conservation laws.

Therefore the corresponding physical picture can be readily inferred without further calculation. Static vortices are formally identical to those of Section 3 but their dynamics is similar to the nonrelativistic dynamics of the current Section 5, for any finite value of the applied field. In other words, to the extent that topological solitons are relevant for the physics of an isotropic antiferromagnet, the dynamical picture is changed significantly even by a very weak bias field.

6. Concluding remarks

The emphasis in the main text was placed on elementary processes involving only two AFM vortices, in order to clearly illustrate an important link between topology and dynamics. However further progress in that direction hinges upon the actual production of isolated vortices. Although there exist several examples of realistic antiferromagnets that are effectively two-dimensional, including the parent compounds of high-T_c superconductors, there seems to be no direct experimental evidence for isolated AFM vortices or bubbles. This situation is in marked contrast to the observed abundance of ferromagnetic bubbles, vortices in superfluid helium, or Abrikosov vortices in superconductors, and may change in the future.

The qualitative picture derived from elementary processes must also influence the thermodynamics of 2D antiferromagnets. Work in that direction was already presented in Refs. [39,40] for both Ising-like and single-ion anisotropy, while the effect of an applied field was considered in Ref. [38]. It is clear that much remains to be done in connection with the anticipated Berezinskii-Kosterlitz-Thouless (BKT) phase transition which relies on the dynamics of a gas of interacting vortices and antivortices. Suffice it to say that the dynamics of vortex-antivortex pairs studied in Section 4 is radically modified by an applied magnetic field discussed in Section 5. The BKT theory may have to be reformulated in a way that clearly reflects the fundamental change of behavior in the elementary vortex processes when a field is turned on.

Perhaps the clearest manifestation of the effect of an applied field will emerge in the thermodynamics of an isotropic antiferromagnet. Topological solitons at vanishing field are metastable AFM bubbles that obey relativistic dynamics. However the smallest external field will trigger Hall dynamics for AFM vortices which become the relevant topological excitations. Again a successful BKT theory must reflect this abrupt transition in the limit of vanishing field.

Our discussion is concluded with some comments on a variation of the main theme that has not been treated in this chapter. An easy-axis anisotropy ($g < 0$) would lead to a ground (Néel) state that is polarized along the easy axis. Therefore topological solitons must then satisfy the simple boundary condition (3.16) and would be AFM bubbles classified by the standard Pontryagin index (3.17). However an application of the Derrick theorem either in its original form or its extended version discussed in [31] leads to the conclusion that such solitons do not exist either with finite or infinite energy. This is a notable difference from FM bubbles that occur in easy-axis ferromagnets. The latter have been studied in Chapter I and shown to be stabilized by a combination of the effects of the long-range magnetostatic field created in a ferromagnetic film and of an applied bias field (see also [12]).

Nevertheless, when an easy-axis antiferromagnet is immersed in a uniform magnetic field pointing along the symmetry axis, an effective easy-plane anisotropy is produced that competes with the easy-axis anisotropy. And, when the field exceeds a certain critical value, a spin-flop transition takes place from the Néel state polarized in the third direction to a canted state of the type shown in Fig. 21 which exhibits azimuthal degeneracy. Consequently AFM vortices reappear above the critical value of the applied field and their dynamical properties are very similar to those discussed in Section 5.

Conclusions

The dynamics of magnetic solitons has been studied in this thesis. We have mainly been concerned with a two-dimensional magnetic continuum where the topological excitations are called magnetic bubbles or vortices depending on the structure of the ground state of the magnet. Throughout the text the emphasis was placed on elementary processes involving either one or a pair of solitons. This approach has been fruitful since the dynamical behavior of solitons has been expected and was actually found to be rich as well as unusual at least from the point of view of ordinary particles. This should mainly be attributed to the fact that solitons are extended structures rather than point like particles. The topology of the field describing the solitons has been known to dominate the dynamics and this dominant role has been confirmed here and made clear throughout our study. Nevertheless the role of topology has yet to be examined in the problem of vortex scattering observed in antiferromagnets.

The theoretical study of elementary processes might appear somewhat artificial had there not been the wealth of experiments with isolated bubbles in ferromagnetic films. Thus, because of this background and also in view of the results derived here, we believe that further theoretical as well as experimental study for isolated solitons and their dynamics is well motivated.

We have confined ourselves to the study of the most well known and important classes among magnets namely the ferromagnets and the antiferromagnets. There certainly are a lot of differences between the two due to the different structure of their ground states. The staggered magnetization in the antiferromagnet and the subsequent lack of a net magnetic moment is its most striking difference from the ferromagnet at least from a macroscopic point of view. An important difference in the dynamics is that a bubble or vortex in an antiferromagnet may be found in free translational motion while this is not possible in a ferromagnet.

Nevertheless the two magnets also bear important similarities. Thus the dynamical behavior of ferromagnetic vortices is comparable to that of the antiferromagnetic when the last are in an external magnetic field. It is clear that some experimental work has to be done in this direction to obtain a better understanding and further clarify these remarks, taken into account that little has been done up to now with respect to vortex observation in antiferromagnets.

We also remark here that there certainly are many more interesting questions to be answered with respect to elementary processes in both ferromagnets and antiferromagnets. Thus the detailed long time behavior of a bubble in a ferromagnetic film remains an open question with potential implications in the use of such bubbles in applications. This program seems to rely largely on computer power but theoretical questions have also to be answered.

One further question is suggested by the vortex-antivortex Kelvin motion in antiferromagnets shown in figures III.25 and III.26. Thus we are tempted to think that a vortex-antivortex like pair can be constructed such that it travels coherently with a constant velocity. Such a possibility is in fact realized in an easy-plane ferromagnet [41, 42] and one can certainly look for corresponding soliton solutions in an antiferromagnet based on the results of section III.5.

The methodology employed here is certainly useful not only for ferromagnets and antiferromagnets but can be extended and applied to other classes of magnets such as weak ferromagnets [29]. We expect that some modifications may be needed for the successful application and extraction of relevant results. Nevertheless, any further theoretical progress to this direction will rely upon corresponding experimental results which would render the development of a complete theory useful.

The good understanding of elementary processes achieved so far can be a basis for the study and the understanding of more complex phenomena in magnetic systems involving many bubbles or vortices. Thus we expect that a study of the thermodynamic quantities could in principle provide a proof for the existence of antiferromagnetic vortices. Such an approach could be an alternative to the search for isolated vortices.

Finally we refer to the possibility of genuinely 3D magnetic solitons that is solitons in a 3D model for a magnet without boundaries. The experimentally observed Bloch points are 3D topological defects whose dynamics has not yet been studied within the present framework. Furthermore theoretical arguments for the existence of magnetic vortex rings with a non-vanishing Hopf index [5, 21] have not yet been concluded to a definite calculation that would provide the necessary background for a corresponding experimental search in the bulk of the ferromagnetic medium. Nevertheless some preliminary calculations have been already performed [41] within an easy-plane ferromagnet for a 3D soliton with vanishing Hopf index.

References

[1] A.P. Malozemoff and J.C. Slonczewski, *Magnetic domain walls in bubble materials* (Academic Press, New York, 1979).

[2] T.H. O'Dell, *Ferromagnetodynamics, the dynamics of magnetic bubbles, domains and domain walls* (Wiley, New York, 1981).

[3] A.A. Thiele, Bell Syst. Tech. J. **48** (1969) 3287; J. Appl. Phys. **41** (1970) 1139.

[4] A.A. Thiele, Phys. Rev. Lett. **30** (1973) 230; J. Appl. Phys. **45** (1974) 377.

[5] N. Papanicolaou and T.N. Tomaras, Nucl. Phys. B **360** (1991) 425; N. Papanicolaou, in Singularities in Fluids, Plasmas and Optics, p. 151-158, eds., R.E. Caflisch and G.C. Papanicolaou (Kluwer, Amsterdam, 1993).

[6] N. Papanicolaou and T.N. Tomaras, Phys. Lett. A **179** (1993) 33.

[7] G. Stratopoulos and T.N. Tomaras, Phys. Rev. B **54** (1996) 12493.

[8] L. Landau and E. Lifshitz, Physik A (Soviet Union) **8** (1935) 153.

[9] V.G. Bar'yakhtar, M.V. Chetkin, B.A. Ivanov and S.N. Gadetskii, *Dynamics of topological magnetic solitons-experiment and theory* (Springer-Verlag, Berlin, 1994).

[10] N. Papanicolaou, Physica D 74 (1994) 107; Phys. Lett. A **186** (1994) 119.

[11] N. Papanicolaou and W.J. Zakrzewski, Physica D **80** (1995) 225; Phys. Lett. A **210** (1996) 328.

[12] S. Komineas, N. Papanicolaou, Physica D **99** (1996) 81-107.

[13] G.H. Derrick, J. Math. Phys. **5** (1964) 1252.

[14] G.K. Batchelor, *An Introduction to Fluid Dynamics* (Cambridge University Press, 1967).

[15] H.K. Moffat, J. Fluid Mech. **35** (1969) 117.

[16] H.K. Moffat, *Magnetic Field Generation in Electrically Conducting Fluids* (Cambridge University Press, 1978).

[17] *Topological Aspects of the Dynamics of Fluids and Plasmas*, NATO ASI Series, eds., H.K. Moffat, G.M. Zaslavsky, P. Compte and M. Tabor (Kluwer, Dordrecht, 1992).

[18] E.A. Kuznetsov and A.V. Mikhailov, Phys. Lett. A **77** (1980) 37.

[19] R. Bott and L.W. Tu, *Differential Forms in Algebraic Topology* (Springer, New York, 1982).

[20] X.G. Wen and A. Zee, Phys. Rev. Lett. **61** (1988) 1025.

[21] J.E. Dzyaloshinskii and B.A. Ivanov, JETP Lett. **29** (1979) 540.

[22] J.C. Slonczewski, J. Magn. Magn. Mat. **12** (1979) 108.

[23] F.D.M. Haldane, Phys. Rev. Lett. **57** (1986) 1488.

[24] G.E. Volovik, J. Phys. C: Solid State Phys. **20** (1987) L83.

[25] W.J. DeBonte AIP Conf. Proc. **5** (1971) 140; J. Appl. Phys. **44** (1973) 1793; IEEE Trans. Magn., MAG-**11** (1975) 3.

[26] T.G.W. Blake, E. Della Torre, J. Appl. Phys. **50** (1979) 2192; E. Della Torre, C. Hagedüs, G. Kádár, AIP Conf. Proc. **29** (1975) 89.

[27] R.A. Leese, M. Peyrard and W.J. Zakrzewski, Nonlinearity **3** (1990) 773.

[28] A.A. Belavin and A.M. Polyakov, JETP Lett. **22** (1975) 245.

[29] N. Papanicolaou, Phys. Rev. B **51** (1995) 15062; Phys. Rev. B **55** (1997) 12290.

[30] N.S. Manton, Phys. Lett. B **110** (1982) 54; M. Atiyah and N. Hitchin, *The geometry and dynamics of magnetic monopoles* (Princeton University Press, Princeton, 1988).

[31] S. Komineas, N. Papanicolaou, Nonlinearity **11** (1998) 265-290.

[32] A.F. Andreev and V.I. Marchenko, Sov. Phys. Uspekhi **23** (1980) 21.

[33] B.A. Ivanov and A.K. Kolezhuk, Phys. Rev. Lett. **74** (1995) 1859.

[34] R.J. Donnely, *Quantized vortices in helium II* (Cambridge University Press, Cambridge, 1991).

[35] B.A. Ivanov, A.K. Kolezhuk and G.M. Wysin, Phys. Rev. Lett. **76** (1996) 511.

[36] R.S. Ward, Phys. Lett. B **158** (1985) 424; W.J. Zakrzewski, Nonlinearity **4** (1991) 429; R.A. Leese, Nucl. Phys. B **344** (1990) 33.

[37] P.J. Ruback, Nucl. Phys. B **296** (1988) 669.

[38] B.A. Ivanov and D.D. Sheka, Phys. Rev. Lett. **72** (1994) 404.

[39] A.R. Völkel, G.M. Wysin, A.R. Bishop and F.G. Mertens, Phys. Rev. B **44** (1991) 10066.

[40] A.R. Pereira and A.S.T. Pires, Phys. Rev. B **51** (1995) 996.

[41] N. Papanicolaou and P. N. Spathis "semitopological solitons in planar ferromagnets" to appear in Nonlinearity.

[42] N. R. Cooper Phys. Rev. Lett. **80** (1998) 4554.